# Neural Tangent Kernels Motivate Cross-Covariance Graphs in Neural Networks

Shervin Khalafi [1] Saurabh Sihag [1] Alejandro Ribeiro [1]

## Abstract

Neural tangent kernels (NTKs) provide a theoretical regime to analyze the learning and generalization behavior of over-parametrized neural networks. For a supervised learning task, the association between the eigenvectors of the NTK and given data (a concept referred to as alignment in this paper) can govern the rate of convergence of gradient descent, as well as generalization to unseen data. Building upon this concept and leveraging the structure of NTKs for graph neural networks (GNNs), we theoretically investigate NTKs and alignment, where our analysis reveals that optimizing the alignment translates to optimizing the graph representation or the graph shift operator (GSO) in a GNN. Our results further establish theoretical guarantees on the optimality of the alignment for a two-layer GNN and these guarantees are characterized by the graph shift operator being a function of the cross-covariance between the input and the output data. The theoretical insights drawn from the analysis of NTKs are validated by our experiments focused on a multi-variate time series prediction task for a publicly available dataset. Specifically, they demonstrate that GNN-based learning models that operate on the cross-covariance matrix indeed outperform those that operate on the covariance matrix estimated from only the input data.

## 1. Introduction

The remarkable success of deep learning frameworks for numerous inference tasks is well established (LeCun et al., 2015). Motivated by the practical implications of the gaps between the empirical observations and theoretical foundations of deep learning, many recent works have explored various approaches to rigorously understand the theory of deep learning models. Multi-layer neural networks have been analyzed extensively in the mean-field regime (Mei et al., 2018; 2019; Sirignano & Spiliopoulos, 2020). The random features model has also been studied to capture the effects of the regime of parameterization and study phenomenon such as generalization, and "double descent" (see e.g., (Mei & Montanari, 2022; Lin & Dobriban, 2021; Adlam & Pennington, 2020)). Among such approaches, the NTK, first introduced in (Jacot et al., 2018), has commonly been used to study the behavior of over-parameterized neural networks (Cao et al., 2021); (Bietti & Mairal, 2019); and is informally defined next.

**Neural Tangent Kernel.** For any given predictor $f(\mathbf{x}; \mathbf{w}) : \mathbb{R}^{n\times 1} \times \mathbb{R}^p \to \mathbb{R}$ the NTK is the kernel matrix $\Theta$ defined by the gradient of the predictor output, $f(\mathbf{x}; \mathbf{w})$, with respect to its learnable parameters, $\mathbf{w}$, as

$$\Theta_{(\mathbf{x}_i,\mathbf{x}_j)}(\mathbf{w}) := \langle \nabla_{\mathbf{w}} f(\mathbf{x}_i; \mathbf{w}), \nabla_{\mathbf{w}} f(\mathbf{x}_j; \mathbf{w})\rangle \ , \qquad (1)$$

where $f(\mathbf{x}; \mathbf{w})$ represents the predictor output for input data point $\mathbf{x} \in \mathbb{R}^{n\times 1}$ with the learnable parameters represented by $\mathbf{w} \in \mathbb{R}^p$. The typical setting to study NTKs is that of neural networks in the asymptote of infinite width, where the NTK is constant with respect to the learnable parameters during training, in contrast to the finite-width scenario (Jacot et al., 2018). This constancy of the NTK is a result of certain neural networks transitioning to linearity as their width goes to infinity (Liu et al., 2020). NTKs have been leveraged to gain theoretical insights on the behavior of neural networks such as over-parameterized neural networks achieving zero training loss over a non-convex loss landscape (Du et al., 2018), the spectral bias of neural networks (Cao et al., 2021) and the inductive biases of different neural network architectures (Bietti & Mairal, 2019).

In particular, the eigenspectrum of the NTK kernel has been linked with the convergence rate of gradient descent for an over-parameterized deep learning model (Liu et al., 2022; Arora et al., 2019; Wang et al., 2022a). For instance, gradient descent can achieve faster convergence for a supervised learning problem if the vector of output labels, $\mathbf{y}$, aligns well with the dominant eigenvectors of the NTK matrix $\Theta$ (Arora et al., 2019; Wang et al., 2022a). For the regression problem pertaining to predicting $\mathbf{y}$ from $\mathbf{x}$, our analysis in

[1]Department of Electrical and Systems Engineering, University of Pennsylvania, Philadelphia, PA. Correspondence to: Shervin Khalafi <shervink@seas.upenn.edu>.

*Proceedings of the 41st International Conference on Machine Learning*, Vienna, Austria. PMLR 235, 2024. Copyright 2024 by the author(s).

Section 2 demonstrates that

$$\text{Convergence of gradient descent} \propto \mathbf{y}^{\mathsf{T}}\Theta\mathbf{y} \tag{2}$$

By leveraging the observation above as a motivation, we define $\mathbf{y}^{\mathsf{T}}\Theta\mathbf{y}$ as Alignment $\mathcal{A}$.

**Structure in NTKs.** Given that the NTK $\Theta$ depends on input data $\mathbf{x}$ (see (1)), the alignment $\mathcal{A}$ inherently captures some version of covariance between output $\mathbf{y}$ and input $\mathbf{x}$. Thus, if the NTK $\Theta$ is 'structured' for a given predictor $f$, the alignment $\mathcal{A}$ could be leveraged to provide further insights into the design of the predictor $f$. GNNs are an example of a class of predictors for which the NTK is a function of the graph structure and input data $\mathbf{x}$ (Krishnagopal & Ruiz, 2023). GNNs operating on covariance matrices derived from the input data have been studied previously in (Sihag et al., 2022), albeit without any consideration of the insights that could be drawn from the NTKs regarding the choice of graph structure derived from the data for a supervised learning problem. Many of the existing works that analyze NTKs for GNNs focus on explaining empirically observed trends for GNNs (see Appendix A for expanded literature review).

In this paper, we leverage GNNs as learning models in NTKs in our theoretical analyses to motivate neural network learning architecture that depends explicitly on the cross-covariance between the input and the output for an inference task. We associate a matrix representation $S \in \mathbb{R}^{n\times n}$ with the graph structure which we shall call the graph shift operator or GSO (common choices for the GSO in GNNs include adjacency matrix and Laplacian matrix). Then, if the NTK $\Theta$ for a GNN is considered to be a function of the form $\Theta(S, \mathbf{x})$ for a GSO $S$, the alignment can be represented as $\mathcal{A}(S, \mathbf{x}, \mathbf{y})$, i.e., as a function of the input data $\mathbf{x}$, output data $\mathbf{y}$ and $S$. It is then apparent that optimizing the alignment $\mathcal{A}$ for a GNN can inform the choice of the GSO $S$ for a given dataset. A key observation made in this paper is that the alignment $\mathcal{A}$ is characterized by the cross-covariance between the input and the output and as a result, the optimal choice of GSO for statistical inference is closely related to the cross-covariance.

**Contributions.** In this paper, we consider the setting where the predictor $f$ is a GNN with graph filter as the convolution operator (Gama et al., 2020). Our theoretical contributions in this context are summarized next.

- Our analysis of alignment $\mathcal{A}$ with graph filter as the predictor motivates a learning model that leverages the cross-covariance between the input and output data as the graph. More precisely, we pose an optimization problem with alignment $\mathcal{A}$ as the objective function and demonstrate that using the cross-covariance as the GSO maximizes a lower bound on this objective.
- We further extend the results from the graph filter to the scenario of a two-layer GNN as the predictor. Our results show that under certain assumptions, the cross-covariance between the input and the output optimizes a lower bound on the alignment for the GNN that has $\tanh$ activation function. Thus, our analysis motivates a learning model that explicitly depends on cross-covariance based graphs.

We validated the insights drawn from our theoretical results via experiments on the publicly available resting state functional magnetic resonance imaging (rfMRI) data from the Human Connectome Project-Young Adult (HCP-YA) dataset (Van Essen et al., 2012). In particular, we considered the task of time series prediction and observed that the GNNs that operated on the cross-covariance between the input and output data achieved better convergence and generalization than those that used the covariance matrix only from the input data. Further, by leveraging the transferability property of GNNs (Ruiz et al., 2023), our experiments also demonstrated that learning models with cross-covariance graphs outperformed those with covariance graphs even when the GNNs were transferred from a low-dimensional fMRI dataset to a higher-dimensional dataset for the same population.

## 2. Alignment and Convergence of Gradient Descent

In this section, we formalize the concept of alignment $\mathcal{A}$ and demonstrate its relationship with the convergence of gradient descent for a regression problem. Consider a dataset $\{(\mathbf{x}_i, \mathbf{y}_i)\}_{i=1}^{M}$, where $\mathbf{x}_i \in \mathbb{R}^{n\times 1}$, $\mathbf{y}_i \in \mathbb{R}^{n\times 1}$. We aim to leverage the inputs $\mathbf{x}_i$ to estimate the outputs $\mathbf{y}_i$ using a predictor denoted by $\boldsymbol{f} : \mathbb{R}^{n\times 1} \times \mathbb{R}^{p} \to \mathbb{R}^{n}$. We use the notation $\boldsymbol{h} \in \mathbb{R}^{p}$ to denote the vector of all learnable parameters of the predictor. To emphasize the dependence of the predictor $\boldsymbol{f}$ on the parameters $\boldsymbol{h}$, we use the notation $\boldsymbol{f}_{\mathbf{x}_i}(\boldsymbol{h})$ for $\boldsymbol{f}(\mathbf{x}_i, \boldsymbol{h})$ subsequently. Also, the parameters are initialized randomly from a Gaussian distribution $\boldsymbol{h}^{(0)} \sim \mathcal{N}(0, \kappa^2 I)$, where the constant $\kappa$ controls the magnitude of the initialized parameters. The objective is to minimize the mean squared error (MSE) loss function, defined as

$$\Phi(\boldsymbol{h}) \triangleq \min_{\boldsymbol{h}\in\mathbb{R}^{p}} \frac{1}{2}\sum_{i=1}^{M} ||\mathbf{y}_i - \boldsymbol{f}_{\mathbf{x}_i}(\boldsymbol{h})||_2^2 \,. \tag{3}$$

For this purpose, we consider a gradient descent based optimization framework with a learning rate $\eta > 0$. The evolution of the predictor output for a single input $\mathbf{x}_i$ is given by

$$\boldsymbol{f}_{\mathbf{x}_i}(\boldsymbol{h}^{(t+1)}) = \boldsymbol{f}_{\mathbf{x}_i}\big(\boldsymbol{h}^{(t)} - \eta \cdot \nabla\Phi(\boldsymbol{h}^{(t)})\big) \tag{4}$$

where $t$ denotes the $t$-th step or epoch of gradient descent. To characterize the evolution of the predictor output over the entire dataset, we provide the following definitions

$$\tilde{\boldsymbol{f}}_{\mathbf{x}}(\boldsymbol{h}) \triangleq \left[ [\boldsymbol{f}_{\mathbf{x}_1}(\boldsymbol{h})]^{\mathsf{T}},\, [\boldsymbol{f}_{\mathbf{x}_2}(\boldsymbol{h})]^{\mathsf{T}}, \cdots,\, [\boldsymbol{f}_{\mathbf{x}_M}(\boldsymbol{h})]^{\mathsf{T}} \right]^{\mathsf{T}}, \tag{5}$$

$$\tilde{\mathbf{x}} \triangleq \left[\mathbf{x}_1^{\mathsf{T}}, \mathbf{x}_2^{\mathsf{T}}, \cdots, \mathbf{x}_M^{\mathsf{T}}\right]^{\mathsf{T}},\ \tilde{\mathbf{y}} \triangleq \left[\mathbf{y}_1^{\mathsf{T}}, \mathbf{y}_2^{\mathsf{T}}, \cdots, \mathbf{y}_M^{\mathsf{T}}\right]^{\mathsf{T}} \tag{6}$$

where $\tilde{\boldsymbol{f}}_{\mathbf{x}}(\boldsymbol{h}), \tilde{\mathbf{x}}$, and $\tilde{\mathbf{y}}$ are vectors of length $nM$. We also define the NTK matrix $\tilde{\boldsymbol{\Theta}}(\boldsymbol{h}) \in \mathbb{R}^{nM \times nM}$, which consists of $M^2$ number of $n \times n$ blocks, such that, the $(i,j)$-th block is the matrix $\Theta(\mathbf{x}_i, \mathbf{x}_j) \in \mathbb{R}^{n \times n}$ and is given by

$$\Theta(\mathbf{x}_i, \mathbf{x}_j) \triangleq \mathrm{J}_{\boldsymbol{f}_{\mathbf{x}_i}}(\boldsymbol{h}^{(t)})\big(\mathrm{J}_{\boldsymbol{f}_{\mathbf{x}_j}}(\boldsymbol{h}^{(t)})\big)^{\mathsf{T}}. \tag{7}$$

In (7), $\mathrm{J}_{\boldsymbol{f}_{\mathbf{x}_i}}(\boldsymbol{h})$ denotes the Jacobian matrix with its $(a,b)$-th entry being $(\mathrm{J}_{\boldsymbol{f}_{\mathbf{x}_i}}(\boldsymbol{h}))_{ab} = \frac{\partial (\boldsymbol{f}_{\mathbf{x}_i}(\boldsymbol{h}))_a}{\partial h_b}$. If the step size $\eta$ from (4) is sufficiently small, the function $\boldsymbol{f}_{\mathbf{x}_i}\big(\boldsymbol{h}^{(t)}\big)$ can be linearized at each step. In this scenario, the linearized version of the evolution of the predictor output in (4) is

$$\tilde{\boldsymbol{f}}_{\mathbf{x}}(\boldsymbol{h}^{(t+1)}) = \tilde{\boldsymbol{f}}_{\mathbf{x}}(\boldsymbol{h}^{(t)}) - \eta \cdot \tilde{\boldsymbol{\Theta}}(\boldsymbol{h}^{(t)}) \cdot (\tilde{\boldsymbol{f}}_{\mathbf{x}}(\boldsymbol{h}^{(t)}) - \tilde{\mathbf{y}}). \tag{8}$$

A typical setting of interest in the existing literature is that of the NTK $\tilde{\boldsymbol{\Theta}}(\boldsymbol{h}^{(t)})$ being a constant with respect to $\boldsymbol{h}^{(t)}$. This is because the NTK converges to a constant for many neural networks in the infinite width limit (Liu et al., 2020). Theorem 2.1 characterizes the convergence of gradient descent for the considered multivariate regression problem in this setting (also see (Arora et al., 2019), (Wang et al., 2022a)). The NTK that is constant with respect to $\boldsymbol{h}^{(t)}$ is denoted by $\tilde{\boldsymbol{\Theta}}$.

**Theorem 2.1.** *In the multivariate regression setting, as described in the beginning of Section 2, if the NTK $\tilde{\boldsymbol{\Theta}}(\boldsymbol{h}^{(t)})$ is constant during training and $\kappa = \mathcal{O}(\varepsilon\sqrt{\frac{\delta}{nM}})$, then with probability at least $1-\delta$, the training error after $t$ steps of gradient descent is bounded as*

$$\begin{aligned}\tilde{\mathbf{y}}^{\mathsf{T}}\left(I - 2t\eta \cdot \tilde{\boldsymbol{\Theta}}\right)\tilde{\mathbf{y}} \pm \mathcal{O}(\varepsilon) &\leq ||\tilde{\boldsymbol{f}}_{\mathbf{x}}(\boldsymbol{h}^{(t)}) - \tilde{\mathbf{y}}||_2^2 \\ &\leq \tilde{\mathbf{y}}^{\mathsf{T}}\left(I - \eta \cdot \tilde{\boldsymbol{\Theta}}\right)\tilde{\mathbf{y}} \pm \mathcal{O}(\varepsilon)\end{aligned}, \tag{9}$$

*Remark* 2.2. In this paper, we primarily consider two classes of predictors. The first class is that of a linear predictor, for which the NTK is a constant given the definition in (7). The second class of predictors is that of infinitely wide neural networks (GNNs in particular). We refer the reader to Appendix D and (Liu et al., 2020) for a detailed discussion of when and why the NTK is constant for neural networks.

Since the term $\tilde{\mathbf{y}}^{\mathsf{T}}\tilde{\boldsymbol{\Theta}}\tilde{\mathbf{y}}$ characterizes the upper and lower bounds, the loss $||\tilde{\boldsymbol{f}}_{\mathbf{x}}(\boldsymbol{h}^{(t)}) - \tilde{\mathbf{y}}||_2^2$ is proportional to this term. Based on Theorem 2.1, we formalize the alignment in Definition 2.3. A similar definition can be found in (Wang et al., 2022a) in the context of active learning.

**Definition 2.3** (Alignment)**.** The alignment between the output $\tilde{\mathbf{y}}$ and NTK $\tilde{\boldsymbol{\Theta}}$ is defined as

$$\mathcal{A} \triangleq \tilde{\mathbf{y}}^{\mathsf{T}}\tilde{\boldsymbol{\Theta}}\tilde{\mathbf{y}}$$

The alignment $\mathcal{A}$ can be perceived as a metric of correlation between output data and the NTK, and is a characteristic of learning with gradient descent. Using Definition 2.3, Theorem 2.1 can be restated as

$$\tilde{\mathbf{y}}^{\mathsf{T}}\tilde{\mathbf{y}} - 2t\eta \cdot \mathcal{A} \pm \mathcal{O}(\varepsilon) \leq ||\tilde{\boldsymbol{f}}_{\mathbf{x}}(\boldsymbol{h}^{(t)}) - \tilde{\mathbf{y}}||_2^2 \leq \tilde{\mathbf{y}}^{\mathsf{T}}\tilde{\mathbf{y}} - \eta \cdot \mathcal{A} \pm \mathcal{O}(\varepsilon) \tag{10}$$

Equation 10 shows that <u>the convergence of gradient descent is positively correlated with $\mathcal{A}$.</u>

Recall that the NTK $\tilde{\boldsymbol{\Theta}}$ is a function of the input data $\tilde{\mathbf{x}}$ and the learning model $\boldsymbol{f}$, even when constant with respect to $\boldsymbol{h}^{(t)}$. Therefore, maximizing $\mathcal{A}$ is contingent on maximizing some kind of cross-covariance between the output data $\tilde{\mathbf{y}}$ and a function of the input data $\tilde{\mathbf{x}}$, where the function depends on the learning model $\boldsymbol{f}$. This observation motivates us to study the setting where the predictor $\boldsymbol{f}$ is a GNN, as a GNN architecture can provide appropriate structure to analyze the connection between alignment, cross-covariance and the structure of the network.

## 3. Optimizing Alignment motivates Cross-Covariance

To gain further insight into alignment $\mathcal{A}$, we consider GNNs as the predictor $\boldsymbol{f}_{\mathbf{x}}$. The convolution operation for GNNs considered in this paper is modeled by the graph filter. A graph filter is characterized by a linear-shift-and-sum operation on the input data and is representative of a large family of convolution operations in GNNs (see the section 'implementation of GCNNs' from (Gama et al., 2020)). We begin with the setting where $\boldsymbol{f}_{\mathbf{x}}(\boldsymbol{h})$ is a graph filter.

### 3.1. NTK and Alignment for Graph Filter

We formally define a graph filter in Definition 3.1.

**Definition 3.1** (Graph Filter, (Gama et al., 2020))**.** Consider a symmetric GSO $S \in \mathbb{R}^{n \times n}$. A graph filter processes an input $\mathbf{x} \in \mathbb{R}^n$ via a linear-shift-and-sum operation characterized by $S$, such that, its output is

$$\begin{aligned}\boldsymbol{f}_{\mathbf{x}}(\boldsymbol{h}) &= \sum_{k=0}^{K-1} h_k S^k \mathbf{x} = H(S)\mathbf{x}, \\ \text{where } H(S) &\triangleq \sum_{k=0}^{K-1} h_k S^k,\end{aligned} \tag{11}$$

and $\boldsymbol{h} = \{h_0, h_1, \cdots, h_{K-1}\}$ is the set of scalars, also referred to as the filter taps or coefficients.

Recall from (7) that $\tilde{\mathbf{\Theta}}(\boldsymbol{h}^{(t)})$ is a function of the Jacobian matrix $\mathrm{J}_{\boldsymbol{f}_{\mathbf{x}_i}}(\boldsymbol{h}^{(t)})$, which for a graph filter model is given by

$$\mathrm{J}_{\boldsymbol{f}_{\mathbf{x}_i}}(\boldsymbol{h}^{(t)}) = \left[\mathbf{x}_i | S\mathbf{x}_i | S^2\mathbf{x}_i | \cdots | S^{K-1}\mathbf{x}_i\right] \ . \tag{12}$$

Using (12), for any pair of input vectors $(\mathbf{x}_i, \mathbf{x}_j)$, the $(i,j)$-the block of the NTK $\tilde{\mathbf{\Theta}}(\boldsymbol{h}^{(t)})$ for a graph filter is given by $\Theta_{(\mathbf{x}_i,\mathbf{x}_j)}(\boldsymbol{h}^{(t)}) = \sum_{k=0}^{K-1} S^k\mathbf{x}_i(S^k\mathbf{x}_j)^\mathsf{T}$. Since the graph filter is a linear model, $\Theta_{(\mathbf{x}_i,\mathbf{x}_j)}(\boldsymbol{h}^{(t)})$ is independent of $\boldsymbol{h}^{(t)}$. Consequently, the NTK $\Theta_{(\mathbf{x}_i,\mathbf{x}_j)}(\boldsymbol{h}^{(t)})$ for a graph filter is a constant with respect to $\boldsymbol{h}^{(t)}$.

**Proposition 3.2** (NTK for a graph filter)**.** *The NTK for a graph filter is given by*

$$\tilde{\mathbf{\Theta}}_{\mathsf{filt}}(\boldsymbol{h}^{(t)}) = \sum_{k=0}^{K-1} \tilde{S}^k\tilde{\mathbf{x}}\tilde{\mathbf{x}}^\mathsf{T}\tilde{S}^k \ . \tag{13}$$

*where $\tilde{S} \in \mathbb{R}^{nM\times nM}$ is a block diagonal matrix consisting of $M$ repeated blocks equal to matrix $S$ on the diagonal and zeros everywhere else.*

Given (13), we further investigate the impact of shift operator $S$ on the alignment $\mathcal{A}$. Also, we define the data matrices $X, Y$ where $X$ is the input data matrix where the $i$-th column is equal to $\mathbf{x}_i$ and similarly for $Y$. From (13), note that the NTK is independent of the filter coefficients $\boldsymbol{h}$. As a consequence, $\mathcal{A}$ for a graph filter (denoted by $\mathcal{A}_{\mathsf{filt}}$) depends on the shift operator $S$ and dataset $(X,Y)$ as follows

$$\begin{aligned}\mathcal{A}_{\mathsf{filt}}(S,X,Y) \quad &= \quad \tilde{\mathbf{y}}^\mathsf{T}\left(\textstyle\sum_{k=0}^{K-1}\tilde{S}^k\tilde{\mathbf{x}}\tilde{\mathbf{x}}^\mathsf{T}\tilde{S}^k\right)\tilde{\mathbf{y}} \\ = \textstyle\sum_{k=0}^{K-1}\left(\tilde{\mathbf{y}}^\mathsf{T}\tilde{S}^k\tilde{\mathbf{x}}\right)^2 \quad &= \quad \textstyle\sum_{k=0}^{K-1}\left(\mathbf{tr}(Y^\mathsf{T}S^kX)\right)^2\end{aligned} \tag{14}$$

The equivalence between different terms in (14) follows from the symmetry of $\tilde{S}$ and the fact that $\tilde{\mathbf{y}}^\mathsf{T}\tilde{S}^k\tilde{\mathbf{x}}$ is a scalar. Since a larger $\mathcal{A}_{\mathsf{filt}}$ is correlated with faster convergence of gradient descent (see (10)), <u>we further investigate whether the alignment $\mathcal{A}_{\mathsf{filt}}$ can be optimized by appropriate selection of shift operator matrix $S$</u>. The objective to optimize $\mathcal{A}_{\mathsf{filt}}$ can be stated as follows.

$$S^* = \arg\max_S \sum_{k=0}^{K-1}\left(\tilde{\mathbf{y}}^\mathsf{T}\tilde{S}^k\tilde{\mathbf{x}}\right)^2 \ \ \textbf{s.t.}\ \eta\cdot||\tilde{\mathbf{\Theta}}_{\mathsf{filt}}||_{\mathsf{op}} < \alpha \ . \tag{15}$$

The constraint $||\eta\cdot\tilde{\mathbf{\Theta}}_{\mathsf{filt}}||_{\mathsf{op}} < \alpha$, for some $\alpha > 0$, in (15) is necessary to ensure the convergence of gradient descent. This constraint also eliminates trivial solutions (such as multiplying a given $S$ with an arbitrarily large positive constant to inflate $\mathcal{A}$ in isolation). The optimization problem in (15), while meaningful, can be analytically intractable due to complications arising from the polynomial functions of $S$ and the objective function and the constraint being non-convex. In order to provide an analytically tractable solution to $S$, we consider a lower bound on $\mathcal{A}$ next.

**Lemma 3.3.** *[Lower bound on $\mathcal{A}_{\mathsf{filt}}$.] The alignment $\mathcal{A}_{\mathsf{filt}}$ satisfies $\mathcal{A}_{\mathsf{filt}}(S,X,Y) \geq \mathcal{A}_{\mathsf{L}}(S,X,Y)$, where*

$$\mathcal{A}_{\mathsf{L}}(S,X,Y) \triangleq \left(\frac{1}{\sqrt{K}}\boldsymbol{tr}\Big(\Big(\sum_{k=0}^{K-1}S^k\Big)C_{XY}\Big)\right)^2 \ , \tag{16}$$

$$\textit{and} \quad C_{XY} \triangleq \frac{1}{2}(XY^\mathsf{T} + YX^\mathsf{T}) \ . \tag{17}$$

Henceforth, we focus on characterizing $S$ that maximizes $\mathcal{A}_{\mathsf{L}}(S,X,Y)$. Our experiments in Section 4 also demonstrate that the insights drawn from optimizing $\mathcal{A}_{\mathsf{L}}$ are practically meaningful. Next, we provide a constraint that depends on the choice of GSO and not on the input data.

**Lemma 3.4.** *If the degree $K$ polynomial in the shift operator $S$ has a bounded Frobenius norm, the operator norm of the NTK matrix is also bounded as follows:*

$$||\sum_{k=0}^{K-1}S^k||_F \leq \sqrt{\alpha/(\eta M)} \ \Rightarrow \ \eta\cdot||\sum_{k=0}^{K-1}\tilde{S}^k\tilde{\mathbf{x}}\tilde{\mathbf{x}}^\mathsf{T}\tilde{S}^k||_{\mathsf{op}} \leq \alpha \tag{18}$$

The constraint on the left in (18) is more straightforward to work with in the analysis since it only depends on $S$, while also ensuring that the constraint in (15) is satisfied. Putting together $\mathcal{A}_{\mathsf{L}}(S,X,Y)$ and the revised constraint, we get the following <u>optimization problem</u>.

$$\begin{aligned} S^* &= \arg\max_S \ \mathcal{A}_{\mathsf{L}}(S,X,Y) \\ \text{such that } & ||\sum_{k=0}^{K-1}S^k||_F \leq \sqrt{\alpha/(\eta M)} \ . \end{aligned} \tag{19}$$

In the following theorem, we characterize the solution to the optimization problem in (19).

**Theorem 3.5** (GSO in graph filter.)**.** *A GSO $S^*$ that satisfies*

$$\sum_{k=0}^{K-1}(S^*)^k = \mu\cdot C_{XY} \ , \quad \textit{where} \quad \mu = \frac{\sqrt{\alpha/(\eta M)}}{||C_{XY}||_F} \ . \tag{20}$$

*is the solution to the optimization problem in* (19)*.*

Theorem 3.5 clearly demonstrates the association between the optimal GSO that optimizes $\mathcal{A}_{\mathsf{L}}(S,X,Y)$ and $C_{XY}$, which is a measure of cross-covariance. For instance, if $K = 2$, then it can be concluded from (20) that

$$I + S^* = \mu\cdot C_{XY} \Rightarrow S^* = \mu\cdot C_{XY} - I \tag{21}$$

The observation in (21) motivates the potential choice of a normalized cross-covariance matrix as a GSO when the predictor $\boldsymbol{f}_{\mathbf{x}}(\boldsymbol{h})$ is a graph filter. Next, we discuss how this observation extends to the setting where $\boldsymbol{f}_{\mathbf{x}}(\boldsymbol{h})$ is a GNN.

## 3.2. NTK and Alignment for GNNs

To start with, we formalize the GNN architecture that is the focus of our analysis. The ability to learn non-linear mappings by GNNs is fundamentally based on concatenating an element-wise non-linearity with a graph filter to form a graph perceptron, which is realized via a point-wise non-linearity $\sigma(\cdot)$ as $\sigma(H(S)\mathbf{x})$. In the remainder of this paper, we will focus on a two-layer GNN that admits a single input feature $\mathbf{x} \in \mathbb{R}^n$ and the GNN output is a vector of length $n$, as dictated by the problem definition in Section 2. The general definition for a GNN, along with additional experimental results for GNNs that are deeper than two layers have been provided in Appendix F.

**Two-Layer GNN Architecture** (see Fig. 8). In the first layer, the input vector $\mathbf{x} \in \mathbb{R}^n$, is processed by $F$ graph perceptrons to output $F$ $n$-dimensional outputs given by $\mathbf{q}_{(1)}^f, \forall f \in \{1, \cdots, F\}$, as follows

$$\mathbf{u}_{(1)}^f = H_{(1)}^f(S)\mathbf{x} = \sum_{k=0}^{K-1} h_{(1),k}^f S^k \mathbf{x},\ \forall f \in \{1, \ldots, F\}; \tag{22}$$

$$\mathbf{q}_{(1)}^f = \sigma\Big(\mathbf{u}_{(1)}^f\Big) \tag{23}$$

In the second layer, each of the outputs of the previous layer, $\mathbf{q}_{(1)}^f$ are processed by a graph filter as

$$\mathbf{u}_{(2)}^f = H_{(2)}^f(S)\mathbf{q}_{(1)}^f = \sum_{k=0}^{K-1} h_{(2),k}^f S^k \mathbf{q}_{(1)}^f, \forall f \in \{1, \ldots, F\}\ . \tag{24}$$

Finally, the terms $\mathbf{u}_{(2)}^f$ are aggregated to get the output at the second layer (also the GNN output) as

$$\boldsymbol{f}_{\mathbf{x}}(\boldsymbol{h}) = \frac{1}{\sqrt{F}} \sum_{f=1}^{F} \mathbf{u}_{(2)}^f \tag{25}$$

The absence of a non-linearity in the final layer (25) is consistent with the NTK literature and necessary for having a constant NTK in the infinite width limit (Liu et al., 2020).

**Proposition 3.6** (NTK for a two-layer GNN). *The NTK for the two-layer GNN is given by*

$$\begin{aligned}\tilde{\mathbf{\Theta}}_{GNN}(\boldsymbol{h}) \quad &= \quad \frac{1}{F}\sum_{f=1}^{F}\sum_{k=0}^{K-1}\Big(\mathbf{c}_{f,k}^{(1)}\Big)\Big(\mathbf{c}_{f,k}^{(1)}\Big)^{\mathsf{T}} \\ &+ \quad \frac{1}{F}\sum_{f=1}^{F}\sum_{k=0}^{K-1}\Big(\mathbf{c}_{f,k}^{(2)}\Big)\Big(\mathbf{c}_{f,k}^{(2)}\Big)^{\mathsf{T}}\end{aligned} \tag{26}$$

*where*

$$\begin{aligned}\mathbf{c}_{f,k}^{(1)} &\triangleq H_f(\tilde{S}) \cdot \boldsymbol{diag}(\sigma'(G_f(\tilde{S})\tilde{\mathbf{x}})\tilde{S}^k\tilde{\mathbf{x}}), \\ \mathbf{c}_{f,k}^{(2)} &\triangleq \tilde{S}^k \sigma\Big(G_f(\tilde{S})\tilde{\mathbf{x}}\Big)\ .\end{aligned} \tag{27}$$

*In (27), $\mathbf{c}_{f,k}^{(\ell)} \in \mathbb{R}^{nM \times 1}$ is the vector determined by picking out the column that pertains to the derivative of the network output with regards to the parameter indexed by $(f, k, \ell)$, namely, the $k$-th coefficient of the $f$-th filter in layer $\ell$, from every Jacobian matrices $\boldsymbol{J}_{\boldsymbol{f}_{\mathbf{x}_i}}, \forall i \in \{1, \cdots M\}$ and stacking all these vectors together.*

The NTK in (26) is an aggregation of two terms, where the first term is associated with the first layer and the second term with the second layer. It follows from Definition 2.3 and (26) that the alignment for a two-layer GNN is also composed of two terms that represent the two layers. Henceforth, we focus on the results pertaining to the second term in (26) for brevity. This corresponds to a two-layer GNN where only the parameters of the second layer are trained and the parameters of the first layer are fixed. However, this does not impact the generality of our results, since the analysis of the setting when we train both layers is similar (see Appendix E).

In the subsequent discussions, the notation $\tilde{\mathbf{\Theta}}_{GNN}$ denotes the second term in (26) when the width of the hidden layer approaches infinity, i.e., $F \to \infty$. Thus, $\tilde{\mathbf{\Theta}}_{GNN}$ is given by

$$\lim_{F\to\infty} \frac{1}{F}\sum_{f=1}^{F}\sum_{k=0}^{K-1}\Big(\tilde{S}^k\sigma\Big(G_f(\tilde{S})\tilde{\mathbf{x}}\Big)\Big)\Big(\tilde{S}^k\sigma\Big(G_f(\tilde{S})\tilde{\mathbf{x}}\Big)\Big)^{\mathsf{T}} \tag{28}$$

$$= \sum_{k=0}^{K-1}\tilde{S}^k \mathop{\mathbb{E}}_{\boldsymbol{g}\sim\mathcal{N}(0,I)}\Big[\sigma\Big(G(\tilde{S})\tilde{\mathbf{x}}\Big)\Big(\sigma\Big(G(\tilde{S})\tilde{\mathbf{x}}\Big)\Big)^{\mathsf{T}}\Big]\tilde{S}^k \tag{29}$$

$$= \sum_{k=0}^{K-1}\tilde{S}^k E \tilde{S}^k = \tilde{\mathbf{\Theta}}_{GNN} \tag{30}$$

We define the expectation matrix $E$ that is instrumental for the analysis of the alignment as $E \triangleq \mathop{\mathbb{E}}_{\boldsymbol{g}\sim\mathcal{N}(0,I)}\Big[\sigma\Big(G(\tilde{S})\tilde{\mathbf{x}}\Big)\Big(\sigma\Big(G(\tilde{S})\tilde{\mathbf{x}}\Big)\Big)^{\mathsf{T}}\Big]$.

Before proceeding, we provide the following remark pertinent to the analysis.

*Remark* 3.7. As a byproduct of the output layer being linear, the NTK $\tilde{\mathbf{\Theta}}_{GNN}$ in (28) does not depend on the parameters of the second layer, i.e., $\boldsymbol{h}_f, \forall f \in \{1, \cdots, F\}$. Hence, the NTK in (28) could be considered a constant if only the second layer of GNN is trained. For completeness, our discussion in Appendix D demonstrates further that as $F \to \infty$, the NTK in (26) also approaches a constant behavior.

From (28), the alignment can be written in terms of $E$ as

$$\mathcal{A} = \tilde{\mathbf{y}}^{\mathsf{T}}\tilde{\mathbf{\Theta}}_{GNN}\tilde{\mathbf{y}} = \tilde{\mathbf{y}}^{\mathsf{T}}\Big(\sum_{k=0}^{K-1}\tilde{S}^k E \tilde{S}^k\Big)\tilde{\mathbf{y}} = \mathbf{tr}(QE)\ , \tag{31}$$

where we have defined the matrix $Q \triangleq \sum_{k=0}^{K-1} \tilde{S}^k \tilde{\mathbf{y}} \tilde{\mathbf{y}}^\mathsf{T} \tilde{S}^k$. Above, we used the cyclic property of the trace and the fact that $\tilde{\mathbf{y}}^\mathsf{T} \tilde{\boldsymbol{\Theta}}_{GNN} \tilde{\mathbf{y}}$ is a scalar.

In order to evaluate $E$, we define the vectors $\boldsymbol{z}^{(\ell)} \triangleq \left[\tilde{\mathbf{x}}_\ell,\ (\tilde{S}\tilde{\mathbf{x}})_\ell,\ \cdots,\ (\tilde{S}^{K-1}\tilde{\mathbf{x}})_\ell\right]^\mathsf{T} \in \mathbb{R}^{K \times 1}$ where $\ell \in \{1, \cdots, nM\}$ and $(\tilde{S}^k \tilde{\mathbf{x}})_\ell$ denotes the $\ell$-th entry of the vector $\tilde{S}^k \tilde{\mathbf{x}}$ . Using this definition, the $(a, b)$-th entry of the expectation matrix $E$ can be written as

$$E_{ab} = \mathop{\mathbb{E}}_{\boldsymbol{g} \sim \mathcal{N}(0,I)} \left[\sigma\left(\langle \boldsymbol{g}, \boldsymbol{z}^{(a)} \rangle\right) \cdot \sigma\left(\langle \boldsymbol{g}, \boldsymbol{z}^{(b)} \rangle\right)\right] . \tag{32}$$

**Linear GNNs.** We next discuss the scenario when the function $\sigma(\cdot)$ is an identity function, i.e., $\sigma(z) = z$. The results drawn from this setting will be leveraged later in the setting when $\sigma(\cdot)$ is a non-linear activation function. When $\sigma(z) = z$, (32) reduces to

$$E_{ab} = \mathop{\mathbb{E}}_{\boldsymbol{g} \sim \mathcal{N}(0,I)} \left[\langle \boldsymbol{g}, \boldsymbol{z}^{(a)} \rangle \cdot \langle \boldsymbol{g}, \boldsymbol{z}^{(b)} \rangle\right] = \langle \boldsymbol{z}^{(a)}, \boldsymbol{z}^{(b)} \rangle \tag{33}$$

We denote the matrix $E$ in this linear setting by $B_{\mathsf{lin}}$, which is given by

$$(B_{\mathsf{lin}})_{ab} \triangleq \langle \boldsymbol{z}^{(a)}, \boldsymbol{z}^{(b)} \rangle \Rightarrow B_{\mathsf{lin}} = \sum_{k=0}^{K-1} \tilde{S}^k \tilde{\mathbf{x}} \tilde{\mathbf{x}}^\mathsf{T} \tilde{S}^k \tag{34}$$

Thus, the alignment in this linear setting is given by

$$\begin{aligned} \mathcal{A}_{\mathsf{lin}} &\triangleq \mathbf{tr}(QB_{\mathsf{lin}}) = \sum_{k=0}^{K-1} \tilde{\mathbf{y}}^T \tilde{S}^k B \tilde{S}^k \tilde{\mathbf{y}} \\ &= \sum_{k=0}^{K-1} \sum_{k'=0}^{K-1} \tilde{\mathbf{y}}^T \tilde{S}^{k+k'} \tilde{\mathbf{x}} \tilde{\mathbf{x}}^T \tilde{S}^{k+k'} \tilde{\mathbf{y}} \end{aligned} \tag{35}$$

The analysis of alignment $\mathcal{A}_{\mathsf{lin}}$ in (35) using similar arguments as that for a graph filter in Section 3.1 yields a similar condition on the GSO $S$ as in Theorem 3.5. The corollaries provided next formalize this observation. First, the following corollary provides a lower bound on $\mathcal{A}_{\mathsf{lin}}$.

**Corollary 3.8.** *[Lower bound on $\mathcal{A}_{\mathsf{lin}}$] The linear Alignment $\mathcal{A}_{\mathsf{lin}} = \mathbf{tr}(QB_{\mathsf{lin}})$ satisfies $\mathcal{A}_{\mathsf{lin}} \geq \mathcal{A}_{\mathsf{L}'}(S, X, Y)$, where the lower bound $\mathcal{A}_{\mathsf{L}'}(S, X, Y)$ is defined as*

$$\mathcal{A}_{\mathsf{L}'}(S, X, Y) \triangleq \left(\frac{1}{\sqrt{K}} \mathbf{tr}\Big(\Big(\sum_{k=0}^{K-1} \sum_{k'=0}^{K-1} (S^*)^{k+k'}\Big) C_{XY}\Big)\right)^2 , \tag{36}$$

Next, we present an optimization problem similar to the one for the graph filter in (19) next.

$$S^* = \arg\max_{S}\ \mathcal{A}_{\mathsf{L}'}(S, X, Y) \tag{37}$$

$$\textbf{s.t.}\ \|\sum_{k=0}^{K-1} \sum_{k'=0}^{K-1} S^{k+k'}\|_F \leq \sqrt{\alpha/(\eta M)} \tag{38}$$

The solution to the optimization problem in (37) is presented next.

**Corollary 3.9.** *[Extension of Theorem 1 to linear GNN] The GSO $S^*$ that solves the optimization problem in (37) must satisfy*

$$\sum_{k=0}^{K-1} \sum_{k=0}^{K-1} (S^*)^{k+k'} = \mu \cdot C_{XY}\ ,\ \ \textit{where}\ \ \mu = \frac{\sqrt{\alpha/(\eta M)}}{\|C_{XY}\|_F} . \tag{39}$$

Corollary 3.9 establishes that the cross-covariance $C_{XY}$ is instrumental to optimizing $\mathcal{A}_{\mathsf{L}'}$ for the considered two-layer GNN architecture when $\sigma(\cdot)$ is an identity function. In general, this observation holds for linear GNNs of any arbitrary depth.

**GNNs with non-linear activation function.** Next, we investigate the conditions under which the observation in Corollary 3.9 extends to a more general setting, in which $\sigma(\cdot)$ is not the identity function. We will focus our theoretical analysis on the case where, $\sigma(z) = \tanh(z)$ and from here on $\mathcal{A}$ will denote the alignment for this case. The experimental results (see Appendix F) suggest that in practice, similar results hold for other commonly used activation functions like ReLU. First, we evaluate the expectation in (29). By leveraging the theory of Hermite polynomials [1], the Hermite expansions of $\sigma\left(\langle \boldsymbol{g}, \boldsymbol{z}^{(a)} \rangle\right)$ and $\sigma\left(\langle \boldsymbol{g}, \boldsymbol{z}^{(b)} \rangle\right)$ enables the expansion of $E$ and subsequently $\mathcal{A}$. These expansions are formalized next.

**Lemma 3.10** (Expansion of $E$ and $\mathcal{A}$)**.** *The Hermite expansion of $E$ can be written as $E = B + \Delta B$, where $B \in \mathbb{R}^{nM \times nM}$ represents the first non-zero term in the expansion and $\Delta B \in \mathbb{R}^{nM \times nM}$ includes all the subsequent terms. For the $(a, b)$-th element of $B$ and $\Delta B$, we have*

$$\begin{aligned} B_{ab} &= \alpha_1 \beta_1 \cdot \frac{\langle \boldsymbol{z}^{(a)}, \boldsymbol{z}^{(b)} \rangle}{\|\boldsymbol{z}^{(a)}\|_2 \cdot \|\boldsymbol{z}^{(b)}\|_2}, \\ (\Delta B)_{ab} &= \sum_{i=3,5,\cdots}^{\infty} \alpha_i \beta_i \cdot \left(\frac{\langle \boldsymbol{z}^{(a)}, \boldsymbol{z}^{(b)} \rangle}{\|\boldsymbol{z}^{(a)}\|_2 \cdot \|\boldsymbol{z}^{(b)}\|_2}\right)^i . \end{aligned} \tag{40}$$

*Hence, the alignment $\mathcal{A}$ in (31) admits the expansion*

$$\mathcal{A} = \mathbf{tr}(QE) = \mathbf{tr}(QB) + \mathbf{tr}(Q\Delta B) . \tag{41}$$

The scalar coefficients $\alpha_i, \beta_i$ in (40) depend on $\|\boldsymbol{z}^{(a)}\|_2$ and $\|\boldsymbol{z}^{(b)}\|_2$, respectively and the choice of $\sigma(\cdot)$.

Expanding the alignment into the two terms in (41) is useful because the first term is closely related to the linear alignment $\mathcal{A}_{\mathsf{lin}}$ and the second term is relatively small. Therefore, the expansion lets us relate alignment in the non-linear case,

[1]See the proof of Lemma 3.10 for an overview of the Hermite polynomials and how we utilized the Hermite expansion.

$\mathcal{A}$, to the linear alignment $\mathcal{A}_{\mathsf{lin}}$. The following lemmas and Theorem formalize this.

**Lemma 3.11.** *Given a family of matrices $S \in \mathbb{S}^{n\times n}$ that have a bounded norm, $||S||_{\mathsf{op}} \leq \nu$, we have*

$$\rho_{\mathsf{min}}\mathcal{A}_{\mathsf{lin}} \leq \textbf{\textit{tr}}(QB) \leq \rho_{\mathsf{max}}\mathcal{A}_{\mathsf{lin}}, \tag{42}$$

*where $\rho_{\mathsf{min}}, \rho_{\mathsf{max}} > 0$ are constants that depend on $\nu$ and the choice of non-linearity $\sigma(\cdot)$.*

We remark that the condition $||S||_{\mathsf{op}} \leq \nu$ is necessary since to compare different shift operators both in practice and in our theorems, we need to normalize the choices of GSO to have the same Frobenius norm. The second term in the expansion, i.e. $\mathbf{tr}(Q\Delta B)$, is harder to directly analyze, therefore we relate it to the first term to make analysis more tractable in the following lemma.

**Lemma 3.12.** *Each element of $\Delta B$ has the same sign as the corresponding element in $B$. Also, the following element-wise inequality holds between the two matrices:*

$$|\Delta B| \leq \beta \cdot |B| \tag{43}$$

*where $\beta$ is a constant that depends on our choice of non-linearity and is determined from the proof.*

While Lemma 3.12 suggests that the contribution of the second term is smaller than the first, in order to make this rigorous, we will need the following assumption:

$$\mathcal{A}_{\mathsf{lin}} \geq \xi ||Q||_F ||B_{\mathsf{lin}}||_F$$

for some constant $0 < \xi \leq 1$. We will shortly discuss what this assumption implies, but by leveraging it, we derive a lower bound in Theorem 3.13 for the alignment in the non-linear setting.

**Theorem 3.13.** *Given a family of matrices $S \in \mathbb{S}^{n\times n}$ that have a bounded norm, $||S||_{\mathsf{op}} \leq \nu$ and that satisfy $\mathcal{A}_{\mathsf{lin}} = \textbf{\textit{tr}}\,(QB_{\mathsf{lin}}) \geq \xi \cdot ||Q||_F ||B_{\mathsf{lin}}||_F$ for some constant $0 < \xi \leq 1$, $\mathcal{A}_{\mathsf{lin}}$ lower bounds the alignment for the two-layer GNN with $\tanh$ non-linearity, $\mathcal{A}$, up to a constant as follows*

$$\left(c - \frac{d}{\xi}\right)\mathcal{A}_{\mathsf{lin}} \leq \mathcal{A}\ , \tag{44}$$

*for positive constants $c \triangleq \rho_{\mathsf{min}}\left(1 + \frac{\beta}{2}\right)$ and $d \triangleq \frac{\beta\rho_{\mathsf{max}}}{2}$.*

We now provide an intuitive explanation for the conditions that enable Theorem 3.13 to be practically relevant. If the linear alignment is not negligible, i.e. when $\mathcal{A}_{\mathsf{lin}} \geq \xi \cdot \|Q\|\, ||B_{\mathsf{lin}}||$ with $\xi > \frac{d}{c}$, then Theorem 3.13 guarantees a non-trivial lower bound on the alignment in the non-linear setting. Specifically, Theorem 3.13 establishes that when the linear alignment is not negligible, the alignment in the non-linear case is also not negligible and is at least a factor of $\mathcal{A}_{\mathsf{lin}}$. Thus, optimizing $\mathcal{A}_{\mathsf{lin}}$ provides a condition for the optimality for $\mathcal{A}$ that can translate to improved performance.

If the assumption in Theorem 3.13 does not hold with sufficiently large $\xi$, then the linear alignment $\mathcal{A}_{\mathsf{lin}}$ is too small, which means that the linear model (characterized by only graph filters) is not a good fit for the regression task at hand. In such a scenario, we cannot make any guarantees for alignment in the non-linear case or, specifically, guarantee a good performance with the addition of non-linear activation functions to the model. We note that the constants can be evaluated numerically to check the validity of the lower bound. Clearly, for the bound to be non-vacuous, $c - \frac{d}{\xi}$ should be positive, which happens only when $\xi > \frac{d}{c}$. As an example, using $\tanh$ and normalizing $S$ to have norm $||S||_{\mathsf{op}} \leq \nu = 0.5$ we get $\frac{d}{c} \simeq 0.7$.

These observations, together with Corollary 3.9, motivate using the cross-covariance matrix $C_{XY}$ as a GSO for the two-layer GNN.

**Alignment, The NTK and Generalization.** Thus far, we have provided the theoretical results motivated by the fact that larger alignment can imply faster convergence of gradient descent during training. However, alignment and NTK are also closely related to generalization. Specifically, the analyses pertaining to generalization from (Arora et al., 2019), (Wang et al., 2022a) can be extended to the case of graph filters, which leads to the conclusion that larger alignment could also lead to smaller generalization error. Hence, the results on improved training and generalization together motivate models with larger alignment in practice. The generalization analysis has been provided in Appendix C.

## 4. Experiments

In this section, we provide the experiments that validate the theoretical insights pertaining to the cross-covariance being an optimal graph to use as a GSO for GNN training and generalization as opposed to graphs derived only from the input data (such as correlation or covariance graphs) for a regression task. The dataset and inference task for this purpose are described below.

**Data.** The HCP-YA dataset is a publicly available brain imaging dataset collected over a population of 1003 healthy adults in the age range of 22–35 years (Van Essen et al., 2012; 2013). In our experiments, we leveraged the rfMRI data for each subject made available by HCP. This data consisted of a multi-variate time series of 100 features, with each time series consisting of 4500 time points.

**Inference task.** Noting that the 100 features could be considered as 100 nodes of a graph, our objective was to use the data at all nodes at the current time step for an individual to predict the data at all nodes at a future time step. Specifically, given the signal value at time step $t$ as $\boldsymbol{z}^{(t)} \in \mathbb{R}^{100}$ for an individual, our goal was to predict the signal value after $\Delta t$ time steps, i.e., $\boldsymbol{z}^{(t+\Delta t)} \in \mathbb{R}^{100}$. For every $\Delta t \in \{1, 2, 3, 4, 5\}$, a separate training/test set of size $N_{train} = 1000$, $N_{test} = 100$ was created, such that, for the signal at a time point $t$, i.e., $\boldsymbol{z}^{(t)}$ as the input, the signal after $\Delta t$ time steps $\boldsymbol{z}^{(t+\Delta t)}$ was the output to be predicted. For additional implementation details, see Appendix F.

**Performance evaluation.** We trained two sets of GNNs and two sets of graph filters using the time series data of each individual for a given $\Delta t$, where one set comprised of predictors with $C_{XY}$ as the GSO and the other with $C_{XX}$ as the GSO. The GNNs with $C_{XX}$ as GSO have been studied before as VNNs in (Sihag et al., 2022) and provide an appropriate baseline for comparison as it is representative of GNNs with GSOs extracted only from the input data (see Appendix F.7). Figure 1 illustrates faster convergence of training loss during gradient descent for predictors with $C_{XY}$ as compared to those with $C_{XX}$ for one representative individual when $\Delta t = 1$. This observation was consistent for graph filters and GNNs. For each individual, the training process for every architecture was repeated 10 times. The average of these runs is shown in Fig.1.

Further, we checked whether these observations were consistent across the dataset and for different $\Delta t$. Fig.2 illustrates the gap between the test error for predictors with $C_{XY}$ and $C_{XX}$ and different values of $\Delta t$, averaged across all individuals. Even as the prediction accuracy diminished with increasing $\Delta t$, we observed a consistent gain in test performance when using $C_{XY}$ as compared to $C_{XX}$. Similarly, Fig.3 shows that predictors with $C_{XY}$ achieved smaller training error relative to those with $C_{XX}$ at each epoch of gradient descent, averaged across the dataset. Thus, Figs.1-3 validate the theoretical insights from the analysis that argued for $C_{XY}$ as an appropriate GSO for GNNs that can achieve smaller training error and better generalization.

We note that in our presented results the covariance graph, $C_{XX}$, is representative of a broader class of graph constructions using the input such as graphs based on Pearson correlation or Euclidean distance with Gaussian kernel. See Appendix F.7 for details.

**Transferability.** The convolution operation for GNNs in (11) has a scale-free characteristic, as the learnable parameters are independent of the dimensionality of the dataset. Thus, in general, a GNN can be transferred across graphs of arbitrary sizes by replacing the GSO in (11). This property of GNN architecture allows us to investigate the transference of GNN from the training dataset to a target dataset with any arbitrary number of features. Successful transference of GNN-based architectures across multi-

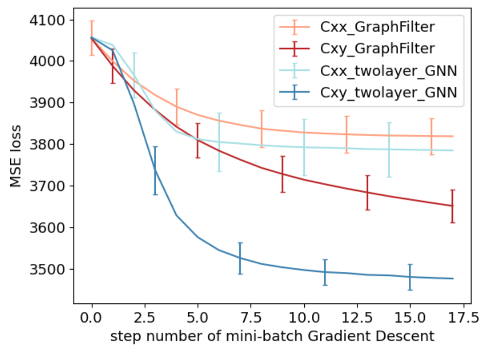

*Figure 1.* Training loss for one individual in HCP-YA dataset.

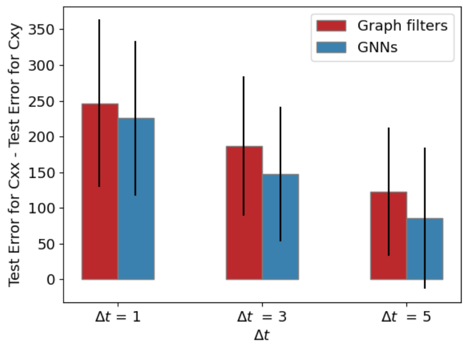

*Figure 2.* **Generalization.** The gap between the final test error for $C_{XY}$ and $C_{XX}$ for different predictors averaged over the complete dataset of individuals.

resolution datasets has previously been demonstrated in (Sihag et al., 2023). In the HCP-YA dataset, we have multivariate time series of different dimensionalities, namely $n = 15, 25, 50, 100, 200, 300$, for each individual. We further expanded the scope of our experiments by deploying GNNs trained on a lower dimensional time series dataset to a higher dimensional dataset to investigate whether cross-covariance graphs outperformed covariance graphs even after transferring the GNN models. Fig.4 demonstrates the gap between the final test loss of predictors using $C_{XY}$ and $C_{XX}$ in two scenarios: (i) GNN trained on data with 100 features for an individual and tested on unseen 100-dimensional data for the same individual; and (ii) GNN trained on data with 50 features for an individual and tested on data with 100 features for the same individual. Thus, the first setting acts as a baseline to evaluate the quality of transference in the second setting. We note that the relative decrease in loss of the models using $C_{XY}$ as opposed to $C_{XX}$ in both scenarios is similar. Thus, we conclude that using $C_{XY}$ is just as beneficial in the transfer scenario. We also remark that the additional loss incurred by transferring the model is very small for both the graph filter and GNN models regardless of the choice of shift operator (See Fig 14 in Appendix F) which shows the GNNs transfer success-

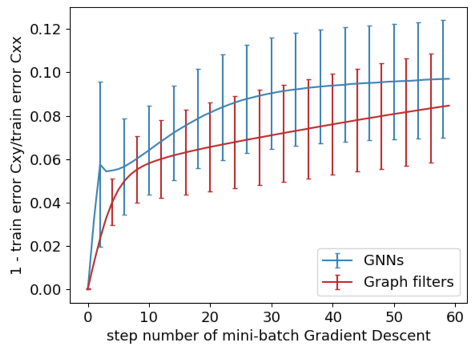

*Figure 3.* **Convergence.** Improvement in training error at different epochs of gradient descent averaged over the complete dataset of individuals.

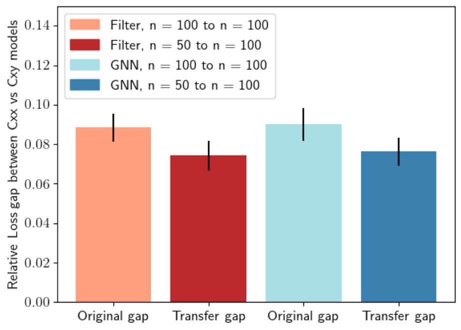

*Figure 4.* **Transferability.** The gap between final test loss of predictors using $C_{XY}$ and $C_{XX}$ in two scenarios: (i) Model trained and tested on dataset with $n = 100$ features; (ii) Model trained on data with $n = 50$ and tested on data with $n = 100$.

fully from 50-feature dataset to 100-feature dataset. This transferability setting provides the unique perspective to the optimality of cross-covariance graphs relative to covariance graphs for inference, which would be infeasible to investigate for learning models with number of learnable parameters dependent on the dimensionality of the dataset (e.g., fully connected neural networks). A brief summary of additional experimental details and results found in Appendix F is provided next.

**Additional Experiments.** In Section F.1, we demonstrate results on time series prediction for two other datasets. In Section F.2, we provide additional details on the inference task described in the main text. In Section F.3, we define multi-layer GNNs and show empirically that the benefit of using cross-covariance based networks extends to GNNs deeper than two layers. In Sections F.4 and F.5, we empirically analyse the effects of changing the non-linear activation function and the number of filter taps, $K$, to validate that the merit of our approach is independent of these architectural details. In Section F.6, we consider a more practically relevant inference task of time series prediction using more than just one previous time step and we extend our approach to that framework. In Section F.7, we compare the results of using a cross-covariance graph to methods of constructing a graph from input data commonly found in the literature to emphasize the benefit of also using the output data in constructing a graph.

## 5. Conclusions

In this paper, we have demonstrated that the analysis of NTKs in the context of GNNs motivates the use of cross-covariance graphs. Specifically, we have shown that for a two-layer GNN, choosing the cross-covariance matrix between the input and output data as the Graph Shift Operator maximized lower bounds on the alignment (a measure of correlation between the NTK and the available dataset) and this alignment, in turn, governed the convergence rate and generalization properties of the predictor. We have validated that GNNs with cross-covariance graphs indeed outperformed GNNs with covariance graphs (which are representative of GNNs with graphs obtained only using the input data) in a time-series prediction task on three different datasets. The cross-covariance based GNNs exhibited faster convergence and smaller training and test errors, and these empirical observations even extended to GNNs with the number of layers larger than two.

A main limitation of this work is the restricted focus on a dataset with input and output vectors of the same dimensionalities. Such a setting lends itself well to the use of GNN architectures and makes their theoretical analysis tractable. However, in general, the inputs and outputs for multi-variate regression problems can have different dimensionalities. Deriving similar results for such cases is a potential avenue for future work. Another limitation of our theoretical contributions is the lack of thorough analysis of the tightness of the lower bounds analyzed.

Other graph-based ML models, such as Graph Attention Networks (Veličković et al., 2018), could also potentially benefit from our novel theoretical approach of alignment optimization. Additionally, there are many existing works that combine GNNs and transformers for improved prediction accuracy in the time-series prediction task. Investigating whether our results can provide further insights or improvements in such models is a future direction of interest.

## Impact Statement

This paper presents work whose goal is to advance the field of Machine Learning. There are many potential societal consequences of our work, none which we feel must be specifically highlighted here.

## References

Adlam, B. and Pennington, J. Understanding double descent requires a fine-grained bias-variance decomposition. Advances in neural information processing systems, 33: 11022–11032, 2020.

Akiba, T., Sano, S., Yanase, T., Ohta, T., and Koyama, M. Optuna: A next-generation hyperparameter optimization framework. In Proceedings of the 25th ACM SIGKDD International Conference on Knowledge Discovery and Data Mining, 2019.

Arora, S., Du, S., Hu, W., Li, Z., and Wang, R. Fine-grained analysis of optimization and generalization for overparameterized two-layer neural networks. In International Conference on Machine Learning, pp. 322–332. PMLR, 2019.

Bietti, A. and Mairal, J. On the inductive bias of neural tangent kernels. Advances in Neural Information Processing Systems, 32, 2019.

Cao, D., Wang, Y., Duan, J., Zhang, C., Zhu, X., Huang, C., Tong, Y., Xu, B., Bai, J., Tong, J., et al. Spectral temporal graph neural network for multivariate time-series forecasting. Advances in neural information processing systems, 33:17766–17778, 2020.

Cao, Y., Fang, Z., Wu, Y., Zhou, D.-X., and Gu, Q. Towards understanding the spectral bias of deep learning. In 30th International Joint Conference on Artificial Intelligence (IJCAI 2021), pp. 2205–2211. International Joint Conferences on Artificial Intelligence, 2021.

Chen, C., Petty, K., Skabardonis, A., Varaiya, P., and Jia, Z. Freeway performance measurement system: Mining loop detector data. Transportation Research Record, 1748(1): 96–102, 2001. doi: 10.3141/1748-12. URL https://doi.org/10.3141/1748-12.

Chen, W., Gong, X., and Wang, Z. Neural architecture search on imagenet in four gpu hours: A theoretically inspired perspective. In International Conference on Learning Representations (ICLR), 2021.

Du, S. S., Zhai, X., Poczos, B., and Singh, A. Gradient descent provably optimizes over-parameterized neural networks. In International Conference on Learning Representations, 2018.

Du, S. S., Hou, K., Salakhutdinov, R. R., Poczos, B., Wang, R., and Xu, K. Graph neural tangent kernel: Fusing graph neural networks with graph kernels. In Wallach, H., Larochelle, H., Beygelzimer, A., d'Alché-Buc, F., Fox, E., and Garnett, R. (eds.), Advances in Neural Information Processing Systems, volume 32. Curran Associates, Inc., 2019.

Gama, F., Marques, A. G., Leus, G., and Ribeiro, A. Convolutional neural network architectures for signals supported on graphs. IEEE Transactions on Signal Processing, 67(4):1034–1049, 2019.

Gama, F., Isufi, E., Leus, G., and Ribeiro, A. Graphs, convolutions, and neural networks: From graph filters to graph neural networks. IEEE Signal Processing Magazine, 37 (6):128–138, 2020.

Höskuldsson, A. PLS regression methods. Journal of chemometrics, 2(3):211–228, 1988.

Huang, W., Li, Y., weitao Du, Xu, R., Yin, J., Chen, L., and Zhang, M. Towards deepening graph neural networks: A GNTK-based optimization perspective. In International Conference on Learning Representations, 2022. URL https://openreview.net/forum?id=tT9t_ZctZRL.

Jacot, A., Gabriel, F., and Hongler, C. Neural tangent kernel: Convergence and generalization in neural networks. In Bengio, S., Wallach, H., Larochelle, H., Grauman, K., Cesa-Bianchi, N., and Garnett, R. (eds.), Advances in Neural Information Processing Systems, volume 31. Curran Associates, Inc., 2018.

Kingma, D. P. and Ba, J. Adam: A method for stochastic optimization. arXiv preprint arXiv:1412.6980, 2014.

Krishnagopal, S. and Ruiz, L. Graph neural tangent kernel: Convergence on large graphs. International Conference on Machine Learning, 2023.

LeCun, Y., Bengio, Y., and Hinton, G. Deep learning. Nature, 521(7553):436, 2015.

Lin, L. and Dobriban, E. What causes the test error? going beyond bias-variance via ANOVA. The Journal of Machine Learning Research, 22(1):6925–7006, 2021.

Liu, C., Zhu, L., and Belkin, M. On the linearity of large non-linear models: when and why the tangent kernel is constant. Advances in Neural Information Processing Systems, 33:15954–15964, 2020.

Liu, C., Zhu, L., and Belkin, M. Loss landscapes and optimization in over-parameterized non-linear systems and neural networks. Applied and Computational Harmonic Analysis, 59:85–116, 2022.

Maurer, A. A vector-contraction inequality for rademacher complexities. In Ortner, R., Simon, H. U., and Zilles, S. (eds.), Algorithmic Learning Theory, pp. 3–17, Cham, 2016. Springer International Publishing. ISBN 978-3-319-46379-7.

Mei, S. and Montanari, A. The generalization error of random features regression: Precise asymptotics and the double descent curve. Communications on Pure and Applied Mathematics, 75(4):667–766, 2022.

Mei, S., Montanari, A., and Nguyen, P.-M. A mean field view of the landscape of two-layer neural networks. Proceedings of the National Academy of Sciences, 115 (33), jul 2018.

Mei, S., Misiakiewicz, T., and Montanari, A. Mean-field theory of two-layers neural networks: dimension-free bounds and kernel limit. In Beygelzimer, A. and Hsu, D. (eds.), Proceedings of the Thirty-Second Conference on Learning Theory, volume 99 of Proceedings of Machine Learning Research, pp. 2388–2464. PMLR, 25–28 Jun 2019.

O'Donnell, R. Analysis of boolean functions. Cambridge University Press, 2014.

Paszke, A., Gross, S., Massa, F., Lerer, A., Bradbury, J., Chanan, G., Killeen, T., Lin, Z., Gimelshein, N., Antiga, L., et al. Pytorch: An imperative style, high-performance deep learning library. Advances in neural information processing systems, 32, 2019.

Qiao, L., Zhang, L., Chen, S., and Shen, D. Data-driven graph construction and graph learning: A review. Neurocomputing, 312:336–351, 2018. ISSN 0925-2312. doi: https://doi.org/10.1016/j.neucom.2018.05.084. URL https://www.sciencedirect.com/science/article/pii/S0925231218306696.

Ruiz, L., Chamon, L. F., and Ribeiro, A. Transferability properties of graph neural networks. IEEE Transactions on Signal Processing, 2023.

Sabanayagam, M., Esser, P., and Ghoshdastidar, D. New insights into graph convolutional networks using neural tangent kernels. arXiv preprint arXiv:2110.04060, 2021.

Sabanayagam, M., Esser, P., and Ghoshdastidar, D. Representation power of graph convolutions: Neural tangent kernel analysis. arXiv preprint arXiv:2210.09809, 2022.

Shalev-Shwartz, S. and Ben-David, S. Understanding Machine Learning - From Theory to Algorithms. Cambridge University Press, 2014. ISBN 978-1-10-705713-5.

Sihag, S., Mateos, G., McMillan, C., and Ribeiro, A. coVariance neural networks. Proc. Advances in Neural Information Processing Systems, 35:17003–17016, 2022.

Sihag, S., Mateos, G., McMillan, C. T., and Ribeiro, A. Transferablility of covariance neural networks and application to interpretable brain age prediction using anatomical features. arXiv preprint arXiv:2305.01807, 2023.

Sirignano, J. and Spiliopoulos, K. Mean field analysis of neural networks: A central limit theorem. Stochastic Processes and their Applications, 130(3):1820–1852, 2020.

Van Essen, D. C., Ugurbil, K., Auerbach, E., Barch, D., Behrens, T. E., Bucholz, R., Chang, A., Chen, L., Corbetta, M., Curtiss, S. W., et al. The human connectome project: a data acquisition perspective. Neuroimage, 62 (4):2222–2231, 2012.

Van Essen, D. C., Smith, S. M., Barch, D. M., Behrens, T. E., Yacoub, E., Ugurbil, K., Consortium, W.-M. H., et al. The WU-Minn human connectome project: an overview. Neuroimage, 80:62–79, 2013.

Veličković, P., Cucurull, G., Casanova, A., Romero, A., Liò, P., and Bengio, Y. Graph attention networks, 2018.

Wang, H., Huang, W., Wu, Z., Tong, H., Margenot, A. J., and He, J. Deep active learning by leveraging training dynamics. Advances in Neural Information Processing Systems, 35:25171–25184, 2022a.

Wang, S., Yu, X., and Perdikaris, P. When and why PINNs fail to train: A neural tangent kernel perspective. Journal of Computational Physics, 449:110768, 2022b.

Zhu, Z., Liu, F., Chrysos, G., and Cevher, V. Generalization properties of nas under activation and skip connection search. Advances in Neural Information Processing Systems, 35:23551–23565, 2022.

## A. Additional Literature Review

**Analysis of GNNs with NTKs.** (Du et al., 2019) prove that the NTK for GNNs can learn a broad class of functions on graphs. (Sabanayagam et al., 2021) use the GNTK as a hyperparameter-free surrogate for GNNs to empirically analyze the effect of increasing depth and using skip connections on the performance of GNNs. They also show that the GNTK captures the performance trend of the corresponding finite-width GNNs. (Krishnagopal & Ruiz, 2023) analyze how the graph size affects the GNTK and shows that as the graph gets larger the GNTK converges to the graphon NTK. (Sabanayagam et al., 2022) use the GNTK to theoretically (and empirically) explain the effects of different architecture choices such as symmetric vs row normalization and increasing depth on GNN performance.

**Empirical implications of theoretical insights derived using NTKs.** Existing studies have used the theoretical insights drawn from NTKs to understand practical observations and inform practical applications. The studies in (Chen et al., 2021) and (Zhu et al., 2022) leverage NTKs to study theory-inspired neural architecture search protocols. Insights into convergence and generalization properties of neural networks derived using NTKs are well known (Jacot et al., 2018). The training dynamics of physics inspired neural networks were studied using NTKs in (Wang et al., 2022b) and an NTK-inspired gradient descent algorithm was proposed. (Huang et al., 2022) utilize insights gained from NTK-based analysis of the optimization of GNNs to explain the degrading performance of GNNs as the number of layers increases. They further suggest a potential solution to this problem through randomly dropping a certain percentage of the edges of the graph during training. Our work is similar in spirit to such studies, where we draw upon the theoretical insights derived from NTKs in the context of GNNs to motivate the choice of GSO for an inference task.

**Relation to other statistical methods.** Cross-covariance graphs in GNNs for regression models could be tied in principle with the traditional statistical approaches for multi-variate regression approaches, such as partial least squares (PLS) regression (Höskuldsson, 1988). Specifically, PLS regression relies on finding a hyperplane that maximizes the cross-covariance between the latent spaces of input and output data for a regression problem. While our work does not rely on any artificial dimensionality reduction, equivalence between information processing using GNNs over covariance matrices and underlying principal components have been demonstrated previously (Sihag et al., 2022). In this context, establishing the foundational analyses of GNNs that operate on cross-covariance graphs is of immediate interest.

## B. Proofs

### B.1. Proof of Theorem 2.1

*Proof.* Gradient descent is deployed to minimize the following cost

$$\Phi(\boldsymbol{h}) \triangleq \min_{\boldsymbol{h}\in\mathbb{R}^p} \frac{1}{2}\sum_{i=1}^{M} ||\mathbf{y}_i - \boldsymbol{f}_{\mathbf{x}_i}(\boldsymbol{h})||_2^2 \,. \tag{45}$$

The change in predictor output at the $t$-th step of gradient descent can be written as

$$\boldsymbol{f}_{\mathbf{x}_i}(\boldsymbol{h}^{(t+1)}) = \boldsymbol{f}_{\mathbf{x}_i}\big(\boldsymbol{h}^{(t)} - \eta\cdot\nabla\Phi(\boldsymbol{h}^{(t)})\big) \tag{46}$$

Assuming $\eta$ to be sufficiently small we can linearize $\boldsymbol{f}_{\mathbf{x}_i}$ near the point $\boldsymbol{h}^{(t)}$:

$$\boldsymbol{f}_{\mathbf{x}_i}\big(\boldsymbol{h}^{(t)} - \eta\cdot\nabla\Phi(\boldsymbol{h}^{(t)})\big) = \boldsymbol{f}_{\mathbf{x}_i}\big(\boldsymbol{h}^{(t)}\big) - \eta\cdot \mathrm{J}_{\boldsymbol{f}_{\mathbf{x}_i}}(\boldsymbol{h}^{(t)})\cdot\nabla\Phi(\boldsymbol{h}^{(t)})\,, \tag{47}$$

where $\mathrm{J}_{\boldsymbol{f}_{\mathbf{x}_i}}(\boldsymbol{h}^{(t)})$ is the Jacobian matrix of the vector-valued function $\boldsymbol{f}_{\mathbf{x}_i}$, evaluated at point $\boldsymbol{h}^{(t)}$. We can also write the gradient of the loss function $\Phi(\boldsymbol{h})$ in terms of the Jacobians $\mathrm{J}_{\boldsymbol{f}_{\mathbf{x}_j}}$ as follows:

$$\nabla\Phi(\boldsymbol{h}^{(t)}) = \sum_{j=1}^{M}\big(\mathrm{J}_{\boldsymbol{f}_{\mathbf{x}_j}}(\boldsymbol{h}^{(t)})\big)^{\mathsf{T}}\cdot(\boldsymbol{f}_{\mathbf{x}_j}(\boldsymbol{h}^{(t)}) - \mathbf{y}_j) \tag{48}$$

Putting (46) and (47) and (48) together we get:

$$\begin{aligned} \boldsymbol{f}_{\mathbf{x}_i}(\boldsymbol{h}^{(t+1)}) &= \boldsymbol{f}_{\mathbf{x}_i}(\boldsymbol{h}^{(t)}) - \eta \cdot \sum_{j=1}^{M} \mathrm{J}_{\boldsymbol{f}_{\mathbf{x}_i}}(\boldsymbol{h}^{(t)}) \big(\mathrm{J}_{\boldsymbol{f}_{\mathbf{x}_j}}(\boldsymbol{h}^{(t)})\big)^{\mathsf{T}} \cdot (\boldsymbol{f}_{\mathbf{x}_j}(\boldsymbol{h}^{(t)}) - \mathbf{y}_j) \\ &= \boldsymbol{f}_{\mathbf{x}_i}(\boldsymbol{h}^{(t)}) - \eta \cdot \sum_{j=1}^{M} \Theta(\mathbf{x}_i, \mathbf{x}_j) \cdot (\boldsymbol{f}_{\mathbf{x}_j}(\boldsymbol{h}^{(t)}) - \mathbf{y}_j) \end{aligned} , \tag{49}$$

where the $n \times n$ matrix $\Theta(\mathbf{x}_i, \mathbf{x}_j)$ is defined as the product of two Jacobian matrices (which corresponds to the inner product of two gradient vectors that appears in the scalar output case; (see (1)):

$$\Theta(\mathbf{x}_i, \mathbf{x}_j) = \mathrm{J}_{\boldsymbol{f}_{\mathbf{x}_i}}(\boldsymbol{h}^{(t)}) \big(\mathrm{J}_{\boldsymbol{f}_{\mathbf{x}_j}}(\boldsymbol{h}^{(t)})\big)^{\mathsf{T}} \tag{50}$$

Further, (49) can be re-written in the vectorized form as follows

$$\tilde{\boldsymbol{f}}_X(\boldsymbol{h}^{(t+1)}) = \tilde{\boldsymbol{f}}_X(\boldsymbol{h}^{(t)}) - \eta \cdot \tilde{\boldsymbol{\Theta}}(\boldsymbol{h}^{(t)}) \cdot (\tilde{\boldsymbol{f}}_X(\boldsymbol{h}^{(t)}) - \tilde{\mathbf{y}}) \tag{51}$$

If the NTK matrix $\tilde{\boldsymbol{\Theta}}(\boldsymbol{h}^{(t)})$ is constant or non-evolving with respect to epoch $t$, we can use (51) to analyze the evolution of gradient descent as follows:

$$\begin{aligned} \tilde{\boldsymbol{f}}_X(\boldsymbol{h}^{(t+1)}) - \tilde{\mathbf{y}} &= \tilde{\boldsymbol{f}}_X(\boldsymbol{h}^{(t)}) - \tilde{\mathbf{y}} - \eta \cdot \tilde{\boldsymbol{\Theta}} \cdot (\tilde{\boldsymbol{f}}_X(\boldsymbol{h}^{(t)}) - \tilde{\mathbf{y}}) \\ &= (I - \eta \cdot \tilde{\boldsymbol{\Theta}})(\tilde{\boldsymbol{f}}_X(\boldsymbol{h}^{(t)}) - \tilde{\mathbf{y}}) \\ &= (I - \eta \cdot \tilde{\boldsymbol{\Theta}})^{t+1}(\tilde{\boldsymbol{f}}_X(\boldsymbol{h}^{(0)}) - \tilde{\mathbf{y}}) \\ &= -(I - \eta \cdot \tilde{\boldsymbol{\Theta}})^{t+1}\tilde{\mathbf{y}} + (I - \eta \cdot \tilde{\boldsymbol{\Theta}})^{t+1}\tilde{\boldsymbol{f}}_X(\boldsymbol{h}^{(0)}) \end{aligned} , \tag{52}$$

where we have used the notation $\tilde{\boldsymbol{\Theta}}$ to denote an NTK matrix with constant behavior. By choosing the initialization to be small i.e., choosing a small $\kappa$, we can ensure that $\tilde{\boldsymbol{f}}_X(\boldsymbol{h}^{(0)})$ is sufficiently close to 0. Recall that the parameters are initialized randomly as

$$\boldsymbol{h}^{(0)} \sim \mathcal{N}(\mathbf{0}, \kappa^2 I). \tag{53}$$

We can thus say that the output at initialization is 0 in expectation and that the variance of each entry of the output vector is also proportional to $\kappa^2$:

$$\mathbb{E}\left[\tilde{\boldsymbol{f}}_X(\boldsymbol{h}^{(0)})\right] = \mathbf{0},\ \mathbb{E}\left[\left(\tilde{\boldsymbol{f}}_X(\boldsymbol{h}^{(0)})\right)_\ell^2\right] = \mathcal{O}(\kappa^2) \tag{54}$$

where $\left(\tilde{\boldsymbol{f}}_X(\boldsymbol{h}^{(0)})\right)_\ell$ denotes the $\ell$-th entry of the vector $\tilde{\boldsymbol{f}}_X(\boldsymbol{h}^{(0)})$. Since $\tilde{\boldsymbol{f}}_X(\boldsymbol{h}^{(0)})$ is a vector of $nM$ independently initialized entries we have $\mathbb{E}\left[||\tilde{\boldsymbol{f}}_X(\boldsymbol{h}^{(0)})||_2^2\right] = \mathcal{O}(nM\kappa^2)$. Therefore, using Markov's inequality, we obtain

$$\mathbb{P}\left(||\tilde{\boldsymbol{f}}_X(\boldsymbol{h}^{(0)})||_2^2 \geq \frac{nM\kappa^2}{\delta}\right) \leq \delta \tag{55}$$

If we choose $\kappa = \mathcal{O}(\varepsilon\sqrt{\frac{\delta}{nM}})$ we have with probability at least $1 - \delta$ that $||\tilde{\boldsymbol{f}}_X(\boldsymbol{h}^{(0)})||_2 < \varepsilon$ which leads to the following:

$$||(I - \eta \cdot \tilde{\boldsymbol{\Theta}})^{t+1}\tilde{\boldsymbol{f}}_X(\boldsymbol{h}^{(0)})||_2 \leq ||(I - \eta \cdot \tilde{\boldsymbol{\Theta}})^{t+1}||_{\mathsf{op}}||\tilde{\boldsymbol{f}}_X(\boldsymbol{h}^{(0)})||_2 \leq \underbrace{(1 - \eta\lambda_{\mathsf{min}})^{t+1}}_{\mathcal{O}(1)}\underbrace{||\tilde{\boldsymbol{f}}_X(\boldsymbol{h}^{(0)})||_2}_{\mathcal{O}(\varepsilon)} \tag{56}$$

Therefore $||(I - \eta \cdot \tilde{\boldsymbol{\Theta}})^{t+1}\tilde{\boldsymbol{f}}_X(\boldsymbol{h}^{(0)})||_2$ has $\mathcal{O}(\varepsilon)$ behavior. Then from (52) we can write:

$$||\tilde{\boldsymbol{f}}_X(\boldsymbol{h}^{(t+1)}) - \tilde{\mathbf{y}}||_2 = ||(I - \eta \cdot \tilde{\boldsymbol{\Theta}})^{t+1}\tilde{\mathbf{y}}||_2 \pm \mathcal{O}(\varepsilon) \tag{57}$$

Since $\varepsilon$ can be chosen to be arbitrarily small, we subsequently focus only on the term $(I - \eta \cdot \tilde{\mathbf{\Theta}})^{t+1}\tilde{\mathbf{y}}$. From (52) we have

$$\tilde{\boldsymbol{f}}_X(\boldsymbol{h}^{(t)}) - \tilde{\mathbf{y}} = -(I - \eta \cdot \tilde{\mathbf{\Theta}})^t \cdot \tilde{\mathbf{y}} \pm \mathcal{O}\left(\varepsilon\sqrt{\frac{\delta}{nM}}\right) \tag{58}$$

Because $\tilde{\mathbf{\Theta}}$ is symmetric with real valued entries, its eigen-decomposition, when $\mathsf{rank}(\tilde{\mathbf{\Theta}}) = r$, is given by

$$\tilde{\mathbf{\Theta}} \;=\; \sum_{\ell=1}^{r} \lambda_\ell \boldsymbol{v}_\ell \boldsymbol{v}_\ell^{\mathsf{T}} \tag{59}$$

(59) implies the following eigen-decomposition for $(I - \eta \cdot \tilde{\mathbf{\Theta}})$:

$$I - \eta \cdot \tilde{\mathbf{\Theta}} \;=\; \sum_{\ell=1}^{r}(1-\eta\lambda_\ell)\boldsymbol{v}_\ell \boldsymbol{v}_\ell^{\mathsf{T}} + \sum_{\ell=r+1}^{nM} 1 \cdot \boldsymbol{v}_\ell \boldsymbol{v}_\ell^{\mathsf{T}} \tag{60}$$

Using (60) we rewrite (58) as

$$\begin{aligned}\tilde{\boldsymbol{f}}_X(\boldsymbol{h}^{(t)}) - \tilde{\mathbf{y}} &= -\Big(\sum_{\ell=1}^{r}(1-\eta\lambda_\ell)\boldsymbol{v}_\ell \boldsymbol{v}_\ell^{\mathsf{T}} + \sum_{\ell=r+1}^{nM} 1 \cdot \boldsymbol{v}_\ell \boldsymbol{v}_\ell^{\mathsf{T}}\Big)^t \tilde{\mathbf{y}} \pm \mathcal{O}\left(\varepsilon\sqrt{\frac{\delta}{nM}}\right) \\ &= -\sum_{\ell=1}^{r}((1-\eta\lambda_\ell)^{\mathsf{T}} \boldsymbol{v}_\ell^{\mathsf{T}}\tilde{\mathbf{y}})\,\boldsymbol{v}_\ell - \sum_{\ell=r+1}^{nM}(\boldsymbol{v}_\ell^{\mathsf{T}}\tilde{\mathbf{y}})\,\boldsymbol{v}_\ell \pm \mathcal{O}\left(\varepsilon\sqrt{\frac{\delta}{nM}}\right)\end{aligned} \tag{61}$$

Using the fact that the eigenvectors form an orthonormal basis we can write the training loss after $t$ steps of Gradient Descent as

$$||\tilde{\boldsymbol{f}}_X(\boldsymbol{h}^{(t)}) - \tilde{\mathbf{y}}||_2^2 = \sum_{\ell=1}^{r}(1-\eta\lambda_\ell)^{2t}(\boldsymbol{v}_\ell^{\mathsf{T}}\tilde{\mathbf{y}})^2 + \sum_{\ell=r+1}^{nM}(\boldsymbol{v}_\ell^{\mathsf{T}}\tilde{\mathbf{y}})^2 \pm \mathcal{O}(\varepsilon) \tag{62}$$

In (62) we can see how the non-zero eigenvalues of the NTK and the corresponding eigenvectors characterize the training process:

1. Of the two sums in (62), $\sum_{\ell=r+1}^{nM}(\boldsymbol{v}_\ell^{\mathsf{T}}\tilde{\mathbf{y}})^2$ remains constant during training. Therefore it is the hard limit for the minimum achievable training error and cannot be optimized.
2. Each summand in $\sum_{\ell=1}^{r}(1-\eta\lambda_\ell)^{2t}(\boldsymbol{v}_\ell^{\mathsf{T}}\tilde{\mathbf{y}})^2$, converges linearly to zero. The rate of convergence is determined by $(1-\eta\lambda_\ell)^2$ i.e., the larger $\lambda_\ell$ is, the faster the convergence.
3. From the previous two points we can surmise that if $\tilde{\mathbf{y}}$ is well-aligned with the eigenvectors of the NTK that correspond to its larger eigenvalues i.e., $(\boldsymbol{v}_\ell^{\mathsf{T}}\tilde{\mathbf{y}})^2$ is large whenever $\lambda_\ell$ is large, we'll have faster convergence.
4. We know that since the eigenvectors form a basis, $\sum_{\ell=1}^{nM}(\boldsymbol{v}_\ell^{\mathsf{T}}\tilde{\mathbf{y}})^2 = ||\tilde{\mathbf{y}}||_2^2$ which is constant. Therefore the more of $\tilde{\mathbf{y}}$ that is aligned with the eigenvectors of the NTK with non-zero eigenvalues, the smaller the final training error ( after a large enough number of steps) will be.

Next, we combine the above insights to derive the result in Theorem 1. First, for simplicity, we write (62) as

$$||\tilde{\boldsymbol{f}}_X(\boldsymbol{h}^{(t)}) - \tilde{\mathbf{y}}||_2^2 = \sum_{\ell=1}^{nM}(1-\eta\lambda_\ell)^{2t}(\boldsymbol{v}_\ell^{\mathsf{T}}\tilde{\mathbf{y}})^2 \pm \mathcal{O}(\varepsilon) \tag{63}$$

considering that that only the first $r$ eigenvalues are non-zero. Then we have:

$$\begin{aligned}\textstyle\sum_{\ell=1}^{nM}(1-\eta\lambda_\ell)^{2t}(\boldsymbol{v}_\ell^{\mathsf{T}}\tilde{\mathbf{y}})^2 &\le \sum_{\ell=1}^{nM}(1-\eta\lambda_\ell)(\boldsymbol{v}_\ell^{\mathsf{T}}\tilde{\mathbf{y}})^2 \\ &= \tilde{\mathbf{y}}^{\mathsf{T}}\left(\sum_{\ell=1}^{nM}(1-\eta\lambda_\ell)\boldsymbol{v}_\ell\boldsymbol{v}_\ell^{\mathsf{T}}\right)\tilde{\mathbf{y}} \\ &= \tilde{\mathbf{y}}^{\mathsf{T}}\left(I - \eta \cdot \tilde{\mathbf{\Theta}}\right)\tilde{\mathbf{y}}\end{aligned} \tag{64}$$

(64) gives the desired upper bound. Now we move on to the lower bound for (63). Using Bernoulli's inequality which states $(1+x)^m \geq 1+mx$ for every integer $m \geq 1$ and real number $x > -1$ we can write:

$$\begin{aligned} \textstyle\sum_{\ell=1}^{nM}(1-\eta\lambda_\ell)^{2t}(\boldsymbol{v}_\ell^\top \tilde{\mathbf{y}})^2 &\geq \sum_{\ell=1}^{nM}(1-2t\eta\lambda_\ell)(\boldsymbol{v}_\ell^\top \tilde{\mathbf{y}})^2 \\ &= \tilde{\mathbf{y}}^\top \left(\sum_{\ell=1}^{nM}(1-2t\eta\lambda_\ell)\boldsymbol{v}_\ell \boldsymbol{v}_\ell^\top\right)\tilde{\mathbf{y}} \\ &= \tilde{\mathbf{y}}^\top \left(I - 2t\eta\cdot\tilde{\mathbf{\Theta}}\right)\tilde{\mathbf{y}} \end{aligned} \tag{65}$$

Note that in order for gradient descent to converge, $\eta$ must be small enough so that for all $\ell$, $\eta\lambda_\ell \leq 1$. This leads to the condition for Bernoulli's inequality to also be satisfied i.e., $-\eta\lambda_\ell \geq -1$. Putting together the upper bound from (64) and the lower bound from (65) we can bound the quantity in (63) from both sides:

$$\tilde{\mathbf{y}}^\top \left(I - 2t\eta\cdot\tilde{\mathbf{\Theta}}\right)\tilde{\mathbf{y}} \pm \mathcal{O}(\varepsilon) \leq \sum_{\ell=1}^{nM}(1-\eta\lambda_\ell)^{2t}(\boldsymbol{v}_\ell^\top \tilde{\mathbf{y}})^2 \leq \tilde{\mathbf{y}}^\top \left(I - \eta\cdot\tilde{\mathbf{\Theta}}\right)\tilde{\mathbf{y}} \pm \mathcal{O}(\varepsilon) \tag{66}$$

which concludes the proof. □

### B.2. Proof of Lemma 3.3

*Proof.*

$$\begin{aligned} \mathcal{A}_{\mathsf{filt}}(S,X,Y) &= \sum_{k=0}^{K-1}\left(\tilde{\mathbf{y}}^\top \tilde{S}^k \tilde{\mathbf{x}}\right)^2 \\ &= \sum_{k=0}^{K-1}\left(\sum_{i=1}^{M}\mathbf{y}_i^\top S^k \mathbf{x}_i\right)^2 \\ &= \sum_{k=0}^{K-1}\left(\mathbf{tr}(Y^\top S^k X)\right)^2 \end{aligned} \tag{67}$$

Using the cyclic property of the trace (and symmetry of $S^k$) we can write:

$$\mathbf{tr}(Y^\top S^k X) = \mathbf{tr}(S^k X Y^\top) = \mathbf{tr}(X Y^\top S^k) = \mathbf{tr}(S^k Y X^\top) \tag{68}$$

Using the above and (67), we have:

$$\mathcal{A}_{\mathsf{filt}}(S,X,Y) = \sum_{k=0}^{K-1}\left(\frac{1}{2}\left(\mathbf{tr}(S^k X Y^\top) + \mathbf{tr}(S^k Y X^\top)\right)\right)^2 \tag{69}$$

$$= \sum_{k=0}^{K-1}\left(\mathbf{tr}(S^k \cdot \frac{1}{2}(XY^\top + YX^\top))\right)^2 \tag{70}$$

$$= \sum_{k=0}^{K-1}\left(\mathbf{tr}(S^k C_{XY})\right)^2 \geq \left(\frac{1}{\sqrt{K}}\sum_{k=0}^{K-1}\left|\mathbf{tr}(S^k C_{XY})\right|\right)^2 \tag{71}$$

$$\geq \left(\frac{1}{\sqrt{K}}\left|\sum_{k=0}^{K-1}\mathbf{tr}(S^k C_{XY})\right|\right)^2 = \underbrace{\left(\frac{1}{\sqrt{K}}\mathbf{tr}\left(\left(\sum_{k=0}^{K-1}S^k\right)C_{XY}\right)\right)^2}_{\mathcal{A}_{\mathsf{L}}} \tag{72}$$

Above in (71) we used the triangle inequality and in (71) we used the fact that for any vector $\boldsymbol{z} \in \mathbb{R}^d$: $||\boldsymbol{z}||_2 \geq \frac{1}{\sqrt{d}}||\boldsymbol{z}||_1$.[2] □

[2]A relevant question: When are these inequalities tight? whenever the terms $\mathbf{tr}(S^k C_{XY})$ are close to each other for different values of $k$, the inequalities are tighter. If $\mathbf{tr}(S^k C_{XY})$ is the same for every value of $k$, equality holds for both inequalities

## B.3. Proof of Lemma 3.4

*Proof.* Starting with the original constraint: $||\sum_{k=0}^{K-1} \tilde{S}^k \tilde{\mathbf{x}}\tilde{\mathbf{x}}^\mathsf{T} \tilde{S}^k||_{\mathsf{op}} < \alpha.$ , we will use upper bounds to get rid of the dependence on the data and to have a constraint that only depends on $S$:

$$||\sum_{k=0}^{K-1} \tilde{S}^k \tilde{\mathbf{x}}\tilde{\mathbf{x}}^\mathsf{T} \tilde{S}^k||_{\mathsf{op}} \leq \sum_{k=0}^{K-1} ||\tilde{S}^k \tilde{\mathbf{x}}\tilde{\mathbf{x}}^\mathsf{T} \tilde{S}^k||_{\mathsf{op}} = \sum_{k=0}^{K-1} ||\tilde{S}^k \tilde{\mathbf{x}}||_2^2 \tag{73}$$

Above, we used the fact that $\tilde{S}^k \tilde{\mathbf{x}}\tilde{\mathbf{x}}^\mathsf{T} \tilde{S}^k$ is a rank one matrix with its only non-zero eigenvalue being $||\tilde{S}^k \tilde{\mathbf{x}}||_2^2$.

$$\sum_{k=0}^{K-1} ||\tilde{S}^k \tilde{\mathbf{x}}||_2^2 = \sum_{k=0}^{K-1} \sum_{i=1}^{M} ||S^k \mathbf{x}_i||_2^2 = \sum_{k=0}^{K-1} \sum_{i=1}^{M} \mathbf{x}_i^\mathsf{T} S^{2k} \mathbf{x}_i \tag{74}$$

The eigen-decomposition of $S$ is given by

$$S = \sum_{\ell=1}^{n} \gamma_\ell \boldsymbol{v}_\ell \boldsymbol{v}_\ell^\mathsf{T} \ . \tag{75}$$

Inserting (75) into (74) leads to

$$\sum_{k=0}^{K-1} \sum_{i=1}^{M} \mathbf{x}_i^\mathsf{T} S^{2k} \mathbf{x}_i = \sum_{k=0}^{K-1} \sum_{i=1}^{M} \sum_{\ell=1}^{n} \gamma_\ell^{2k} (\boldsymbol{v}_\ell^\mathsf{T} \mathbf{x}_i)^2 \tag{76}$$

Using the notation $\hat{x}_i$ to denote $\boldsymbol{v}_\ell^\mathsf{T}$, we have

$$\sum_{k=0}^{K-1} \sum_{i=1}^{M} \sum_{\ell=1}^{n} \gamma_\ell^{2k} (\boldsymbol{v}_\ell^\mathsf{T} \mathbf{x}_i)^2 = \sum_{k=0}^{K-1} \sum_{i=1}^{M} \langle \boldsymbol{\gamma}^{\odot 2k}, \hat{\mathbf{x}}_i^{\odot 2} \rangle \tag{77}$$

By the linearity of the inner product and Holder's inequality (noting that every element of both vectors is non-negative),

$$\sum_{k=0}^{K-1} \sum_{i=1}^{M} \langle \boldsymbol{\gamma}^{\odot 2k}, \hat{\mathbf{x}}_i^{\odot 2} \rangle = \langle \sum_{k=0}^{K-1} \boldsymbol{\gamma}^{\odot 2k}, \sum_{i=1}^{M} \hat{\mathbf{x}}_i^{\odot 2} \rangle \leq ||\sum_{k=0}^{K-1} \boldsymbol{\gamma}^{\odot 2k}||_1 \cdot ||\sum_{i=1}^{M} \hat{\mathbf{x}}_i^{\odot 2}||_\infty \tag{78}$$

Since $\hat{\mathbf{x}}_i$ consists of the coefficients of $\mathbf{x}_i$ projected onto the eigenspace of $S$, and recall that the input dataset is normalized, i.e., $||\hat{\mathbf{x}}_i||_2 = ||\mathbf{x}_i||_2 = 1$, the term $||\sum_{i=1}^{M} \hat{\mathbf{x}}_i^{\odot 2}||_\infty$ in (78) can be upper bounded as

$$||\sum_{i=1}^{M} \hat{\mathbf{x}}_i^{\odot 2}||_\infty \leq \sum_{i=1}^{M} ||\hat{\mathbf{x}}_i^{\odot 2}||_\infty \leq \sum_{i=1}^{M} ||\hat{\mathbf{x}}_i^{\odot 2}||_1 = \sum_{i=1}^{M} ||\hat{\mathbf{x}}_i||_2^2 \leq M \tag{79}$$

Using the upper bound from (79) we can further upper bound the quantity from (78):

$$\begin{aligned} \sum_{k=0}^{K-1} \sum_{i=1}^{M} \langle \boldsymbol{\gamma}^{\odot 2k}, \hat{\mathbf{x}}_i^{\odot 2} \rangle &\leq M \cdot ||\sum_{k=0}^{K-1} \boldsymbol{\gamma}^{\odot 2k}||_1 \\ &= M \cdot ||\sum_{k=0}^{K-1} \boldsymbol{\gamma}^{\odot k}||_2^2 \\ &= M \cdot ||\sum_{k=0}^{K-1} S^k||_F^2 \end{aligned} \tag{80}$$

Putting together equations (73) - (80) we get:

$$||\sum_{k=0}^{K-1} S^k||_F \leq \sqrt{\alpha/(\eta M)} \Rightarrow \eta \cdot ||\sum_{k=0}^{K-1} \tilde{S}^k \tilde{\mathbf{x}}\tilde{\mathbf{x}}^\mathsf{T} \tilde{S}^k||_{\mathsf{op}} \leq \alpha \tag{81}$$

which concludes the proof. □

## B.4. Proof of Theorem 3.5

*Proof.* We restate the optimization problem to be considered for the result in this theorem.

$$S^* = \arg\max_S \left(\frac{1}{\sqrt{K}}\mathbf{tr}\left(\left(\sum_{k=0}^{K-1} S^k\right) C_{XY}\right)\right)^2 \quad \mathbf{s.t.} \;\; ||\sum_{k=0}^{K-1} S^k||_F \le \sqrt{\alpha/(\eta M)} \tag{82}$$

The vectorized form of (82) is given by

$$\mathbf{vec}(S^*) = \arg\max_{\mathbf{vec}(S)} \left(\frac{1}{\sqrt{K}}\langle \mathbf{vec}(\sum_{k=0}^{K-1} S^k), \mathbf{vec}(C_{XY})\rangle\right)^2 \quad \mathbf{s.t.} \;\; ||\mathbf{vec}(\sum_{k=0}^{K-1} S^k)||_2 \le \sqrt{\alpha/(\eta M)} \tag{83}$$

Thus, (83) is equivalent to maximizing the projection of the vector $\mathbf{vec}(\sum_{k=0}^{K-1} S^k)$ along the direction of $\mathbf{vec}(C_{XY})$ on an $\ell_2$-norm ball of radius $\sqrt{\alpha/(\eta M)}$, which has the following solution

$$\sum_{k=0}^{K-1} (S^*)^k = \mu \cdot C_{XY} \tag{84}$$

where $\mu = \frac{\sqrt{\alpha/(\eta M)}}{||C_{XY}||_F}$ is a normalizing constant to ensure the Frobenius norm of $\sum_{k=0}^{K-1}(S^*)^k$ satisfies our constraint. Note that while a solution $S^*$ satisfying (84) might not exist for some values of $K$, When designing the architecture we could choose $K$ in a way that (84) has a solution. For example with $K = 2$ there is always a solution as given by (21). □

## B.5. Proof of Lemma 3.10

*Proof.* From (32), we can write:

$$\begin{aligned} E_{ab} &= \mathop{\mathbb{E}}_{\boldsymbol{g}\sim\mathcal{N}(0,I)}\left[\sigma\left(\langle \boldsymbol{g}, \boldsymbol{z}^{(a)}\rangle\right)\cdot\sigma\left(\langle \boldsymbol{g}, \boldsymbol{z}^{(b)}\rangle\right)\right] \\ &= \mathop{\mathbb{E}}_{\boldsymbol{g}\sim\mathcal{N}(0,I)}\left[\sigma\left(||\boldsymbol{z}^{(a)}||_2\cdot\langle \boldsymbol{g}, \frac{\boldsymbol{z}^{(a)}}{||\boldsymbol{z}^{(a)}||_2}\rangle\right)\cdot\sigma\left(||\boldsymbol{z}^{(b)}||_2\cdot\langle \boldsymbol{g}, \frac{\boldsymbol{z}^{(b)}}{||\boldsymbol{z}^{(b)}||_2}\rangle\right)\right] \end{aligned} \tag{85}$$

In order to analyze (85), we define two random variables $u \triangleq \langle \boldsymbol{g}, \frac{\boldsymbol{z}^{(a)}}{||\boldsymbol{z}^{(a)}||_2}\rangle$ an $u' \triangleq \langle \boldsymbol{g}, \frac{\boldsymbol{z}^{(b)}}{||\boldsymbol{z}^{(b)}||_2}\rangle$. It is evident that the random variables $u, u'$ are correlated, mean-zero Gaussian random variables with their joint distribution given by

$$u, u' \sim \mathcal{N}\left(\begin{bmatrix}0\\0\end{bmatrix}, \Lambda = \begin{bmatrix} 1 & \frac{\langle \boldsymbol{z}^{(a)}, \boldsymbol{z}^{(b)}\rangle}{||\boldsymbol{z}^{(a)}||_2\cdot||\boldsymbol{z}^{(b)}||_2} \\ \frac{\langle \boldsymbol{z}^{(a)}, \boldsymbol{z}^{(b)}\rangle}{||\boldsymbol{z}^{(a)}||_2\cdot||\boldsymbol{z}^{(b)}||_2} & 1 \end{bmatrix}\right) \tag{86}$$

Therefore from (85) we can write

$$E_{ab} = \mathop{\mathbb{E}}_{u,u'\sim\mathcal{N}(0,\Lambda)}\left[\sigma\left(||\boldsymbol{z}^{(a)}||_2\cdot u\right)\cdot\sigma\left(||\boldsymbol{z}^{(b)}||_2\cdot u'\right)\right] \tag{87}$$

In order to analyze $E_{ab}$, we leverage Hermite polynomials, which are discussed next.

**Hermite Polynomials.** Hermite polynomials are a collection of functions $(p_j)_{j\in\mathbb{N}}$ which form an orthonormal basis for the space of square-integrable functions. The first few of these polynomials can be seen below:

$$p_0(z) = 1, \quad p_1(z) = z, \quad p_2(z) = \frac{z^2-1}{\sqrt{2}}, \quad p_3(z) = \frac{z^3-3z}{\sqrt{6}}, \quad \ldots \tag{88}$$

We can define the inner product between two square-integrable functions $f$ and $g$ as

$$\langle f, g\rangle = \int_{-\infty}^{\infty} f(z)\cdot g(z)\cdot e^{-z^2/2}dz \tag{89}$$

By noting that the Hermite polynomials are orthonormal with respect to the inner product defined in (89), we can expand any function $f(z)$ for which $\langle f, f\rangle$ is bounded, in terms of these polynomials:

$$f(z) = \sum_{\ell=0}^{\infty} \alpha_\ell \cdot p_\ell(z) \tag{90}$$

where we have

$$\alpha_\ell = \langle f, p_l\rangle = \int_{-\infty}^{\infty} f(z) \cdot p_\ell(z) \cdot e^{-z^2/2} dz \tag{91}$$

In our analysis, we also leverage another property of these polynomials (section 11.2 of O'Donnell (2014)), which is given by

$$\underset{\substack{(z,z') \\ \rho\text{-correlated}}}{\mathbb{E}} [p_j(z) p_k(z')] = \begin{cases} \rho^j & \text{if } j = k, \\ 0 & \text{if } j \neq k \end{cases} \tag{92}$$

Essentially, (92) establishes orthogonality of the polynomials $p_j(z)$ and $p_k(z')$ when $(z, z')$ are a pair of $\rho$-correlated standard Gaussian random variables. It is straightforward to see that setting $\rho = 1$ in (92) recovers the orthonormality of the Hermite polynomials. Based on (91) can now write the Hermite expansion of the two functions in (87) as:

$$\sigma\left(||\boldsymbol{z}^{(a)}||_2 \cdot u\right) = \sum_{\ell=0}^{\infty} \alpha_\ell \cdot p_\ell(u), \;\; \sigma\left(||\boldsymbol{z}^{(b)}||_2 \cdot u'\right) = \sum_{\ell'=0}^{\infty} \beta_{\ell'} \cdot p_{\ell'}(u') \tag{93}$$

Inserting these into (87) we get

$$\begin{aligned} E_{ab} &= \underset{u,u' \sim \mathcal{N}(0,\Lambda)}{\mathbb{E}} \left[ \sum_{\ell=0}^{\infty} \alpha_\ell \cdot p_\ell(u) \sum_{\ell'=0}^{\infty} \beta_{\ell'} \cdot p_{\ell'}(u') \right] & (94) \\ &= \sum_{\ell=0}^{\infty} \sum_{\ell'=0}^{\infty} \alpha_\ell \beta_{\ell'} \underset{u,u' \sim \mathcal{N}(0,\Lambda)}{\mathbb{E}} [p_\ell(u) p_{\ell'}(u')] & (95) \\ &= \sum_{\ell=0}^{\infty} \alpha_\ell \beta_\ell \cdot \left(\frac{\langle \boldsymbol{z}^{(a)}, \boldsymbol{z}^{(b)}\rangle}{||\boldsymbol{z}^{(a)}||_2 \cdot ||\boldsymbol{z}^{(b)}||_2}\right)^\ell & (96) \end{aligned}$$

where to get from (95) to (96) we used the orthogonality property of Hermite polynomials from (92). Here, we remark that the coefficients $\alpha_\ell, \beta_\ell$ depend on the choice of non-linear activation function and the magnitudes $||\boldsymbol{z}^{(a)}||_2$ and $||\boldsymbol{z}^{(b)}||_2$ respectively.

For the subsequent analysis, we consider the setting where the non-linear activation function is the hyperbolic tangent function, i.e., $\sigma(y) = \tanh(y)$. Note that $\tanh$ is an odd function. Since the Hermite polynomial $p_\ell(z)$ is odd for odd $\ell$ and even for even $\ell$, for even $\ell$ we have

$$\alpha_\ell = \int_{-\infty}^{\infty} \sigma(||\boldsymbol{z}_a||_2 u) \cdot p_\ell(u) \cdot e^{-u^2/2} du = 0 \tag{97}$$

and similarly we have $\beta_\ell = 0$. This leaves us with only the odd terms in the sum from (96), therefore we can write $E_{ab}$ as

$$E_{ab} = \underbrace{\alpha_1 \beta_1 \cdot \frac{\langle \boldsymbol{z}^{(a)}, \boldsymbol{z}^{(b)}\rangle}{||\boldsymbol{z}^{(a)}||_2 \cdot ||\boldsymbol{z}^{(b)}||_2}}_{B_{ab}} + \underbrace{\sum_{\ell=3,5,\cdots}^{\infty} \alpha_\ell \beta_\ell \cdot \left(\frac{\langle \boldsymbol{z}^{(a)}, \boldsymbol{z}^{(b)}\rangle}{||\boldsymbol{z}^{(a)}||_2 \cdot ||\boldsymbol{z}^{(b)}||_2}\right)^\ell}_{\Delta B_{ab}} \tag{98}$$

For conciseness moving forward, we define the matrices $B \in \mathbb{R}^{nM \times nM}$ which represents the first non-zero term in the expansion and $\Delta B \in \mathbb{R}^{nM \times nM}$ which includes all the subsequent terms. Now, recalling (31) and replacing $E$ with the expansion given in (98), the alignment $\mathcal{A}$ is given by

$$\mathcal{A} = \mathbf{tr}(QE) = \mathbf{tr}(QB) + \mathbf{tr}(Q\Delta B) \,. \tag{99}$$

Hence, we conclude the proof. □

### B.6. Proof of Lemma 3.11

*Proof.* We begin with the analysis of the $(a, b)$-th entry of matrix $B$, i.e.,

$$B_{ab} = \alpha_1 \beta_1 \cdot \frac{\langle \boldsymbol{z}^{(a)}, \boldsymbol{z}^{(b)} \rangle}{||\boldsymbol{z}^{(a)}||_2 \cdot ||\boldsymbol{z}^{(b)}||_2} \tag{100}$$

For this purpose, we define the nonlinear function $\hat{\sigma}(\cdot)$ as

$$\hat{\sigma}(||\boldsymbol{z}_a||_2^2) \triangleq \frac{\alpha_1}{||\boldsymbol{z}_a||_2} \tag{101}$$

$$= \frac{\int_{-\infty}^{\infty} \sigma(||\boldsymbol{z}_a||_2 u) \cdot p_1(u) \cdot e^{-u^2/2} du}{||\boldsymbol{z}_a||_2} \tag{102}$$

By noting that $(B_{\mathsf{lin}})_{aa} = \langle \boldsymbol{z}_a, \boldsymbol{z}_a \rangle = ||\boldsymbol{z}_a||_2^2$, we can write:

$$B_{ab} = \hat{\sigma}((B_{\mathsf{lin}})_{aa}) \cdot \hat{\sigma}((B_{\mathsf{lin}})_{bb}) \cdot (B_{\mathsf{lin}})_{ab} \tag{103}$$

The element-wise equation in (103) implies the following:

$$B = \hat{\sigma}(\textbf{diag}(B_{\mathsf{lin}}))B_{\mathsf{lin}}\hat{\sigma}(\textbf{diag}(B_{\mathsf{lin}})) \tag{104}$$

where $\textbf{diag}(B_{\mathsf{lin}})$ is a square $nM \times nM$ matrix equal to $B_{\mathsf{lin}}$ on the diagonal and zero everywhere else. Next, we focus on the first term in the expansion of the alignment given in (41).

$$\textbf{tr}(QB) = \textbf{tr}\left(\left(\sum_{k=0}^{K-1} \tilde{S}^k \tilde{\mathbf{y}} \tilde{\mathbf{y}}^{\mathsf{T}} \tilde{S}^k\right) B\right) = \sum_{k=0}^{K-1} \textbf{tr}(Q_k B) \tag{105}$$

where $Q_k \triangleq \tilde{S}^k \tilde{\mathbf{y}} \tilde{\mathbf{y}}^{\mathsf{T}} \tilde{S}^k$. Using (104) we can write:

$$\textbf{tr}\left(Q_k B\right) = \textbf{tr}\left(Q_k \cdot \hat{\sigma}(\textbf{diag}(B_{\mathsf{lin}}))B_{\mathsf{lin}}\hat{\sigma}(\textbf{diag}(B_{\mathsf{lin}}))\right) \tag{106}$$

We note that $Q_k$ is a rank one matrix. Therefore $Q_k B$ also has rank at most one. Noting that $\hat{\sigma}(\textbf{diag}(B_{\mathsf{lin}}))$ is a diagonal matrix (with non-negative entries) and, therefore, its eigenvalues are the elements on its diagonal, calling the largest of these $\lambda_{\mathsf{max}}(\hat{\sigma}(\textbf{diag}(B_{\mathsf{lin}})))$ or $\lambda_{\mathsf{max}}$ for short and the smallest one $\lambda_{\mathsf{min}}$, we can write:

$$\begin{aligned}
\lambda_{\mathsf{min}}\textbf{tr}\left(Q_k B_{\mathsf{lin}}\right) &\leq \textbf{tr}\big(Q_k B_{\mathsf{lin}} \cdot \hat{\sigma}(\textbf{diag}(B))\big) \leq \lambda_{\mathsf{max}}\textbf{tr}\left(Q_k B_{\mathsf{lin}}\right) \\
\Rightarrow \lambda_{\mathsf{min}}\textbf{tr}\left(Q_k B_{\mathsf{lin}}\right) &\leq \textbf{tr}\big(B_{\mathsf{lin}} \cdot \hat{\sigma}(\textbf{diag}(B_{\mathsf{lin}}))Q_k\big) \\
\Rightarrow \lambda_{\mathsf{min}}^2\textbf{tr}\left(Q_k B_{\mathsf{lin}}\right) &\leq \textbf{tr}\big(\hat{\sigma}(\textbf{diag}(B_{\mathsf{lin}}))B_{\mathsf{lin}} \cdot \hat{\sigma}(\textbf{diag}(B_{\mathsf{lin}}))Q_k\big) \\
&= \textbf{tr}\left(Q_k B\right)
\end{aligned} \tag{107}$$

We recall from (35) that

$$\mathcal{A}_{\mathsf{lin}} = \textbf{tr}(QB_{\mathsf{lin}}) = \sum_{k=0}^{K-1} \textbf{tr}(Q_k B_{\mathsf{lin}}) \tag{108}$$

Using (107) and (108) we get

$$\lambda_{\mathsf{min}}^2 \mathcal{A}_{\mathsf{lin}} \leq \sum_{k=0}^{K-1} \textbf{tr}\left(Q_k B\right) = \textbf{tr}(QB) \tag{109}$$

An upper bound can be attained similarly:

$$\textbf{tr}(QB) \leq \lambda_{\mathsf{max}}^2 \mathcal{A}_{\mathsf{lin}} \tag{110}$$

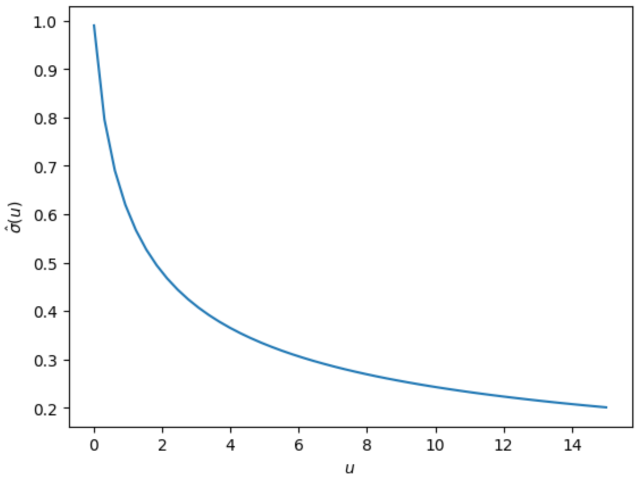

*Figure 5.* The function $\hat{\sigma}(\cdot)$ in the case where $\sigma(x) = \tanh(x)$

We can further find a lower bound for $\lambda_{\mathsf{min}}$. Note that

$$\lambda_{\mathsf{min}} = \min_a \hat{\sigma}(||\boldsymbol{z}^{(a)}||_2^2) = \min_a \hat{\sigma}(\sum_{k=0}^{K-1} (\tilde{S}^k \tilde{\mathbf{x}})_a^2) = \hat{\sigma}(\max_a \sum_{k=0}^{K-1} (\tilde{S}^k \tilde{\mathbf{x}})_a^2) \ , \tag{111}$$

where we have used the fact that $\hat{\sigma}(.)$ is a non-increasing function (see Figure 5) to establish (111).

Further, because $\hat{\sigma}(.)$ is a non-increasing function, an upper bound on $\sum_{k=0}^{K-1} (\tilde{S}^k \tilde{\mathbf{x}})_a^2$ will give us a corresponding lower bound on $\lambda_{\mathsf{min}}$. To find an upper bound on $\sum_{k=0}^{K-1} (\tilde{S}^k \tilde{\mathbf{x}})_a^2$, we provide the following analyses

$$\max_a \sum_{k=0}^{K-1} (\tilde{S}^k \tilde{\mathbf{x}})_a^2 \leq \max_{a',i} \sum_{k=0}^{K-1} (S^k \mathbf{x}_i)_{a'}^2 \tag{112}$$

$$\leq \max_i \sum_{k=0}^{K-1} ||S^k \mathbf{x}_i||_2^2 \leq \max_i \sum_{k=0}^{K-1} ||S^k||_{\mathsf{op}}^2 ||\mathbf{x}_i||_2^2 \tag{113}$$

$$\leq \sum_{k=0}^{K-1} ||S^k||_{\mathsf{op}}^2 = \sum_{k=0}^{K-1} ||S||_{\mathsf{op}}^{2k} \tag{114}$$

where in the last inequality we used the fact that for every sample $\mathbf{x}_i$ in the dataset we have $||\mathbf{x}_i||_2 \leq 1$. Therefore, we can write

$$\lambda_{\mathsf{min}}^2 = \left( \hat{\sigma}(\max_a \sum_{k=0}^{K-1} (\tilde{S}^k \tilde{\mathbf{x}})_a^2) \right)^2 \geq \left( \hat{\sigma} \left( \sum_{k=0}^{K-1} ||S||_{\mathsf{op}}^{2k} \right) \right)^2 \tag{115}$$

Considering that, in practice, bounding the norm of the GSO $S$ through normalization, (see Appendix F) ensures that the constraint $||\eta \cdot \tilde{\boldsymbol{\Theta}}||_{\mathsf{op}} < \alpha$ of our optimization problem is satisfied, we next consider the mild assumption that $||S||$ is upper bounded. Formally, this assumption is given by

$$||S||_{\mathsf{op}} \leq \nu \tag{116}$$

Using (116) and (115), we reach

$$\lambda_{\mathsf{min}}^2 \geq \rho_{\mathsf{min}} \tag{117}$$

$$\text{where } \rho_{\mathsf{min}} \triangleq \left( \hat{\sigma} \left( \sum_{k=0}^{K-1} \nu^{2k} \right) \right)^2 \tag{118}$$

Similarly for $\lambda_{\mathsf{max}}$ we can use the fact that $\hat{\sigma}(.)$ is a non-increasing function to write:

$$\lambda^2_{\mathsf{max}} = \left(\hat{\sigma}(\min_a \sum_{k=0}^{K-1} (\tilde{S}^k \tilde{\mathbf{x}})^2_a)\right)^2 \leq (\hat{\sigma}\,(0))^2 \tag{119}$$

where we can define $\rho_{\mathsf{max}} \triangleq (\hat{\sigma}\,(0))^2$. Thus, we can put (109) and (110) together to write the following:

$$\rho_{\mathsf{min}} \mathcal{A}_{\mathsf{lin}} \leq \mathbf{tr}(QB) \leq \rho_{\mathsf{max}} \mathcal{A}_{\mathsf{lin}} \tag{120}$$

which concludes the proof.

□

### B.7. Proof of Lemma 3.12

*Proof.* We start by defining the Hermite transform of the $\tanh$ functioon as $g_\ell$ for clarity in subsequent analysis and to emphasize that the $\ell$-th coefficient $\alpha_\ell$ is a function of $||\boldsymbol{z}^{(a)}||_2$.

$$g_\ell(||\boldsymbol{z}^{(a)}||_2) \triangleq \int_{-\infty}^{\infty} \tanh(||\boldsymbol{z}^{(a)}||_2 u) \cdot p_\ell(u) \cdot e^{-u^2/2} du = \alpha_i \tag{121}$$

From (40), we recall that

$$\begin{aligned}\Delta B_{ab} &= \sum_{i=1}^{\infty} \alpha_{2i+1}\beta_{2i+1} \cdot (\frac{\langle \boldsymbol{z}^{(a)}, \boldsymbol{z}^{(b)}\rangle}{||\boldsymbol{z}^{(a)}||_2 \cdot ||\boldsymbol{z}^{(b)}||_2})^{2i+1} \\ &= \sum_{i=1}^{\infty} g_{2i+1}(||\boldsymbol{z}^{(a)}||_2) \cdot g_{2i+1}(||\boldsymbol{z}^{(b)}||_2) \cdot (\frac{\langle \boldsymbol{z}^{(a)}, \boldsymbol{z}^{(b)}\rangle}{||\boldsymbol{z}^{(a)}||_2 \cdot ||\boldsymbol{z}^{(b)}||_2})^{2i+1}\end{aligned} \tag{122}$$

It can readily be verified numerically that for a given index $\ell$, we either have $g_\ell(y) \geq 0,\ \forall y \geq 0$ or $g_\ell(y) \leq 0,\ \forall y \geq 0$.[3] Consequently, we have $g_{2i+1}(||\boldsymbol{z}^{(a)}||_2) \cdot g_{2i+1}(||\boldsymbol{z}^{(b)}||_2) \geq 0$. We can further conclude that $\Delta B_{ab}$ and $B_{ab}$ have the same sign, which is given by $\mathsf{sign}(\langle \boldsymbol{z}^{(a)}, \boldsymbol{z}^{(b)}\rangle)$ since recall that:

$$B_{ab} = g_1(||\boldsymbol{z}^{(a)}||_2) g_1(||\boldsymbol{z}^{(b)}||_2) \cdot \frac{\langle \boldsymbol{z}^{(a)}, \boldsymbol{z}^{(b)}\rangle}{||\boldsymbol{z}^{(a)}||_2 \cdot ||\boldsymbol{z}^{(b)}||_2} \tag{123}$$

Next, in the scenario $\langle \boldsymbol{z}^{(a)}, \boldsymbol{z}^{(b)}\rangle \geq 0$, we have

$$\begin{aligned}&\sum_{i=1}^{\infty} g_{2i+1}(||\boldsymbol{z}^{(a)}||_2) \cdot g_{2i+1}(||\boldsymbol{z}^{(b)}||_2) \cdot (\frac{\langle \boldsymbol{z}^{(a)}, \boldsymbol{z}^{(b)}\rangle}{||\boldsymbol{z}^{(a)}||_2 \cdot ||\boldsymbol{z}^{(b)}||_2})^{2i+1} \\ &\leq \sum_{i=1}^{\infty} g_{2i+1}(||\boldsymbol{z}^{(a)}||_2) \cdot g_{2i+1}(||\boldsymbol{z}^{(b)}||_2) \cdot (\frac{\langle \boldsymbol{z}^{(a)}, \boldsymbol{z}^{(b)}\rangle}{||\boldsymbol{z}^{(a)}||_2 \cdot ||\boldsymbol{z}^{(b)}||_2}) \qquad (124) \\ &= \frac{\left(\sum_{i=1}^{\infty} g_{2i+1}(||\boldsymbol{z}^{(a)}||_2) \cdot g_{2i+1}(||\boldsymbol{z}^{(b)}||_2)\right)}{g_1(||\boldsymbol{z}^{(a)}||_2) \cdot g_1(||\boldsymbol{z}^{(b)}||_2)} \cdot B_{ab} \qquad (125)\end{aligned}$$

We established previously that $g_{2i+1}(||\boldsymbol{z}^{(a)}||_2)$ and $g_{2i+1}(||\boldsymbol{z}^{(b)}||_2)$ have the same sign for any $i \geq 0$. Further, $|\frac{g_{2i+1}(||\boldsymbol{z}^{(a)}||_2)}{g_1(||\boldsymbol{z}^{(a)}||_2)}|$ is a non-decreasing function in $||\boldsymbol{z}^{(a)}||_2$ for any $i \geq 0$ [4]. Hence, we can continue from (125), such that, we have

$$\begin{aligned}\frac{\left(\sum_{i=1}^{\infty} g_{2i+1}(||\boldsymbol{z}^{(a)}||_2) \cdot g_{2i+1}(||\boldsymbol{z}^{(b)}||_2)\right)}{g_1(||\boldsymbol{z}^{(a)}||_2) \cdot g_1(||\boldsymbol{z}^{(b)}||_2)} \cdot B_{ab} &\leq \lim_{y\to\infty} \frac{\left(\sum_{i=1}^{\infty} g_{2i+1}(y) \cdot g_{2i+1}(y)\right)}{g_1(y) \cdot g_1(y)} \cdot B_{ab} \\ &= \left(\lim_{y\to\infty} \frac{\sum_{i=1}^{\infty} (g_{2i+1}(y))^2}{(g_1(y))^2}\right) B_{ab}\end{aligned}, \tag{126}$$

[3] A simple Python script can be found in https://github.com/shervinkhal/Cross_Covariance_NTK that plots $g_\ell(y)$ against $y$ for any given index $\ell$. See the file ”numerical_verification_1.py”

[4] A simple Python script can be found in https://github.com/shervinkhal/Cross_Covariance_NTK that plots $|\frac{g_{2i+1}(y)}{g_1(y)}|$ against $y$ for any given index $i$. See the file ”numerical_verification_2.py”

which implies that

$$\Delta B_{ab} \leq \beta \cdot B_{ab} \tag{127}$$

where

$$\begin{aligned}\beta &\triangleq \lim_{y\to\infty} \frac{\sum_{i=1}^{\infty}(g_{2i+1}(y))^2}{(g_1(y))^2} \\ &= \frac{\sum_{i=1}^{\infty}\left(\int_{-\infty}^{\infty}(\lim_{y\to\infty}\tanh(y\cdot u))\cdot p_\ell(u)\cdot e^{-u^2/2}du\right)^2}{\left(\int_{-\infty}^{\infty}(\lim_{y\to\infty}\tanh(y\cdot u))\cdot p_1(u)\cdot e^{-u^2/2}du\right)^2} = \frac{\pi-2}{2} \simeq 0.57\end{aligned} \tag{128}$$

Noting that all of the inequalities from (124) and (126) hold in the opposite direction when $B_{ab} < 0$, the proof is concluded. ☐

## B.8. Proof of Theorem 3.13

*Proof.* From Lemma 3.12, we know that the first term in the expansion of the alignment i.e., $\mathbf{tr}(QB)$ is lower bounded by $\mathcal{A}_{\mathsf{lin}}$ multiplied by a constant. Hence, it remains to analyze how the second term, $\mathbf{tr}\,(Q\Delta B)$, can affect alignment. To begin with, we make the following assumption that the alignment in the linear case is sufficiently large, i.e.,

$$\mathcal{A}_{\mathsf{lin}} = \mathbf{tr}\,(QB_{\mathsf{lin}}) \geq \xi \cdot ||Q||_F||B_{\mathsf{lin}}||_F \tag{129}$$

where $0 \leq \xi \leq 1$, is some constant that quantifies how large the alignment is in the linear case. We define the matrix $W \in \mathbb{R}^{nM\times nM}$, such that, for any $(a,b)$-th entry of the matrices $B, \Delta B$, and $W$, the following holds

$$(\Delta B)_{ab} = B_{ab}W_{ab} \tag{130}$$

Recall from Lemma 3.12 that for the $(a,b)$-th entries of $B$ and $\Delta B$, we have

$$|(\Delta B)_{ab}| \leq \beta B_{ab} \quad \text{and} \quad (\Delta B)_{ab}B_{ab} \geq 0 \tag{131}$$

Therefore, the entries of $W$ must satisfy $0 \leq W_{ab} \leq \beta$.

**Analysis of term tr $(Q\Delta B)$.** Based on the discussion above, we now analyze the term $\mathbf{tr}\,(Q\Delta B)$ in the alignment.

$$\begin{aligned}\mathbf{tr}\,(Q\Delta B) &= \sum_{a,b} Q_{ab}(\Delta B)_{ab} \\ &= \sum_{a,b} Q_{ab}B_{ab}W_{ab} \\ &= \sum_{Q_{ab}B_{ab}\geq 0} Q_{ab}B_{ab}W_{ab} + \sum_{Q_{ab}B_{ab}<0} Q_{ab}B_{ab}W_{ab} \\ &\geq \beta \cdot \sum_{Q_{ab}B_{ab}<0} Q_{ab}B_{ab}\end{aligned} \tag{132}$$

To achieve the last inequality, we consider the worst case scenario, i.e., the most negative value possible for $\mathbf{tr}\,(Q\cdot(\Delta B))$. The worst case scenario corresponds to the setting when $W_{ab} = 0$ for all non-negative terms in the sum $\sum_{a,b} Q_{ab}B_{ab}W_{ab}$, and $W_{ab} = \beta$ for all the negative terms. For conciseness, we introduce the following notation:

$$\mathbf{tr}\,(QB)_+ = \sum_{Q_{ab}B_{ab}\geq 0} Q_{ab}B_{ab}, \quad \text{and} \quad \mathbf{tr}\,(QB)_- = \sum_{Q_{ab}B_{ab}<0} Q_{ab}B_{ab} \tag{133}$$

Thus, we can write

$$\mathbf{tr}\,(Q\Delta B) \geq -\beta\left|\mathbf{tr}\,(QB)_-\right| \tag{134}$$

Next, we aim to provide an upper bound on $\left|\mathbf{tr}\,(QB)_-\right|$. Recall from (104) that

$$B = \hat{\sigma}(\mathbf{diag}(B_{\mathsf{lin}}))\cdot B_{\mathsf{lin}}\cdot \hat{\sigma}(\mathbf{diag}(B_{\mathsf{lin}}))$$

Hence, since $\hat{\sigma}(\mathbf{diag}(B_{\mathsf{lin}}))$ is a diagonal matrix, it readily follows that

$$\lambda_{\mathsf{min}}^2 ||B_{\mathsf{lin}}||_F \leq ||B||_F \leq \lambda_{\mathsf{max}}^2 ||B_{\mathsf{lin}}||_F \tag{135}$$

where $\lambda_{\mathsf{max}} = \max_i(\hat{\sigma}(\mathbf{diag}(B_{\mathsf{lin}})))_{ii}$ is the largest element on the diagonal of $\hat{\sigma}(\mathbf{diag}(B_{\mathsf{lin}}))$ and therefore, also its largest eigenvalue. Similarly, $\lambda_{\mathsf{min}} = \min_i(\hat{\sigma}(\mathbf{diag}(B_{\mathsf{lin}})))_{ii}$ is the smallest element on the diagonal of $\hat{\sigma}(\mathbf{diag}(B_{\mathsf{lin}}))$ and its smallest eigenvalue. Note that all elements on the diagonal of $B_{\mathsf{lin}}$ are non-negative. From (107), we have

$$\begin{aligned} \mathbf{tr}\,(QB) &\geq \lambda_{\mathsf{min}}^2 \mathbf{tr}\,(QB_{\mathsf{lin}}) \\ &\geq \xi \lambda_{\mathsf{min}}^2 ||Q||_F ||B_{\mathsf{lin}}||_F \\ &\geq \xi \frac{\lambda_{\mathsf{min}}^2}{\lambda_{\mathsf{max}}^2} ||Q||_F ||B||_F \\ \Rightarrow \mathbf{tr}\,(QB) &= \left|\mathbf{tr}\,(Q \cdot B)_+\right| - \left|\mathbf{tr}\,(Q \cdot B)_-\right| \\ &\geq \xi \frac{\lambda_{\mathsf{min}}^2}{\lambda_{\mathsf{max}}^2} ||Q||_F ||B||_F \end{aligned} \tag{136}$$

Since changing the signs of individual elements of a matrix does not change the Frobenius norm of said matrix, we can write

$$\left|\mathbf{tr}\,(Q \cdot B)_+\right| + \left|\mathbf{tr}\,(Q \cdot B)_-\right| \leq ||Q||_F ||B||_F \tag{137}$$

From (136) and (137), we have the following

$$\left|\mathbf{tr}\,(Q \cdot B)_-\right| \leq 1/2(1 - \xi \frac{\lambda_{\mathsf{min}}^2}{\lambda_{\mathsf{max}}^2}) ||Q||_F ||B||_F \tag{138}$$

Next, recalling (134) and using (138), we have

$$\begin{aligned} \mathbf{tr}\,(Q \cdot (\Delta B)) &\geq -\beta/2(1 - \xi \frac{\lambda_{\mathsf{min}}^2}{\lambda_{\mathsf{max}}^2}) ||Q||_F ||B||_F \\ &\geq -\beta/2(\frac{\lambda_{\mathsf{max}}^2}{\xi \lambda_{\mathsf{min}}^2} - 1) \mathbf{tr}\,(QB) \end{aligned} \tag{139}$$

Using (139), we can lower bound $\mathcal{A}$ as follows

$$\begin{aligned} \mathcal{A} &= \mathbf{tr}\,(QB) + \mathbf{tr}\,(Q \cdot (\Delta B)) \\ &\geq \left(1 - \beta/2(\frac{\lambda_{\mathsf{max}}^2}{\xi \lambda_{\mathsf{min}}^2} - 1)\right) \mathbf{tr}\,(QB) \\ &\geq \lambda_{\mathsf{min}}^2 \left(1 - \beta/2(\frac{\lambda_{\mathsf{max}}^2}{\xi \lambda_{\mathsf{min}}^2} - 1)\right) \mathcal{A}_{\mathsf{lin}} \end{aligned} \tag{140}$$

Now recall from the proof of Lemma 3.11 (Equations (111) to (117)):

$$\lambda_{\mathsf{min}}^2 = \left(\hat{\sigma}(\max_a \sum_{k=0}^{K-1} (\tilde{S}^k \tilde{\mathbf{x}})_a^2)\right)^2 \geq \left(\hat{\sigma}\left(\sum_{k=0}^{K-1} \nu^{2k}\right)\right)^2 = \rho_{\mathsf{min}} \tag{141}$$

Similarly for $\lambda_{\mathsf{max}}$:

$$\lambda_{\mathsf{max}}^2 \leq (\hat{\sigma}(0))^2 = \rho_{\mathsf{max}} \tag{142}$$

Using (141) and (142), from (140) we can continue to write:

$$\mathcal{A} \geq \left(\rho_{\mathsf{min}} \left(1 + \frac{\beta}{2}\right) - \frac{\beta \rho_{\mathsf{max}}}{2\xi}\right) \mathcal{A}_{\mathsf{lin}} \tag{143}$$

Further, using the following definitions

$$c \triangleq \rho_{\mathsf{min}} \left(1 + \frac{\beta}{2}\right), \quad \text{and} \quad d \triangleq \frac{\beta \rho_{\mathsf{max}}}{2}, \tag{144}$$

we can rewrite (140) as

$$\mathcal{A} \geq (c - \frac{d}{\xi})\mathcal{A}_{\mathsf{lin}} \tag{145}$$

Thus, the proof is concluded. □

## B.9. Proof of Lemma C.2

*Proof.* Our approach is to upper bound the Rademacher complexity term in (198) for the class of hypotheses $\tilde{\mathcal{H}}_{filt}(B)$ where the vector of filter coefficients are close to some initialization. Recall the definition of $\tilde{\mathcal{H}}_{filt}(B)$ from (200):

$$\tilde{\mathcal{H}}_{filt}(B) \triangleq \left\{ \boldsymbol{f}_{\mathbf{x}}(\boldsymbol{h}) = \sum_{k=0}^{K-1} h_k S^k \mathbf{x} \,\middle|\, \boldsymbol{h} \in \mathbb{R}^K,\ ||\boldsymbol{h} - \boldsymbol{h}^{(0)}||_2 \leq B \right\}$$

We can write the complexity term from (198) as:

$$R(\ell \circ \tilde{\mathcal{H}}_{filt} \circ S) = \frac{1}{M} \mathop{\mathbb{E}}_{\boldsymbol{\sigma} \sim \{\pm 1\}^M} \left[ \sup_{h \in \tilde{\mathcal{H}}_{filt}} \sum_{i=1}^{M} \sigma_i \cdot \ell(f(\mathbf{x}_i), \mathbf{y}_i) \right] \tag{146}$$

$$= \frac{1}{M} \mathop{\mathbb{E}}_{\boldsymbol{\sigma} \sim \{\pm 1\}^M} \left[ \sup_{||\boldsymbol{h} - \boldsymbol{h}^{(0)}||_2 \leq B} \sum_{i=1}^{M} \sigma_i \cdot || \sum_{k=0}^{K-1} h_k S^k \mathbf{x}_i - \mathbf{y}_i||_2^2 \right] \tag{147}$$

Next, we provide the following lemma (an application of Lemma 26.9 from ((Shalev-Shwartz & Ben-David, 2014))).

**Lemma B.1** (Contraction lemma)**.** *Let $\phi : \mathbb{R} \to \mathbb{R}$ be a $\rho$-Lipschitz function, i.e., we have $|\phi(\alpha) - \phi(\beta)| \leq \rho|\alpha - \beta|, \forall \alpha, \beta \in \mathbb{R}$. For $\mathbf{a} \in \mathbb{R}^m$, let $\boldsymbol{\phi}(\mathbf{a})$ denote the vector $[\phi_1(a_1), \ldots, \phi_m(y_m)]$ and let $\boldsymbol{\phi} \circ A = \{\boldsymbol{\phi}(\mathbf{a}) : a \in A\}$. Then, we have*

$$R(\phi \circ \ell \circ \mathcal{H} \circ S) \leq \rho R(\ell \circ \mathcal{H} \circ S).$$

We recall the assumption that $|| \sum_{k=0}^{K-1} h_k S^k \mathbf{x}_i - \mathbf{y}_i||_2 \leq \rho$. Also note that the function $\phi(z) = z^2$ is $\rho$-Lipschitz continuous over the domain $|z| \leq \rho$, therefore using Lemma B.1 and (147) we can write:

$$R(\ell \circ \tilde{\mathcal{H}}_{filt} \circ S) \leq \rho \cdot \frac{1}{M} \mathop{\mathbb{E}}_{\boldsymbol{\sigma} \sim \{\pm 1\}^M} \left[ \sup_{||\boldsymbol{h} - \boldsymbol{h}^{(0)}||_2 \leq B} \sum_{i=1}^{M} \sigma_i \cdot || \sum_{k=0}^{K-1} h_k S^k \mathbf{x}_i - \mathbf{y}_i||_2 \right] \tag{148}$$

Next, we re-state Corollary 4 from (Maurer, 2016) that enables us to bound the Rademacher complexity for our setting when the hypothesis functions are vector valued.

**Lemma B.2.** *For a given set $\mathcal{X} = (x_1, \ldots, x_n) \in \mathcal{X}^n$, a class of fucntions $\mathcal{F}$, such that, $f : \mathcal{X} \to \ell_2$ and an L-Lispschitz function $g_i : \ell_2 \to \mathbb{R}$, we have*

$$\mathbb{E}\left[\sup_{f \in \mathcal{F}} \sum_i \sigma_i g_i(f(x_i))\right] \leq \sqrt{2} L \mathbb{E}\left[\sup_{f \in \mathcal{F}} \sum_{i,j} \sigma_{ij} f_j(x_i)\right],$$

*where $\sigma_{ij}$ is an independent doubly indexed Rademacher sequence and $f_j(x_i)$ is the $j$-th component of $f(x_i)$.*

The above lemma still holds if instead of $f : \mathcal{X} \to \ell_2$ we have $f : \mathcal{X} \to \mathcal{B}^n(\rho) \subset \mathbb{R}^n$ where $\mathcal{B}^n(\rho)$ is an $\ell_2$ norm ball in $\mathbb{R}^n$ of radius $\rho$ centered at the origin.

In our case, we can take $\mathcal{X} = \mathbb{R} \times \mathbb{R}$. Note that $\{(\mathbf{x}_i, \mathbf{y}_i)\}_{i=1}^M \in \mathcal{X}^M = (\mathbb{R} \times \mathbb{R})^M$ and also $g(\boldsymbol{z}) = ||\boldsymbol{z}||_2$ which is $L$-Lipschitz with $L = 1$. Now we can apply Lemma B.2 to upper bound (148):

$$M/\rho \cdot R(\ell \circ \tilde{\mathcal{H}}_{filt} \circ S) \leq \sqrt{2}\mathbb{E}\left[\sup_{||\boldsymbol{h}-\boldsymbol{h}^{(0)}||_2 \leq B} \sum_{i=1}^M \sum_{j=1}^n \sigma_{ij} \cdot (\sum_{k=0}^{K-1} h_k S^k \mathbf{x}_i - \mathbf{y}_i)\right] \tag{149}$$

$$= \sqrt{2} \mathop{\mathbb{E}}_{\boldsymbol{\sigma}_i \sim \{\pm 1\}^n}\left[\sup_{||\boldsymbol{h}-\boldsymbol{h}^{(0)}||_2 \leq B} \sum_{i=1}^M \langle \boldsymbol{\sigma}_i, \sum_{k=0}^{K-1} h_k S^k \mathbf{x}_i - \mathbf{y}_i\rangle\right] \tag{150}$$

Writing $\boldsymbol{h} = \boldsymbol{h}^{(0)} + \Delta\boldsymbol{h}$, we have

$$M/\rho \cdot R(\ell \circ \tilde{\mathcal{H}}_{filt} \circ S) \leq \sqrt{2} \mathop{\mathbb{E}}_{\boldsymbol{\sigma}_i \sim \{\pm 1\}^n}\left[\sup_{||\Delta\boldsymbol{h}||_2 \leq B} \sum_{i=1}^M \langle \boldsymbol{\sigma}_i, \sum_{k=0}^{K-1} (h_k^{(0)} + \Delta h_k) S^k \mathbf{x}_i - \mathbf{y}_i\rangle\right] \tag{151}$$

$$\leq \sqrt{2} \mathop{\mathbb{E}}_{\boldsymbol{\sigma}_i \sim \{\pm 1\}^n}\left[\sup_{||\Delta\boldsymbol{h}||_2 \leq B} \sum_{i=1}^M \langle \boldsymbol{\sigma}_i, \sum_{k=0}^{K-1} h_k^{(0)} S^k \mathbf{x}_i - \mathbf{y}_i\rangle\right]$$
$$+ \sqrt{2} \mathop{\mathbb{E}}_{\boldsymbol{\sigma}_i \sim \{\pm 1\}^n}\left[\sup_{||\Delta\boldsymbol{h}||_2 \leq B} \sum_{i=1}^M \langle \boldsymbol{\sigma}_i, \sum_{k=0}^{K-1} \Delta h_k S^k \mathbf{x}_i\rangle\right] \tag{152}$$

In (152), the first term does not depend on $\Delta\boldsymbol{h}$ and hence, we can remove the supremum, i.e.,

$$\mathop{\mathbb{E}}_{\boldsymbol{\sigma}_i \sim \{\pm 1\}^n}\left[\sup_{||\Delta\boldsymbol{h}||_2 \leq B} \sum_{i=1}^M \langle \boldsymbol{\sigma}_i, \sum_{k=0}^{K-1} h_k^{(0)} S^k \mathbf{x}_i - \mathbf{y}_i\rangle\right] = \mathop{\mathbb{E}}_{\boldsymbol{\sigma}_i \sim \{\pm 1\}^n}\left[\sum_{i=1}^M \langle \boldsymbol{\sigma}_i, \sum_{k=0}^{K-1} h_k^{(0)} S^k \mathbf{x}_i - \mathbf{y}_i\rangle\right] \tag{153}$$

Further, using the linearity of expectations and inner products, we have

$$\sum_{i=1}^M \sum_{k=0}^{K-1} \mathop{\mathbb{E}}_{\boldsymbol{\sigma}_i \sim \{\pm 1\}^n}\left[\langle \boldsymbol{\sigma}_i, h_k^{(0)} S^k \mathbf{x}_i - \mathbf{y}_i\rangle\right] = \sum_{i=1}^M \sum_{k=0}^{K-1} \sum_{j=1}^n (h_k^{(0)} S^k \mathbf{x}_i - \mathbf{y}_i)_j \mathop{\mathbb{E}}_{\boldsymbol{\sigma}_i \sim \{\pm 1\}^n}[(\boldsymbol{\sigma}_i)_j] = 0 \tag{154}$$

Thus, we can restate (152) as

$$M/\rho \cdot R(\ell \circ \tilde{\mathcal{H}}_{filt} \circ S) \leq \sqrt{2} \mathop{\mathbb{E}}_{\boldsymbol{\sigma}_i \sim \{\pm 1\}^n}\left[\sup_{||\Delta\boldsymbol{h}||_2 \leq B} \sum_{i=1}^M \langle \boldsymbol{\sigma}_i, \sum_{k=0}^{K-1} \Delta h_k S^k \mathbf{x}_i\rangle\right] \tag{155}$$

Focusing on the supremum in (155), we have

$$\sup_{||\Delta\boldsymbol{h}||_2 \leq B} \sum_{i=1}^M \langle \boldsymbol{\sigma}_i, \sum_{k=0}^{K-1} \Delta h_k S^k \mathbf{x}_i\rangle = \sup_{||\Delta\boldsymbol{h}||_2 \leq B} \sum_{i=1}^M \sum_{k=0}^{K-1} \langle \boldsymbol{\sigma}_i, \Delta h_k S^k \mathbf{x}_i\rangle \tag{156}$$

$$= \sup_{||\Delta\boldsymbol{h}||_2 \leq B} \sum_{k=0}^{K-1} \Delta h_k \left(\sum_{i=1}^M \langle \boldsymbol{\sigma}_i, S^k \mathbf{x}_i\rangle\right) \tag{157}$$

We introduce the notation $a_k \triangleq \sum_{i=1}^M \langle \boldsymbol{\sigma}_i, S^k \mathbf{x}_i\rangle$. Note that $a_k$ doesn't depend on $\Delta\boldsymbol{h}$. Hence,

$$\sup_{||\Delta\boldsymbol{h}||_2 \leq B} \sum_{k=0}^{K-1} \Delta h_k \left(\sum_{i=1}^M \langle \boldsymbol{\sigma}_i, S^k \mathbf{x}_i\rangle\right) = \sup_{||\Delta\boldsymbol{h}||_2 \leq B} \sum_{k=0}^{K-1} \Delta h_k a_k = \sup_{||\Delta\boldsymbol{h}||_2 \leq B} \langle \Delta\boldsymbol{h}, \boldsymbol{a}\rangle = B \cdot ||\boldsymbol{a}||_2 \tag{158}$$

Inserting (158) into (155), we have

$$M/\rho \cdot R(\ell \circ \tilde{\mathcal{H}}_{filt} \circ S) \leq \sqrt{2} \mathop{\mathbb{E}}_{\boldsymbol{\sigma}_i \sim \{\pm 1\}^n}[B \cdot ||\boldsymbol{a}||_2] = \sqrt{2}B \mathop{\mathbb{E}}_{\boldsymbol{\sigma}_i \sim \{\pm 1\}^n}\left[\sqrt{\sum_{k=0}^{K-1}\left(\sum_{i=1}^M \langle \boldsymbol{\sigma}_i, S^k \mathbf{x}_i\rangle\right)^2}\right] \tag{159}$$

Further, using Jensen's inequality in (159), we get

$$M/\rho \cdot R(\ell \circ \tilde{\mathcal{H}}_{filt} \circ S) \leq \sqrt{2}B \sqrt{\sum_{k=0}^{K-1} \mathop{\mathbb{E}}_{\boldsymbol{\sigma}_i \sim \{\pm 1\}^n} \left[ \left( \sum_{i=1}^{M} \langle \boldsymbol{\sigma}_i, S^k \mathbf{x}_i \rangle \right)^2 \right]} \tag{160}$$

$$= \sqrt{2}B \sqrt{\sum_{k=0}^{K-1} \mathop{\mathbb{E}}_{\boldsymbol{\sigma}_i \sim \{\pm 1\}^n} \left[ \left( \sum_{i=1}^{M} \sum_{j=1}^{n} (\boldsymbol{\sigma}_i)_j (S^k \mathbf{x}_i)_j \right)^2 \right]} \tag{161}$$

$$= \sqrt{2}B \sqrt{\sum_{k=0}^{K-1} \mathop{\mathbb{E}}_{\boldsymbol{\sigma}_i \sim \{\pm 1\}^n} \left[ \sum_{i=1}^{M} \sum_{j=1}^{n} \left((\boldsymbol{\sigma}_i)_j\right)^2 \left((S^k \mathbf{x}_i)_j\right)^2 \right]} \tag{162}$$

$$= \sqrt{2}B \sqrt{\sum_{k=0}^{K-1} \sum_{i=1}^{M} \sum_{j=1}^{n} \left((S^k \mathbf{x}_i)_j\right)^2} \tag{163}$$

$$= \sqrt{2}B \sqrt{\sum_{i=1}^{M} \sum_{k=0}^{K-1} ||S^k \mathbf{x}_i||_2^2} \tag{164}$$

In the above set of equations from (162) to (163), we have used the fact that $(\boldsymbol{\sigma}_i)_j$ are independent and therefore:

$$\mathbb{E}\left[(\boldsymbol{\sigma}_i)_j (\boldsymbol{\sigma}_k)_\ell\right] = \begin{cases} 1 & \text{if } i = k,\ j = l \\ 0 & o.w. \end{cases} \tag{165}$$

Finally, we provide an upper bound on the Rademacher complexity that is proportional to $1/\sqrt{M}$. From 164:

$$M/\rho \cdot R(\ell \circ \tilde{\mathcal{H}}_{filt} \circ S) \leq \sqrt{2}B \sqrt{\sum_{i=1}^{M} \sum_{k=0}^{K-1} ||S^k \mathbf{x}_i||_2^2} \leq \sqrt{2}B \sqrt{MK \max_{k,i} ||S^k \mathbf{x}_i||_2^2} \tag{166}$$

$$\Rightarrow R(\ell \circ \tilde{\mathcal{H}}_{filt} \circ S) \leq B\rho \sqrt{\frac{2K \max_{k,i} ||S^k \mathbf{x}_i||_2^2}{M}} \tag{167}$$

We thus conclude the proof. □

## B.10. Proof of Lemma C.3

*Proof.* Our focus is on the setting where the NTK does not change during training. In such a case, the "movement" of the parameters (i.e., how much the vector of parameters changes) during gradient descent is directly related to the NTK.

Recall that the NTK matrix $\tilde{\boldsymbol{\Theta}}(\boldsymbol{h}) \in \mathbb{R}^{nM \times nM}$ consists of $M^2$ blocks, each of which is an $n \times n$ matrix $\Theta(\mathbf{x}_i, \mathbf{x}_j) = \mathrm{J}_{\boldsymbol{f}_{\mathbf{x}_i}}(\boldsymbol{h}^{(t)}) \big(\mathrm{J}_{\boldsymbol{f}_{\mathbf{x}_j}}(\boldsymbol{h}^{(t)})\big)^{\mathsf{T}}$ (see (7)). Hence, assuming that the NTK does not change during training is equivalent to assuming that the Jacobian matrices $\mathrm{J}_{\boldsymbol{f}_{\mathbf{x}_i}}(\boldsymbol{h}^{(t)})$ are constant. Also, for ease of notation, we define the big Jacobian matrix $\tilde{\mathbf{J}} \in \mathbb{R}^{nM \times p}$ that consists of all the Jacobian matrices $\mathrm{J}_{\boldsymbol{f}_{\mathbf{x}_i}}$ stacked on top of one another. Therefore, we have

$$\tilde{\boldsymbol{\Theta}}(\boldsymbol{h}) = (\tilde{\mathbf{J}}(\boldsymbol{h}))(\tilde{\mathbf{J}}(\boldsymbol{h}))^{\mathsf{T}} \tag{168}$$

Again, we note that in general both $\tilde{\mathbf{J}}$ (and consequently, $\tilde{\boldsymbol{\Theta}}$) can depend on the parameters $\boldsymbol{h}$ but we are considering cases where they do not.[5]

Similar to Section 2, we denote the vector of all parameters of the predictor as $\boldsymbol{h} \in \mathbb{R}^p$. For the $t$-th step of gradient descent we can write:

$$\boldsymbol{h}^{(t+1)} = \boldsymbol{h}^{(t)} - \eta \cdot \nabla\Phi(\boldsymbol{h}^{(t)}) \tag{169}$$

[5]This is the case for any linear predictor like the graph filter as we saw in Section 3 and it is also the case for some neural networks with infinite width in every layer. See Appendix D and (Liu et al., 2020) for details.

Also, we can write the gradient in terms of the Jacobian evaluated at different input points as follows

$$\nabla\Phi(\boldsymbol{h}^{(t)}) = \sum_{j=1}^{M} \left(\mathrm{J}_{\boldsymbol{f}_{\mathbf{x}_j}}\right)^{\mathsf{T}} \cdot (\boldsymbol{f}_{\mathbf{x}_j}(\boldsymbol{h}^{(t)}) - \mathbf{y}_j) \tag{170}$$

Further, using the linearization of $\boldsymbol{f}_{\mathbf{x}_j}$ around the initialization $\boldsymbol{h}^{(0)}$, we have

$$\boldsymbol{f}_{\mathbf{x}_j}(\boldsymbol{h}^{(t)}) - \mathbf{y}_j = \boldsymbol{f}_{\mathbf{x}_j}(\boldsymbol{h}^{(0)}) + \mathrm{J}_{\boldsymbol{f}_{\mathbf{x}_j}} \cdot (\boldsymbol{h}^{(t)} - \boldsymbol{h}^{(0)}) - \mathbf{y}_j \tag{171}$$

Since $\mathrm{J}_{\boldsymbol{f}_{\mathbf{x}_j}}$ is assumed to be constant, we can further replace $\boldsymbol{f}_{\mathbf{x}_j}(\boldsymbol{h}^{(0)})$ with a linearization around $\boldsymbol{h} = 0$, such that, we have

$$\boldsymbol{f}_{\mathbf{x}_j}(\boldsymbol{h}^{(0)}) = \boldsymbol{f}_{\mathbf{x}_j}(0) + \mathrm{J}_{\boldsymbol{f}_{\mathbf{x}_j}}\boldsymbol{h}^{(0)} = \mathrm{J}_{\boldsymbol{f}_{\mathbf{x}_j}}\boldsymbol{h}^{(0)} \tag{172}$$

In (172), we used the fact that the output of the predictor is zero when all its parameters are set to zero. By inserting (172) into (171), we get

$$\boldsymbol{f}_{\mathbf{x}_j}(\boldsymbol{h}^{(t)}) - \mathbf{y}_j = \mathrm{J}_{\boldsymbol{f}_{\mathbf{x}_j}}\boldsymbol{h}^{(t)} - \mathbf{y}_j \tag{173}$$

And inserting (173) into (170), we have

$$\nabla\Phi(\boldsymbol{h}^{(t)}) = \sum_{j=1}^{M} \left(\mathrm{J}_{\boldsymbol{f}_{\mathbf{x}_j}}\right)^{\mathsf{T}} \cdot (\mathrm{J}_{\boldsymbol{f}_{\mathbf{x}_j}}\boldsymbol{h}^{(t)} - \mathbf{y}_j) \tag{174}$$

Replacing the gradient of the loss $\nabla\Phi(\boldsymbol{h}^{(t)})$ in (169) by (174) leads to

$$\boldsymbol{h}^{(t+1)} = \boldsymbol{h}^{(t)} - \eta \cdot \sum_{j=1}^{M} \left(\mathrm{J}_{\boldsymbol{f}_{\mathbf{x}_j}}\right)^{\mathsf{T}} \cdot (\mathrm{J}_{\boldsymbol{f}_{\mathbf{x}_j}}\boldsymbol{h}^{(t)} - \mathbf{y}_j)\ , \tag{175}$$

which implies

$$\mathrm{J}_{\boldsymbol{f}_{\mathbf{x}_i}}\boldsymbol{h}^{(t+1)} = \mathrm{J}_{\boldsymbol{f}_{\mathbf{x}_i}}\boldsymbol{h}^{(t)} - \eta \cdot \sum_{j=1}^{M} \mathrm{J}_{\boldsymbol{f}_{\mathbf{x}_i}}\left(\mathrm{J}_{\boldsymbol{f}_{\mathbf{x}_j}}\right)^{\mathsf{T}} \cdot (\mathrm{J}_{\boldsymbol{f}_{\mathbf{x}_j}}\boldsymbol{h}^{(t)} - \mathbf{y}_j) \tag{176}$$

Introducing the notation $\boldsymbol{r}_i^{(t)}$ to denote $\mathrm{J}_{\boldsymbol{f}_{\mathbf{x}_i}}\boldsymbol{h}^{(t)}$, we can rewrite (176) as

$$\boldsymbol{r}_i^{(t+1)} = \boldsymbol{r}_i^{(t)} - \eta \cdot \sum_{j=1}^{M} \Theta(\mathbf{x}_i, \mathbf{x}_j) \cdot (\boldsymbol{r}_j^{(t)} - \mathbf{y}_j) \tag{177}$$

Similar to the procedure in (5), we can stack all the vectors $\boldsymbol{r}_i^{(t)}$ together in one tall vector $\tilde{\boldsymbol{r}}(t) \in \mathbb{R}^{nM\times 1}$ and rewrite (177) in the vectorized form as follows

$$\tilde{\boldsymbol{r}}(t+1) = \tilde{\boldsymbol{r}}(t) - \eta \cdot \tilde{\boldsymbol{\Theta}}(\tilde{\boldsymbol{r}}(t) - \tilde{\mathbf{y}}) \tag{178}$$

$$\Rightarrow \tilde{\boldsymbol{r}}(t+1) - \tilde{\mathbf{y}} = \tilde{\boldsymbol{r}}(t) - \tilde{\mathbf{y}} - \eta \cdot \tilde{\boldsymbol{\Theta}}(\tilde{\boldsymbol{r}}(t) - \tilde{\mathbf{y}}) \tag{179}$$

$$\Rightarrow \tilde{\boldsymbol{r}}(t) - \tilde{\mathbf{y}} = (I - \eta \cdot \tilde{\boldsymbol{\Theta}})^t(\tilde{\boldsymbol{r}}(0) - \tilde{\mathbf{y}}) \tag{180}$$

Now, writing (175) in terms of the big Jacobian matrix $\tilde{\mathbf{J}}$

$$\boldsymbol{h}^{(t+1)} = \boldsymbol{h}^{(t)} - \eta \cdot \tilde{\mathbf{J}}^{\mathsf{T}}(\tilde{\boldsymbol{r}}(t) - \tilde{\mathbf{y}}) \tag{181}$$

and replacing $(\tilde{\boldsymbol{r}}(t) - \tilde{\mathbf{y}})$ by the quantity from (180) we get

$$\Rightarrow \boldsymbol{h}^{(t+1)} = \boldsymbol{h}^{(t)} + \eta \cdot \tilde{\mathbf{J}}^{\mathsf{T}}(I - \eta \cdot \tilde{\boldsymbol{\Theta}})^t\tilde{\mathbf{y}} - \eta \cdot \tilde{\mathbf{J}}^{\mathsf{T}}(I - \eta \cdot \tilde{\boldsymbol{\Theta}})^t\tilde{\boldsymbol{r}}(0) \tag{182}$$

$$\Rightarrow \boldsymbol{h}^{(\infty)} - \boldsymbol{h}^{(0)} = \eta \sum_{t=0}^{\infty} \tilde{\mathbf{J}}^{\mathsf{T}}(I - \eta \cdot \tilde{\boldsymbol{\Theta}})^t\tilde{\mathbf{y}} - \eta \sum_{t=0}^{\infty} \tilde{\mathbf{J}}^{\mathsf{T}}(I - \eta \cdot \tilde{\boldsymbol{\Theta}})^t\tilde{\boldsymbol{r}}(0) \tag{183}$$

We write the eigen-decomposition of $\tilde{\mathbf{\Theta}}$ (assuming it has rank $r$) as

$$\tilde{\mathbf{\Theta}} = \sum_{\ell=1}^{r} \lambda_\ell \boldsymbol{v}_\ell \boldsymbol{v}_\ell^\mathsf{T}$$

which implies the following eigen-decomposition for $(I - \eta \cdot \tilde{\mathbf{\Theta}})$.

$$I - \eta \cdot \tilde{\mathbf{\Theta}} \quad = \quad \sum_{\ell=1}^{r} (1 - \eta\lambda_\ell) \boldsymbol{v}_\ell \boldsymbol{v}_\ell^\mathsf{T} + \sum_{\ell=r+1}^{nM} 1 \cdot \boldsymbol{v}_\ell \boldsymbol{v}_\ell^\mathsf{T} \tag{184}$$

Noting that $\lambda_\ell = 0$ for $\ell > r$, we use the eigen-decomposition in (184) to write

$$\Rightarrow \boldsymbol{h}^{(\infty)} - \boldsymbol{h}^{(0)} = \eta \sum_{t=0}^{\infty} \sum_{\ell=1}^{nM} \tilde{\mathbf{J}}^\mathsf{T} (1 - \eta\lambda_\ell)^t \boldsymbol{v}_\ell \boldsymbol{v}_\ell^\mathsf{T} \tilde{\mathbf{y}} - \eta \sum_{t=0}^{\infty} \sum_{\ell=1}^{nM} \tilde{\mathbf{J}}^\mathsf{T} (1 - \eta\lambda_\ell)^t \boldsymbol{v}_\ell \boldsymbol{v}_\ell^\mathsf{T} \tilde{\boldsymbol{r}}(0) \tag{185}$$

Note that

$$\text{for } j > r, \ \tilde{\mathbf{\Theta}} \boldsymbol{v}_j = \sum_{\ell=1}^{r} \lambda_\ell \boldsymbol{v}_\ell \boldsymbol{v}_\ell^\mathsf{T} \boldsymbol{v}_j = 0 \,. \tag{186}$$

Hence, from (168) and (186), we have for $j > r$:

$$\tilde{\mathbf{J}} \cdot \tilde{\mathbf{J}}^\mathsf{T} \boldsymbol{v}_j = 0 \tag{187}$$

Assuming that $\tilde{\mathbf{J}} \in \mathbb{R}^{nM \times p}$ is full-column rank, (187) implies that

$$\text{for } j > r, \ \tilde{\mathbf{J}}^\mathsf{T} \boldsymbol{v}_j = 0 \tag{188}$$

Hence, we can write (185) as

$$\begin{aligned}
\boldsymbol{h}^{(\infty)} - \boldsymbol{h}^{(0)} &= \eta \sum_{t=0}^{\infty} \sum_{\ell=1}^{r} \tilde{\mathbf{J}}^\mathsf{T} (1 - \eta\lambda_\ell)^t \boldsymbol{v}_\ell \boldsymbol{v}_\ell^\mathsf{T} \tilde{\mathbf{y}} - \eta \sum_{t=0}^{\infty} \sum_{\ell=1}^{r} \tilde{\mathbf{J}}^\mathsf{T} (1 - \eta\lambda_\ell)^t \boldsymbol{v}_\ell \boldsymbol{v}_\ell^\mathsf{T} \tilde{\boldsymbol{r}}(0) && (189) \\
&= \eta \sum_{\ell=1}^{r} \tilde{\mathbf{J}}^\mathsf{T} \frac{1}{\eta\lambda_\ell} \boldsymbol{v}_\ell \boldsymbol{v}_\ell^\mathsf{T} \tilde{\mathbf{y}} - \eta \sum_{\ell=1}^{r} \tilde{\mathbf{J}}^\mathsf{T} \frac{1}{\eta\lambda_\ell} \boldsymbol{v}_\ell \boldsymbol{v}_\ell^\mathsf{T} \tilde{\boldsymbol{r}}(0) && (190) \\
&= \tilde{\mathbf{J}}^\mathsf{T} \tilde{\mathbf{\Theta}}^\dagger \tilde{\mathbf{y}} - \tilde{\mathbf{J}}^\mathsf{T} \tilde{\mathbf{\Theta}}^\dagger \tilde{\boldsymbol{r}}(0) && (191)
\end{aligned}$$

Now, similar to what we saw in the proof of Theorem 2.1 ((53) - (56)), if we choose the parameter controlling the magnitude of initialization to be $\kappa = \mathcal{O}(\varepsilon\sqrt{\frac{\delta}{nM}})$, then with probability at least $1 - \delta$ we have $\tilde{\boldsymbol{r}}(0) = \mathcal{O}\left(\varepsilon\sqrt{\frac{\delta}{nM}}\right)$ and $||\tilde{\boldsymbol{r}}(0)||_2 = \mathcal{O}(\varepsilon)$.

$$\begin{aligned}
||\boldsymbol{h}^{(\infty)} - \boldsymbol{h}^{(0)}||_2 &= \sqrt{\tilde{\mathbf{y}}^\mathsf{T} \tilde{\mathbf{\Theta}}^\dagger \tilde{\mathbf{J}} \cdot \tilde{\mathbf{J}}^\mathsf{T} \tilde{\mathbf{\Theta}}^\dagger \tilde{\mathbf{y}}} \pm \mathcal{O}(\varepsilon) && (192) \\
&= \sqrt{\tilde{\mathbf{y}}^\mathsf{T} \tilde{\mathbf{\Theta}}^\dagger \tilde{\mathbf{\Theta}} \tilde{\mathbf{\Theta}}^\dagger \tilde{\mathbf{y}}} \pm \mathcal{O}(\varepsilon) && (193)
\end{aligned}$$

Finally, since $\tilde{\mathbf{\Theta}}^\dagger$ acts as a weak inverse, we get

$$||\boldsymbol{h}^{(\infty)} - \boldsymbol{h}^{(0)}||_2 = \sqrt{\tilde{\mathbf{y}}^\mathsf{T} \tilde{\mathbf{\Theta}}^\dagger \tilde{\mathbf{y}}} \pm \mathcal{O}(\varepsilon) \tag{194}$$

Thus, we've concluded the proof by showing that the "movement" of the parameters, $||\boldsymbol{h}^{(\infty)} - \boldsymbol{h}^{(0)}||_2$, is directly related to the NTK. (More precisely, the pseudo-inverse of the NTK $\tilde{\mathbf{\Theta}}^\dagger$) $\square$

## C. Alignment, The NTK and Generalization

In this section, we will briefly go over how alignment relates to generalization. We start by providing a few definitions from (Shalev-Shwartz & Ben-David, 2014). Consider a function class $\mathcal{F}$ and a function $f \in \mathcal{F}$ and a distribution $\mathcal{D}$ from which we sample data points $z$. Also consider a set $\mathcal{S} = \{z_1, z_2, \cdots, z_M\}$ of M samples, sampled i.i.d from $\mathcal{D}$. The population average $L_{\mathcal{D}}(f)$ and sample average $L_{\mathcal{S}}(f)$ of the function $f$ are then defined as follows:

$$L_{\mathcal{D}}(f) \triangleq \mathbb{E}_{z\sim\mathcal{D}}[f(z)], \quad L_{\mathcal{S}}(f) \triangleq \frac{1}{M}\sum_{i=1}^{M} f(z_i) \tag{195}$$

Also, the Rademacher complexity of class $\mathcal{F}$ with respect to $\mathcal{S}$ is defined as:

$$R(\mathcal{F}\circ\mathcal{S}) \triangleq \frac{1}{M}\underset{\boldsymbol{\sigma}\sim\{\pm1\}^M}{\mathbb{E}}\left[\sup_{f\in\mathcal{F}}\sum_{i=1}^{M}\sigma_i f\left(z_i\right)\right] \tag{196}$$

where each element of the random vector $\boldsymbol{\sigma}$ is either 1 or -1 with equal probability.

Now consider class of functions (called hypotheses here) $\mathcal{H}$ and some loss function $\ell(h, z)$. In an empirical risk minimization problem, our goal is to find the function $h^* \in \mathcal{H}$ that minimizes the sample loss $L_{\mathcal{S}}(\ell(h))$:

$$h^* = \mathrm{ERM}_{\mathcal{H}}(\mathcal{S}) = \underset{h\in\mathcal{H}}{\arg\min}\, L_{\mathcal{S}}(\ell(h)) = \underset{h\in\mathcal{H}}{\arg\min}\, \frac{1}{M}\sum_{i=1}^{M}\ell(h, z_i) \tag{197}$$

But minimizing the sample loss does not necessarily lead to a small population loss $L_{\mathcal{D}}(\ell(h)) = \mathbb{E}_{z\sim\mathcal{D}}[\ell(z,h)]$. The gap between these two losses is called the generalization error. We present the following lemma which upper bounds the generalization error for a class of functions $\mathcal{H}$ based on the Rademacher complexity of the class:

**Lemma C.1** (Theorem 26.5 from (Shalev-Shwartz & Ben-David, 2014))**.** *Assume that for all $z$ and $h \in \mathcal{H}$ we have that $|\ell(h, z)| \leq c$. Then with probability of at least $1-\delta$, for all $h \in \mathcal{H}$,*

$$L_{\mathcal{D}}(\ell(h)) - L_{\mathcal{S}}(\ell(h)) \leq 2R(\ell\circ\mathcal{H}\circ\mathcal{S}) + 4c\sqrt{\frac{2\ln(4/\delta)}{M}} \tag{198}$$

*where $\ell(h, z)$ is some loss function. In particular, this holds for $h = \mathrm{ERM}_{\mathcal{H}}(\mathcal{S})$ which is the solution of the empirical risk minimization problem.*

In the case of the multivariate regression problem that we consider in this paper, each point $z$ is an input output pair of vectors $(\mathbf{x}_i, \mathbf{y}_i)$ and the loss function is quadratic. Also the set $\mathcal{H}$ in our case corresponds to the set of all possible predictors or the set of possible parameter vectors $\boldsymbol{h} \in \mathbb{R}^p$ and the set $\mathcal{S}$ is our training set.

From Lemma C.1, we can surmise that if the complexity of the function class $\ell\circ\mathcal{H}$ is sufficiently small, our trained model generalizes to unseen input output pairs sampled from the same distribution as the training set. Henceforth in this section we will only be considering the hypothesis class of graph filters with $K$ filter taps:

$$\mathcal{H}_{filt} \triangleq \left\{\boldsymbol{f}_{\mathbf{x}}(\boldsymbol{h}) = \sum_{k=0}^{K-1} h_k S^k \mathbf{x} \,\middle|\, \boldsymbol{h}\in\mathbb{R}^K\right\} \tag{199}$$

First, in the next lemma, we will be considering the subset $\tilde{\mathcal{H}}_{filt} \subset \mathcal{H}_{filt}$, for which the vector of filter coefficients is close to some initialization $\boldsymbol{h}^{(0)}$. Formally:

$$\tilde{\mathcal{H}}_{filt}(B) \triangleq \left\{\boldsymbol{f}_{\mathbf{x}}(\boldsymbol{h}) = \sum_{k=0}^{K-1} h_k S^k \mathbf{x} \,\middle|\, \boldsymbol{h}\in\mathbb{R}^K,\ ||\boldsymbol{h}-\boldsymbol{h}^{(0)}||_2 \leq B\right\} \tag{200}$$

The following lemma gives us an upper bound for the complexity of $\tilde{\mathcal{H}}_{filt}$:

**Lemma C.2.** *Consider the class of hypotheses $\tilde{\mathcal{H}}_{filt}(B)$ defined in (200). Assuming that $||\sum_{k=0}^{K-1} h_k S^k \mathbf{x}_i - \mathbf{y}_i||_2 \leq \rho$, $\forall(\mathbf{x}_i, \mathbf{y}_i) \in S, \boldsymbol{h} \in \tilde{\mathcal{H}}_{filt}$, the Rademacher complexity of $\tilde{\mathcal{H}}_{filt}$ can be upper bounded as follows:*

$$R(\ell \circ \tilde{\mathcal{H}}_{filt} \circ \mathcal{S}) \leq B\rho\sqrt{\frac{2K \max_{k,i} ||S^k \mathbf{x}_i||_2^2}{M}} \tag{201}$$

*where the loss function is quadratic $\ell(\boldsymbol{h}, z = (\mathbf{x}_i, \mathbf{y}_i)) = ||\sum_{k=0}^{K-1} h_k S^k \mathbf{x}_i - \mathbf{y}_i||_2^2$.*

For proof of Lemma C.2 see Section B.9. In order to meaningfully utilize Lemma C.2, we next bound the movement of the vector of parameters (in this case the filter coefficients) from initialization using a straightforward extension of a result from (Arora et al., 2019).

**Lemma C.3.** *Consider the prediction task defined in Section 2. If the NTK $\tilde{\mathbf{\Theta}}(\boldsymbol{h}^{(t)})$ is constant during training and $\kappa = \mathcal{O}(\varepsilon\sqrt{\frac{\delta_1}{nM}})$, then with probability at least $1 - \delta_1$, The change in the vector of parameters, $\boldsymbol{h}$, after infinitely many steps of gradient descent is related to the NTK matrix, $\tilde{\mathbf{\Theta}}$, as follows:*

$$||\boldsymbol{h}^{(\infty)} - \boldsymbol{h}^{(0)}||_2^2 = \sqrt{\tilde{\mathbf{y}}^\mathsf{T} \tilde{\mathbf{\Theta}}^\dagger \tilde{\mathbf{y}}} \pm \mathcal{O}(\varepsilon)\ ^{6} \tag{202}$$

For proof of Lemma C.3 see Section B.10. Motivated by the above lemma we define the class of functions $\mathcal{H}_{trained}$ which includes the family of graph filters where the coefficients have been initialized randomly to some vector $\boldsymbol{h}^{(0)}$ and subsequently updated using an arbitrary number of gradient descent steps:

$$\mathcal{H}_{trained} \triangleq \left\{ \boldsymbol{f}_\mathbf{x}(\boldsymbol{h}) = \sum_{k=0}^{K-1} h_k S^k \mathbf{x} \;\middle|\; \begin{array}{c} \boldsymbol{h} \in \mathbb{R}^K \text{initialized to } \boldsymbol{h}^{(0)} \text{ with } \kappa = \mathcal{O}\left(\varepsilon\sqrt{\frac{\delta_1}{nM}}\right), \\ \text{then updated using Gradient Descent} \end{array} \right\} \tag{203}$$

Finally, putting the previous Lemmas C.1, C.2 and C.3 together we get the result that relates generalization to the NTK:

**Theorem C.4.** *Consider the prediction task defined in Section 2 and the hypothesis class $\mathcal{H}_{trained}$ of graph filters trained using Gradient Descent. Under the assumption that $|\ell(\boldsymbol{h}, z)| = ||\sum_{k=0}^{K-1} h_k S^k \mathbf{x}_i - \mathbf{y}_i||_2^2 \leq \rho^2$, $\forall(\mathbf{x}_i, \mathbf{y}_i) \in S, \boldsymbol{h} \in \mathcal{H}_{trained}$, with probability of at least $1 - \delta$, for all $h \in \mathcal{H}_{trained}$, we have*

$$L_\mathcal{D}(\ell(h)) - L_S(\ell(h)) \leq 2\rho\sqrt{\frac{2K \cdot (\max_{k,i} ||S^k \mathbf{x}_i||_2^2) \cdot (\tilde{\mathbf{y}}^\mathsf{T} \tilde{\mathbf{\Theta}}^\dagger \tilde{\mathbf{y}})}{M}} + 4\rho^2\sqrt{\frac{2\ln(4/\delta_2)}{M}} \tag{204}$$

*where $\delta = \delta_1 + \delta_2$. In particular, (204) holds for $h = \mathrm{ERM}_\mathcal{H}(S)$ which is the solution of the empirical risk minimization problem.*

Theorem C.4 reveals that the upper bound on generalization error is proportional to the term $\sqrt{\tilde{\mathbf{y}}^\mathsf{T} \tilde{\mathbf{\Theta}}^\dagger \tilde{\mathbf{y}}}$. While maximizing the alignment i.e., $\mathcal{A} = \tilde{\mathbf{y}}^\mathsf{T} \tilde{\mathbf{\Theta}} \tilde{\mathbf{y}}$ and minimizing the term $\tilde{\mathbf{y}}^\mathsf{T} \tilde{\mathbf{\Theta}}^\dagger \tilde{\mathbf{y}}$ are clearly not identical objectives, there is a close relationship between the two as formalized in the following result (Theorem 2 from (Wang et al., 2022a)):

$$\frac{\tilde{\mathbf{y}}^\mathsf{T} \tilde{\mathbf{y}}}{\mathcal{A}(X, Y, S)} \leq \tilde{\mathbf{y}}^\mathsf{T} \tilde{\mathbf{\Theta}}^\dagger \tilde{\mathbf{y}} \leq \frac{\lambda_{\max}(\tilde{\mathbf{\Theta}})}{\lambda_{\min}(\tilde{\mathbf{\Theta}})} \frac{\tilde{\mathbf{y}}^\mathsf{T} \tilde{\mathbf{y}}}{\mathcal{A}(X, Y, S)} \tag{205}$$

[7] (205) tells us that for a class of predictors where the ratio of the largest and smallest eigenvalues of the NTK i.e. $\frac{\lambda_{\max}(\tilde{\mathbf{\Theta}})}{\lambda_{\min}(\tilde{\mathbf{\Theta}})}$ is more or less constant between different predictors, the generalization error bound given in Theorem C.4 is governed by $1/\mathcal{A}(X, Y, S)$. This means within such a class, predictors with larger alignment are likely to have a smaller generalization error. The question remains that for the classes of predictors discussed within the paper, namely Graph filters and two-layer GNNs, how much does $\frac{\lambda_{\max}(\tilde{\mathbf{\Theta}})}{\lambda_{\min}(\tilde{\mathbf{\Theta}})}$ vary between predictors. This is an avenue for potential future work.

[6] If $\tilde{\mathbf{\Theta}}$ is full rank then this becomes $\sqrt{\tilde{\mathbf{y}}^\mathsf{T} \tilde{\mathbf{\Theta}}^{-1} \tilde{\mathbf{y}}}$

[7] Since in our case $\tilde{\mathbf{\Theta}}$ isn't full-rank, by $\lambda_{\min}(\tilde{\mathbf{\Theta}})$ we mean the smallest eigenvalue of $\tilde{\mathbf{\Theta}}$ that is greater than 0.

## D. Why the NTK is constant for a two-layer GNN with infinite width

We start this section with the following proposition from (Liu et al., 2020):

**Proposition D.1** ((Small Hessian norm implies small change in tangent kernel))**.** *Given a point $\mathbf{w}_0 \in \mathbb{R}^p$ and a ball $B(\mathbf{w}_0, R) := \{\mathbf{w} \in \mathbb{R}^p : \|\mathbf{w} - \mathbf{w}_0\| \leq R\}$ with fixed radius $R > 0$, if the Hessian matrix satisfies $\|H(\mathbf{w})\| < \epsilon$, where $\epsilon > 0$, for all $\mathbf{w} \in B(\mathbf{w}_0, R)$, then the tangent kernel $K(\mathbf{w})$ of the model, as a function of $\mathbf{w}$, satisfies*

$$\left|K_{(\mathbf{x},\mathbf{z})}(\mathbf{w}) - K_{(\mathbf{x},\mathbf{z})}(\mathbf{w}_0)\right| = \mathcal{O}(\epsilon R), \quad \forall \mathbf{w} \in B(\mathbf{w}_0, R), \forall \mathbf{x}, \mathbf{z} \in \mathbb{R}^d$$

*Remark* D.2. It will now suffice to show that the norm of the Hessian matrix $||H||$ is sufficiently small if we choose our network width $F$ large enough. This means if $F$ is chosen to be large enough, the NTK will be almost constant within a ball of arbitrary fixed radius $R$ around initialization.

Note that the above proposition is given for the case where the network output $f$ is a scalar and an element of the NTK is defined as $K_{(\mathbf{x}_i,\mathbf{x}_j)}(\mathbf{w}) := \nabla f_{\mathbf{x}_i}(\mathbf{w})^\mathsf{T} \nabla f_{\mathbf{x}_j}(\mathbf{w})$. Since for a GNN the output is a vector $\boldsymbol{f}_{\mathbf{x}}(\boldsymbol{h})$, we will consider the Hessian of a network with a scalar output equal to the first element of this vector which we'll call $f_1(\boldsymbol{h})$. Also for illustration purposes, we will consider a GNN where each filter only has a single coefficient (e.g. the $i$-th filter in the first layer: $G_i(S) = g_i S$ and the $j$-th filter in the second layer: $H_j(S) = h_j S$). Similar end results hold for GNNs with filters that have $K > 1$ coefficients. We now derive the different elements of the Hessian.

$$\frac{\partial^2 f_1}{\partial g_i \partial g_j} = \begin{cases} \frac{1}{\sqrt{F}} \left(h_i S \mathbf{diag}\left(\mathbf{diag}\left(\sigma''\left(g_i S \mathbf{x}\right)\right) S\mathbf{x}\right) S\mathbf{x}\right)_1, & \text{if } i = j \\ 0, & \text{otherwise} \end{cases} \tag{206}$$

$$\frac{\partial^2 f_1}{\partial h_i \partial h_j} = 0 \tag{207}$$

$$\frac{\partial^2 f_1}{\partial g_i \partial h_j} = \begin{cases} \frac{1}{\sqrt{F}} \left(S \mathbf{diag}\left(\sigma'\left(g_i S\mathbf{x}\right) S\mathbf{x}\right)\right)_1, & \text{if } i = j \\ 0, & \text{otherwise} \end{cases} \tag{208}$$

The Hessian can be written as follows:

$$H = \begin{bmatrix} H_{gg} & H_{gh} \\ (H_{gh})^\mathsf{T} & H_{hh} \end{bmatrix} \tag{209}$$

where each of the sub-matrices $H_{gg}, H_{gh}$ are diagonal $F \times F$ matrices and $H_{hh} = 0$.

$$||H|| = || \begin{bmatrix} H_{gg} & 0 \\ 0 & 0 \end{bmatrix} + \begin{bmatrix} 0 & H_{gh} \\ (H_{gh})^\mathsf{T} & 0 \end{bmatrix} || \leq || \begin{bmatrix} H_{gg} & 0 \\ 0 & 0 \end{bmatrix} || + || \begin{bmatrix} 0 & H_{gh} \\ (H_{gh})^\mathsf{T} & 0 \end{bmatrix} || \tag{210}$$

$$= \max_i |(H_{gg})_{ii}| + \max_i |(H_{gh})_{ii}| = \max_i | \left(\frac{\partial^2 f_1}{\partial^2 g_i}\right) | + \max_i | \left(\frac{\partial^2 f_1}{\partial g_i \partial h_i}\right) | \tag{211}$$

$$\Rightarrow ||H|| \leq \max_i | \left(\frac{\partial^2 f_1}{\partial^2 g_i}\right) | + \max_i | \left(\frac{\partial^2 f_1}{\partial g_i \partial h_i}\right) | \tag{212}$$

We will assume the following. The function $\sigma(.)$ is twice differentiable and the magnitude of its second derivative is at most $B_\sigma$ (e.g. tanh or Sigmoid). We also recall that our input data has been normalized such that $||\mathbf{x}||_2 \leq 1$. We will also assume $||S||_{\mathsf{op}} \leq \nu$.

$$\max_i | \left(\frac{\partial^2 f_1}{\partial^2 g_i}\right) | = \max_i | \frac{1}{\sqrt{F}} \left(h_i S \mathbf{diag}\left(\mathbf{diag}\left(\sigma''\left(g_i S\mathbf{x}\right)\right) S\mathbf{x}\right) S\mathbf{x}\right)_1 | \tag{213}$$

$$\leq \max_i || \frac{1}{\sqrt{F}} h_i S \mathbf{diag}\left(\mathbf{diag}\left(\sigma''\left(g_i S\mathbf{x}\right)\right) S\mathbf{x}\right) S\mathbf{x} ||_\infty \tag{214}$$

$$\leq \max_i \frac{1}{\sqrt{F}} h_i ||S\mathbf{diag}\left(\mathbf{diag}\left(\sigma''\left(g_i S\mathbf{x}\right)\right) S\mathbf{x}\right) S||_{\mathsf{op}} ||\mathbf{x}||_2 \tag{215}$$

$$\leq \max_i \frac{1}{\sqrt{F}} h_i ||S||_{\mathsf{op}}^2 ||\mathbf{diag}\left(\mathbf{diag}\left(\sigma''\left(g_i S\mathbf{x}\right)\right) S\mathbf{x}\right)||_{\mathsf{op}} \tag{216}$$

For the rightmost term in (216) we can write:

$$||\mathbf{diag}\left(\mathbf{diag}\left(\sigma''\left(g_i S\mathbf{x}\right)\right) S\mathbf{x}\right)||_{\mathsf{op}} \leq ||\mathbf{diag}\left(\sigma''\left(g_i S\mathbf{x}\right)\right) S\mathbf{x}||_\infty \leq B_\sigma ||S||_{\mathsf{op}} ||\mathbf{x}||_2 \tag{217}$$

using (216) and (217) we get:

$$\max_i |\left(\frac{\partial^2 f_1}{\partial^2 g_i}\right)| \leq (\max_i h_i) \frac{1}{\sqrt{F}} B_\sigma ||S||_{\mathsf{op}}^3 = \mathcal{O}(\frac{1}{\sqrt{F}}) \tag{218}$$

We can similarly show that $\max_i |\left(\frac{\partial^2 f_1}{\partial g_i \partial h_i}\right)| = \mathcal{O}(\frac{1}{\sqrt{F}})$. using these and (212) we conclude:

$$||H|| = \mathcal{O}(\frac{1}{\sqrt{F}}) \tag{219}$$

The important take away is the order of $||H||$ in terms of $F$. note that even if we set aside the simplifying assumption that each filter has only a single coefficient, it still won't be too difficult to show that $||H|| = \mathcal{O}(\frac{1}{\sqrt{F}})$ since $H$ will be similarly sparse with $\mathcal{O}(K)$ number of non zero diagonals, and aside from the factor of $\frac{1}{\sqrt{F}}$, none of its elements depend on $F$. Going back to proposition D.1 we conclude that for the two-layer GNN discussed in this paper, as $F \to \infty$ the NTK converges to a constant matrix.

## E. Training the First Layer

The NTK, and subsequently the alignment, for the case where we train the filter coefficients of both layers is equal to the sum of the cases where we train only the first layer and only the second layer respectively. We analyzed alignment when training the second layer in Section 3. For completeness, here we analyze the alignment when only training the first layer to show that similar results hold.

The NTK for the two-layer GNN where we randomly initialize all filter coefficients by sampling i.i.d from a Gaussian distribution and then only train the filter coefficients in the first layer, is the first term of the NTK in Proposition 3.6. It is re-stated here as follows.

$$\tilde{\mathbf{\Theta}}_{GNN}^{(1)}(\boldsymbol{h}) = \frac{1}{F}\sum_{f=1}^{F}\sum_{k=0}^{K-1}\left(\mathbf{c}_{f,k}^{(1)}\right)\left(\mathbf{c}_{f,k}^{(1)}\right)^{\mathsf{T}} \tag{220}$$

where we recall from (26) that:

$$\mathbf{c}_{f,k}^{(1)} = H_f(\tilde{S}) \cdot \mathbf{diag}(\sigma'(G_f(\tilde{S})\tilde{\mathbf{x}})\tilde{S}^k\tilde{\mathbf{x}}) \tag{221}$$

In the asymptote of the width of the hidden layer, i.e., $F \to \infty$, we have

$$\tilde{\mathbf{\Theta}}_{GNN}^{(1)}(\boldsymbol{h}) = \lim_{F\to\infty}\frac{1}{F}\sum_{f=1}^{F}\sum_{k=0}^{K-1}\left(H_f(\tilde{S})\cdot\mathbf{diag}(\sigma'(G_f(\tilde{S})\tilde{\mathbf{x}})\tilde{S}^k\tilde{\mathbf{x}})\right)\left(H_f(\tilde{S})\cdot\mathbf{diag}(\sigma'(G_f(\tilde{S})\tilde{\mathbf{x}})\tilde{S}^k\tilde{\mathbf{x}})\right)^{\mathsf{T}} \tag{222}$$

$$= \mathop{\mathbb{E}}_{\boldsymbol{g}\sim\mathcal{N}(0,I),\,\boldsymbol{h}\sim\mathcal{N}(0,I)}\left[\sum_{k=0}^{K-1}\left(H(\tilde{S})\cdot\mathbf{diag}(\sigma'(G(\tilde{S})\tilde{\mathbf{x}})\tilde{S}^k\tilde{\mathbf{x}})\right)\left(H(\tilde{S})\cdot\mathbf{diag}(\sigma'(G(\tilde{S})\tilde{\mathbf{x}})\tilde{S}^k\tilde{\mathbf{x}})\right)^{\mathsf{T}}\right] \tag{223}$$

We begin by focusing on the expectation over $\boldsymbol{h}$, such that,

$$\tilde{\mathbf{\Theta}}_{GNN}^{(1)}(\boldsymbol{h}) = \sum_{k=0}^{K-1}\mathop{\mathbb{E}}_{\boldsymbol{g}\sim\mathcal{N}(0,I)}\left[\mathop{\mathbb{E}}_{\boldsymbol{h}\sim\mathcal{N}(0,I)}\left[\left(\sum_{k'=0}^{K-1}h_{k'}\tilde{S}^{k'}\mathbf{diag}(\sigma'(G(\tilde{S})\tilde{\mathbf{x}})\tilde{S}^k\tilde{\mathbf{x}})\right)\right.\right.$$
$$\left.\left.\times\left(\sum_{k''=0}^{K-1}h_{k''}\tilde{S}^{k''}\mathbf{diag}(\sigma'(G(\tilde{S})\tilde{\mathbf{x}})\tilde{S}^k\tilde{\mathbf{x}})\right)^{\mathsf{T}}\right]\right] \tag{224}$$

We first evaluate the inner expected value from (224) with respect to $\boldsymbol{h}$:

$$\mathop{\mathbb{E}}_{\boldsymbol{h}\sim\mathcal{N}(0,I)}\left[\left(\sum_{k'=0}^{K-1} h_{k'}\tilde{S}^{k'}\mathbf{diag}(\sigma'(G(\tilde{S})\tilde{\mathbf{x}})\tilde{S}^k\tilde{\mathbf{x}})\right)\left(\sum_{k''=0}^{K-1} h_{k''}\tilde{S}^{k''}\mathbf{diag}(\sigma'(G(\tilde{S})\tilde{\mathbf{x}})\tilde{S}^k\tilde{\mathbf{x}})\right)^{\mathsf{T}}\right] \tag{225}$$

$$= \sum_{k'=0}^{K-1}\sum_{k''=0}^{K-1}\mathop{\mathbb{E}}_{\boldsymbol{h}\sim\mathcal{N}(0,I)}\left[h_{k'}h_{k''}\left(\tilde{S}^{k'}\mathbf{diag}(\sigma'(G(\tilde{S})\tilde{\mathbf{x}})\tilde{S}^k\tilde{\mathbf{x}})\right)\left(\tilde{S}^{k''}\mathbf{diag}(\sigma'(G(\tilde{S})\tilde{\mathbf{x}})\tilde{S}^k\tilde{\mathbf{x}})\right)^{\mathsf{T}}\right] \tag{226}$$

$$= \sum_{k'=0}^{K-1}\left(\tilde{S}^{k'}\mathbf{diag}(\sigma'(G(\tilde{S})\tilde{\mathbf{x}})\tilde{S}^k\tilde{\mathbf{x}})\right)\left(\tilde{S}^{k'}\mathbf{diag}(\sigma'(G(\tilde{S})\tilde{\mathbf{x}})\tilde{S}^k\tilde{\mathbf{x}})\right)^{\mathsf{T}} \tag{227}$$

Above, in (227) we used the fact that $\mathop{\mathbb{E}}_{\boldsymbol{h}\sim\mathcal{N}(0,I)}[h_k h_{k'}] = \delta_{kk'}$. Now we can replace the inner expectation with respect to $\boldsymbol{h}$ in (224) with the quantity from (227) to get

$$\tilde{\boldsymbol{\Theta}}^{(1)}_{GNN}(\boldsymbol{h}) = \sum_{k=0}^{K-1}\mathop{\mathbb{E}}_{\boldsymbol{g}\sim\mathcal{N}(0,I)}\left[\sum_{k'=0}^{K-1}\left(\tilde{S}^{k'}\mathbf{diag}(\sigma'(G(\tilde{S})\tilde{\mathbf{x}})\tilde{S}^k\tilde{\mathbf{x}})\right)\left(\tilde{S}^{k'}\mathbf{diag}(\sigma'(G(\tilde{S})\tilde{\mathbf{x}})\tilde{S}^k\tilde{\mathbf{x}})\right)^{\mathsf{T}}\right] \tag{228}$$

$$= \sum_{k'=0}^{K-1}\tilde{S}^{k'}\mathop{\mathbb{E}}_{\boldsymbol{g}\sim\mathcal{N}(0,I)}\left[\sum_{k=0}^{K-1}\left(\mathbf{diag}(\sigma'(G(\tilde{S})\tilde{\mathbf{x}})\tilde{S}^k\tilde{\mathbf{x}})\right)\left(\mathbf{diag}(\sigma'(G(\tilde{S})\tilde{\mathbf{x}})\tilde{S}^k\tilde{\mathbf{x}})\right)^{\mathsf{T}}\right]\tilde{S}^{k'} \tag{229}$$

Now we turn our attention to the expectation in (229) which we shall call $E^{(1)} \in \mathbb{R}^{nM\times nM}$[8].

$$E^{(1)} = \mathop{\mathbb{E}}_{\boldsymbol{g}\sim\mathcal{N}(0,I)}\left[\sum_{k=0}^{K-1}\left(\mathbf{diag}(\sigma'(G(\tilde{S})\tilde{\mathbf{x}})\tilde{S}^k\tilde{\mathbf{x}})\right)\left(\mathbf{diag}(\sigma'(G(\tilde{S})\tilde{\mathbf{x}})\tilde{S}^k\tilde{\mathbf{x}})\right)^{\mathsf{T}}\right] \tag{230}$$

$$\Rightarrow (E^{(1)})_{ab} = \mathop{\mathbb{E}}_{\boldsymbol{g}\sim\mathcal{N}(0,I)}\left[\sigma'\left(\langle\boldsymbol{g},\boldsymbol{z}^{(a)}\rangle\right)\cdot\sigma'\left(\langle\boldsymbol{g},\boldsymbol{z}^{(b)}\rangle\right)\right]\cdot\sum_{k=0}^{K-1}(\tilde{S}^k\tilde{x})_a(\tilde{S}^k\tilde{x})_b \tag{231}$$

$$= \mathop{\mathbb{E}}_{\boldsymbol{g}\sim\mathcal{N}(0,I)}\left[\sigma'\left(\langle\boldsymbol{g},\boldsymbol{z}^{(a)}\rangle\right)\cdot\sigma'\left(\langle\boldsymbol{g},\boldsymbol{z}^{(b)}\rangle\right)\right]\cdot\langle\boldsymbol{z}^{(a)},\boldsymbol{z}^{(b)}\rangle \tag{232}$$

Similar to our analysis in Section 3.2, we begin by considering the case where the non-linearity is an identity function, i.e., $\sigma(z) = z$ which implies that $\sigma'(z) = 1$:

$$\sigma'\left(\langle\boldsymbol{g},\boldsymbol{z}^{(a)}\rangle\right) = \sigma'\left(\langle\boldsymbol{g},\boldsymbol{z}^{(b)}\rangle\right) = 1 \tag{233}$$

For this linear case, we shall name the expectation from (230), $B^{(1)}_{\mathsf{lin}} \in \mathbb{R}^{nM\times nM}$. Using (232) and (233) we can write the elements of $B^{(1)}_{\mathsf{lin}}$ as

$$(B^{(1)}_{\mathsf{lin}})_{ab} = \langle\boldsymbol{z}^{(a)},\boldsymbol{z}^{(b)}\rangle \tag{234}$$

Thus, our analysis in this context renders (234), which is the same conclusion as that for the alignment when we only train the second layer (see (34)).

Next, we analyze the expectation matrix $E^{(1)}$ when $\sigma(\cdot)$ is non-linear. In this non-linear case, for each element of $E^{(1)}$ we have from (232):

$$(E^{(1)})_{ab} = \mathop{\mathbb{E}}_{u,u'\sim\mathcal{N}(0,\Lambda)}\left[\sigma'\left(||\boldsymbol{z}^{(a)}||_2\cdot u\right)\cdot\sigma'\left(||\boldsymbol{z}^{(b)}||_2\cdot u'\right)\right]\cdot\langle\boldsymbol{z}^{(a)},\boldsymbol{z}^{(b)}\rangle \tag{235}$$

The Hermite expansion of the two functions in (235) is given by

$$\sigma'\left(||\boldsymbol{z}^{(a)}||_2\cdot u\right) = \sum_{\ell=0}^{\infty}\alpha_\ell\cdot p_\ell(u), \quad \text{and} \quad \sigma'\left(||\boldsymbol{z}^{(b)}||_2\cdot u'\right) = \sum_{\ell'=0}^{\infty}\beta_{\ell'}\cdot p_{\ell'}(u') \tag{236}$$

[8]The superscript (1) denotes that these matrices are defined for the analysis of the NTK for the first layer in contrast to those defined in the main body of the paper

Inserting (236) into (235), we get

$$(E^{(1)})_{ab} = \sum_{\ell=0}^{\infty}\sum_{\ell'=0}^{\infty} \alpha_\ell \beta_{\ell'} \mathop{\mathbb{E}}_{u,u'\sim\mathcal{N}(0,\Lambda)} [p_\ell(u)p_{\ell'}(u')] \cdot \langle \boldsymbol{z}^{(a)}, \boldsymbol{z}^{(b)} \rangle \tag{237}$$

$$= \sum_{\ell=0}^{\infty} \alpha_\ell \beta_\ell \cdot \left(\frac{\langle \boldsymbol{z}^{(a)}, \boldsymbol{z}^{(b)} \rangle}{||\boldsymbol{z}^{(a)}||_2 \cdot ||\boldsymbol{z}^{(b)}||_2}\right)^l \cdot \langle \boldsymbol{z}^{(a)}, \boldsymbol{z}^{(b)} \rangle \tag{238}$$

We recall that for simpler analysis, we have analyzed the case where the non-linearity is the $\tanh$ function and hence, the derivative of the activation i.e., $\sigma'(z) = \frac{1}{\cosh^2(z)}$, is an even function. This observation further leads to the Hermite expansion coefficients $\alpha_\ell, \beta_\ell$ being zero whenever $\ell$ is odd. With these considerations, we divide the expansion from (238) into the two following parts and name them $B^{(1)}$ and $\Delta B^{(1)}$ respectively:

$$(E^{(1)})_{ab} = \underbrace{\alpha_0\beta_0 \cdot \langle \boldsymbol{z}^{(a)}, \boldsymbol{z}^{(b)} \rangle}_{(B^{(1)})_{ab}} + \underbrace{\sum_{\ell=2,4,\cdots}^{\infty} \alpha_\ell \beta_\ell \cdot \left(\frac{\langle \boldsymbol{z}^{(a)}, \boldsymbol{z}^{(b)} \rangle}{||\boldsymbol{z}^{(a)}||_2 \cdot ||\boldsymbol{z}^{(b)}||_2}\right)^\ell \cdot \langle \boldsymbol{z}^{(a)}, \boldsymbol{z}^{(b)} \rangle}_{(\Delta B^{(1)})_{ab}} \tag{239}$$

Now, recalling (31) the alignment, which we will call $\mathcal{A}^{(1)}$ here to emphasize that we are only training the first layer, becomes:

$$\mathcal{A}^{(1)} = \textbf{tr}(QE^{(1)}) = \textbf{tr}(QB^{(1)}) + \textbf{tr}(Q\Delta B^{(1)}) \tag{240}$$

Focusing on the first term in (240), we define the family of hermite transforms of the function $\frac{1}{\cosh^2(||\boldsymbol{z}^{(a)}||_2 u)}$ as $\tau_l(\cdot)$ for $l = 0, 1, 2, \cdots$ :

$$\tau_\ell(||\boldsymbol{z}^{(a)}||_2^2) \triangleq \int_{-\infty}^{\infty} \frac{1}{\cosh^2(||\boldsymbol{z}^{(a)}||_2 u)} \cdot p_\ell(u) \cdot e^{-u^2/2} du = \alpha_\ell \tag{241}$$

Note that $\tau_0(\cdot)$ is similar in functionality to the function $\hat{\sigma}(\cdot)$ defined in (101). Now, using the fact that $(B_{\mathsf{lin}})_{aa} = \langle \boldsymbol{z}^{(a)}, \boldsymbol{z}^{(a)} \rangle = ||\boldsymbol{z}^{(a)}||_2^2$, we have

$$(B^{(1)})_{ab} = \tau_0((B_{\mathsf{lin}})_{aa}) \cdot \tau_0((B_{\mathsf{lin}})_{bb}) \cdot (B_{\mathsf{lin}})_{ab} \tag{242}$$

$$\Rightarrow B^{(1)} = \tau_0(\textbf{diag}(B_{\mathsf{lin}})) \cdot B_{\mathsf{lin}} \cdot \tau_0(\textbf{diag}(B_{\mathsf{lin}})) \tag{243}$$

Therefore, similar to (109) from the proof of Lemma 3.11, we have

$$\lambda_{\mathsf{min}}^2 \mathcal{A}_{\mathsf{lin}} \leq \textbf{tr}(QB^{(1)}) \tag{244}$$

where $\lambda_{\mathsf{min}} \triangleq \min_a \tau_0(||\boldsymbol{z}^{(a)}||_2^2)$. From equations (111)-(115) and with the assumption from (116) i.e. $||S||_{\mathsf{op}} \leq \nu$ we have:

$$\lambda_{\mathsf{min}}^2 \geq \rho^{(1)} \tag{245}$$

$$\text{where } \rho^{(1)} \triangleq \left(\tau_0\left(\sum_{k=0}^{K-1} \nu^{2k}\right)\right)^2 \tag{246}$$

which together with (244) gives us the following similar to Lemma 3.11:

$$\textbf{tr}(QB^{(1)}) \geq \rho^{(1)} \mathcal{A}_{\mathsf{lin}} \tag{247}$$

Next, we aim to show that a result similar to Lemma 3.12 holds for this scenario, as this allows us to conclude that Theorem 3.13 also holds for the case when alignment is optimized based on the first layer. We will now check to see whether the element-wise inequality from Lemma 3.12 also holds here.

From (239) and using the definition from (241), we have

$$(\Delta B^{(1)})_{ab} = \langle \boldsymbol{z}^{(a)}, \boldsymbol{z}^{(b)} \rangle \sum_{i=1}^{\infty} \alpha_{2i}\beta_{2i} \cdot \left(\frac{\langle \boldsymbol{z}^{(a)}, \boldsymbol{z}^{(b)} \rangle}{||\boldsymbol{z}^{(a)}||_2 \cdot ||\boldsymbol{z}^{(b)}||_2}\right)^{2i} \tag{248}$$

$$= \langle \boldsymbol{z}^{(a)}, \boldsymbol{z}^{(b)} \rangle \sum_{i=1}^{\infty} \tau_{2i}(||\boldsymbol{z}^{(a)}||_2^2) \cdot \tau_{2i}(||\boldsymbol{z}^{(b)}||_2^2) \cdot \left(\frac{\langle \boldsymbol{z}^{(a)}, \boldsymbol{z}^{(b)} \rangle}{||\boldsymbol{z}^{(a)}||_2 \cdot ||\boldsymbol{z}^{(b)}||_2}\right)^{2i} \tag{249}$$

Similar to the family of functions $g_\ell$, it can readily be verified numerically that for a given $\ell$, we either have $\tau_\ell(y) \geq 0,\ \forall y \geq 0$ or $\tau_\ell(y) \leq 0,\ \forall y \geq 0$.[9] Hence, $\tau_{2i}(||\boldsymbol{z}^{(a)}||_2^2) \cdot \tau_{2i}(||\boldsymbol{z}^{(b)}||_2^2) \geq 0$ and we can conclude that $(\Delta B^{(1)})_{ab}$ and $(B^{(1)})_{ab}$ have the same sign, which is the sign of $\langle \boldsymbol{z}^{(a)}, \boldsymbol{z}^{(b)} \rangle$. Now, for the case where $\langle \boldsymbol{z}^{(a)}, \boldsymbol{z}^{(b)} \rangle \geq 0$, we have:

$$\begin{aligned}
&\sum_{i=1}^{\infty} \tau_{2i}(||\boldsymbol{z}^{(a)}||_2^2) \cdot \tau_{2i}(||\boldsymbol{z}^{(b)}||_2^2) \cdot \left( \frac{\langle \boldsymbol{z}^{(a)}, \boldsymbol{z}^{(b)} \rangle}{||\boldsymbol{z}^{(a)}||_2 \cdot ||\boldsymbol{z}^{(b)}||_2} \right)^{2i} \cdot \langle \boldsymbol{z}^{(a)}, \boldsymbol{z}^{(b)} \rangle \\
&\quad \leq \sum_{i=1}^{\infty} \tau_{2i}(||\boldsymbol{z}^{(a)}||_2^2) \cdot \tau_{2i}(||\boldsymbol{z}^{(b)}||_2^2) \cdot \langle \boldsymbol{z}^{(a)}, \boldsymbol{z}^{(b)} \rangle \qquad (250) \\
&\quad = \frac{\left( \sum_{i=1}^{\infty} \tau_{2i}(||\boldsymbol{z}^{(a)}||_2^2) \cdot \tau_{2i}(||\boldsymbol{z}^{(b)}||_2^2) \right)}{\tau_0(||\boldsymbol{z}^{(a)}||_2^2) \cdot \tau_0(||\boldsymbol{z}^{(b)}||_2^2)} \cdot (B^{(1)})_{ab} \qquad (251)
\end{aligned}$$

It is straightforward to check numerically that $\left| \frac{\tau_{2i}(||\boldsymbol{z}^{(a)}||_2^2)}{\tau_0(||\boldsymbol{z}^{(a)}||_2^2)} \right|$ is increasing in $||\boldsymbol{z}^{(a)}||_2,\ \forall i \geq 1$.[10] Hence, we can continue from (248) and (251) to have

$$\begin{aligned}
(\Delta B^{(1)})_{ab} &\leq \frac{\left( \sum_{i=1}^{\infty} \tau_{2i}(||\boldsymbol{z}^{(a)}||_2^2) \cdot \tau_{2i}(||\boldsymbol{z}^{(b)}||_2^2) \right)}{\tau_1(||\boldsymbol{z}^{(a)}||_2^2) \cdot \tau_1(||\boldsymbol{z}^{(b)}||_2^2)} \cdot B_{ab} \qquad (252) \\
&\leq \left( \frac{\sum_{i=1}^{\infty} (\tau_{2i}((||\boldsymbol{z}||_2^2)_{max}))^2}{(\tau_0((||\boldsymbol{z}||_2^2)_{max}))^2} \right) (B^{(1)})_{ab} \qquad (253) \\
&= \beta^{(1)} \cdot (B^{(1)})_{ab} \qquad (254)
\end{aligned}$$

where

$$\beta^{(1)} \triangleq \left( \frac{\sum_{i=1}^{\infty} (\tau_{2i}((||\boldsymbol{z}||_2^2)_{max}))^2}{(\tau_0((||\boldsymbol{z}||_2^2)_{max}))^2} \right) \qquad (255)$$

and $(||\boldsymbol{z}||_2^2)_{max} = \max_{a'}(||\boldsymbol{z}_{a'}||_2^2)$. In the proof of Lemma 3.12, we made no further assumptions and considered the worst case upper bound on $\Delta B_{ab}$ when $(||\boldsymbol{z}||_2^2)_{max}$ is infinitely large. But a similar approach cannot be adopted here since the limit of the sum $\lim_{y \to \infty} \sum_{\ell=1}^{\infty} (\tau_{2i}(y))^2$ is unbounded. However, given the assumptions on the data and the shift operator $S$ so far and with some additional mild assumptions, it is possible to upper bound $(||\boldsymbol{z}||_2^2)_{max}$ and thus, derive a meaningful expression for constant $\beta$. Recall the definition of $\boldsymbol{z}_\ell \in \mathbb{R}^K$:

$$\boldsymbol{z}_\ell \triangleq \left[ \tilde{\mathbf{x}}_\ell,\ (\tilde{S}\tilde{\mathbf{x}})_\ell,\ \cdots,\ (\tilde{S}^{K-1}\tilde{\mathbf{x}})_\ell \right]^{\mathsf{T}} \qquad (256)$$

For the $k$-th element of $\boldsymbol{z}_\ell$ we can write:

$$(\tilde{S}^k \tilde{\mathbf{x}})_\ell \leq \max_i ||S^k \mathbf{x}_i||_\infty \leq \max_i ||S^k \mathbf{x}_i||_2 \leq \max_i ||S^k||_{\mathsf{op}} ||\mathbf{x}_i||_2 \leq ||S^k||_{\mathsf{op}} \qquad (257)$$

$$\Rightarrow ||\boldsymbol{z}_\ell||_2^2 \leq \sum_{k=0}^{K-1} ||S^k||_{\mathsf{op}}^2 \qquad (258)$$

In order to give an upper bound on the maximum possible value for $||\boldsymbol{z}_\ell||_2^2$, we need an upper bound on $||S||_{\mathsf{op}}$. To see why such an upper bound makes sense, recall the constraint from Lemma 3.4: $||\sum_{k=0}^{K-1} S^k||_F \leq \sqrt{\alpha/(\eta M)}$. One straightforward way to make sure that this constraint is satisfied, is to normalize the shift operator $S$, such that its Frobenius norm is bounded (which is indeed the method used in the experiments for this paper. See Appendix E). Assuming that $||S||_F \leq \frac{1}{K}\sqrt{\alpha/(\eta M)} \leq 1$, we have

$$||\sum_{k=0}^{K-1} S^k||_F \leq \sum_{k=0}^{K-1} ||S^k||_F \leq \sum_{k=0}^{K-1} ||S||_F^k \leq K||S||_F \leq \sqrt{\alpha/(\eta M)} \qquad (259)$$

[9]A simple Python script can be found in https://github.com/shervinkhal/Cross_Covariance_NTK that plots $\tau_\ell(y)$ against $y$ for any given index $\ell$. See the file "numerical_verification_3.py"

[10]A simple Python script can be found in https://github.com/shervinkhal/Cross_Covariance_NTK that plots $|\frac{\tau_{2i}(y)}{\tau_0(y)}|$ against $y$ for any given index $i$. See the file "numerical_verification_4.py"

Since in practice we don't know precisely what the constant $\alpha$ should be, we opt to simply normalize $S$ so that $||S||_F = 1$. Therefore:

$$||S||_{\mathsf{op}} \leq ||S||_F = 1 \Rightarrow ||\boldsymbol{z}_\ell||_2^2 \leq \sum_{k=0}^{K-1} ||S^k||_{\mathsf{op}}^2 \leq K \Rightarrow (||\boldsymbol{z}||_2)_{max} \leq \sqrt{K} \tag{260}$$

Going back to (255), with the assumption in (260) we have

$$\beta^{(1)} = \left( \frac{\sum_{i=1}^{\infty} (\tau_{2i}(K))^2}{(\tau_0(K))^2} \right) \tag{261}$$

The above constant can be numerically evaluated for different values of $K$. For example, for $K = 3$, we have $\beta^{(1)} = 0.7320$ which is close to the constant we had when training only the second layer ($\beta = 0.57$, see (128)). Now that we've shown similar results to Lemma 3.11 and Lemma 3.12 (see (247) and (255) respectively) for this case where we train only the first layer, we can conclude with a result similar to Theorem 3.13 which we shall present as the following corollary:

**Corollary E.1.** *Under the assumption $\mathcal{A}_{\mathsf{lin}} = \textbf{tr}\,(QB_{\mathsf{lin}}) \geq \xi \cdot ||Q||_F ||B_{\mathsf{lin}}||_F$, $\mathcal{A}_{\mathsf{lin}}$ lower bounds the alignment for the two-layer GNN with* $\tanh$ *non-linearity where we only train the first layer, $\mathcal{A}^{(1)}$, up to a constant as follows*

$$\mathcal{A}^{(1)} \geq \left(b - \frac{s}{\xi}\right)\mathcal{A}_{\mathsf{lin}}\ , \tag{262}$$

*for some constants positive constants $b$ and $s$ and* $0 \leq \xi \leq 1$.

## F. Additional Experimental Details and Results

### F.1. Other Datasets

We use a similar setup as described in Appendix F.2 to conduct some preliminary experiments on two other public datasets. These two datasets have been previously investigated in (Cao et al., 2020), although for a different variation of forecasting task.

**Traffic Flow Dataset.** We utilize the PEMS07 traffic flow dataset (Chen et al., 2001) for traffic flow prediction. The data collected is from the California Department of Transportation network. It is an $n = 228$-dimensional time-series with $N = 12671$ time steps. The time interval between each consecutive point in the time series is 5 minutes.

**Temperature dataset** The dataset contains high temporal resolution (hourly measurements) data of various weather attributes, such as temperature, humidity, air pressure, etc gathered from the OpenWeatherMap website over a  5 year period during 2012-2017. We used the temperature data available for 30 US and Canadian Cities as our time series dataset[11].

For each dataset, we created $N_{train} = 1000$ and $N_{test} = 100$ training and test samples respectively by randomly sampling pairs of vectors $\boldsymbol{z}^{(t)}, \boldsymbol{z}^{(t+\Delta t)}$ from the respective time series. Next, the normalized sample covariance and sample cross covariance matrices were constructed using only the training data. Note that for both of these datasets, for small values of $\Delta t$, the signals $\boldsymbol{z}^{(t)}$ and $\boldsymbol{z}^{(t+\Delta t)}$ tend to be very similar, which led to very similar covariance and cross-covariance matrices. Therefore, although the cross-covariance based models achieved better performance for all tested values of $\Delta t$, we showcase our results for a relatively large value of $\Delta t$ ($\Delta t = 7$ days for the weather dataset and $\Delta t = 20$ for the PEMS07 dataset) such that, the performance improvements are observable. As seen in Figure 7, for both datasets, the cross-covariance based models converge faster and to a smaller final test error, which is consistent with our observations on the HCP-YA dataset and has been predicted by our theoretical results.

### F.2. Convergence of Training Error.

We recall that there was a time series associated with each of the 100 features in the rfMRI time series data for an individual. For each individual, these 100 time series were utilized in the experiments. For a given individual, we denote the time series across 100 nodes at time step $t$ as the vector $\boldsymbol{z}^{(t)} \in \mathbb{R}^{100\times 1}$.

[11]The dataset can be found on https://www.kaggle.com/datasets/selfishgene/historical-hourly-weather-data

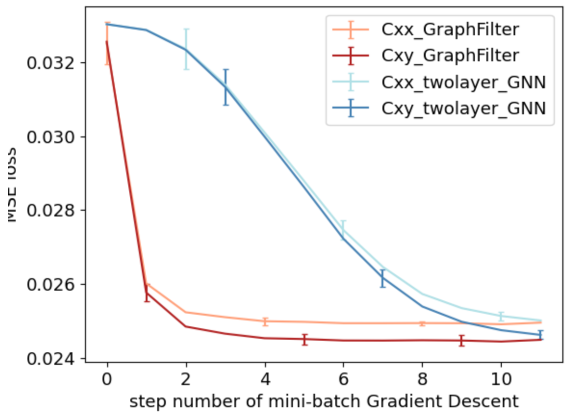

(a) Training loss for time series prediction task on PEMS07 dataset.

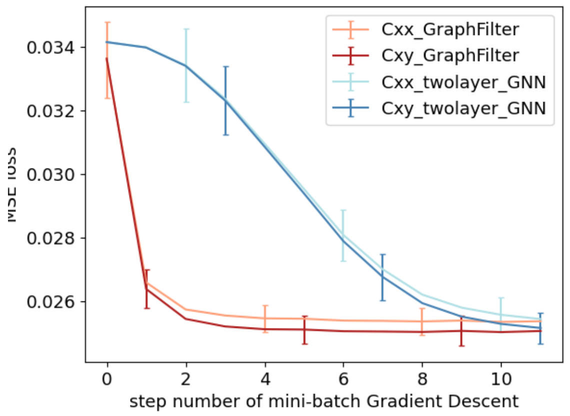

(b) Test loss for time series prediction task on the PEMS07 traffic dataset.

*Figure 6.* Experimental results for the PEMS07 dataset

For each individual, we created $N_{train} = 1000$ and $N_{test} = 100$ training and test samples respectively by randomly sampling (without replacement) pairs of vectors $\boldsymbol{z}^{(t)}, \boldsymbol{z}^{(t+1)}$ from the time series of length $N = 4500$. Next, the normalized sample covariance and sample cross covariance matrices were constructed using only the training data:

$$C_{XX}^{normalized} = \frac{X_{train}X_{train}^{\mathsf{T}}}{||X_{train}X_{train}^{\mathsf{T}}||}, \; C_{XY}^{normalized} = \frac{X_{train}Y_{train}^{\mathsf{T}}}{||X_{train}Y_{train}^{\mathsf{T}}||} \tag{263}$$

Afterwards, batch stochastic gradient descent with the Adam optimizer (Kingma & Ba, 2014) and the Pytorch library (Paszke et al., 2019) were used to train the following four models:

- Two-layer GNN with $K = 2$, $F = 50$ and GSO $S = C_{XY}^{normalized}$
- Two-layer GNN with $K = 2$, $F = 50$ and GSO $S = C_{XX}^{normalized}$
- Single graph filter with $K = 2$ and GSO $S = C_{XY}^{normalized}$
- Single graph filter with $K = 2$ and GSO $S = C_{XX}^{normalized}$

Regarding the choices of the parameters, $K = 2$ was chosen as (21) directly motivates using $C_{XY}$ as the GSO for the $K = 2$ case. Note that using $C_{XY} - I$ and $C_{XY}$ is essentially the same since in the graph filter polynomial $\sum_{k=0}^{K-1} h_k S^k \mathbf{x}$ we always have the term $h_0 I$ regardless of the choice of GSO. Furthermore, in Section F.4 and Fig. 10, we observed that changing $K$ does not have a noticeable impact on the model performance. Therefore, $K = 2$ is a reasonable choice for the experiments here. For choosing the number of features in the hidden layer, $F$, and the learning rate $\eta$ for training the GNN models, the Optuna hyperparameter optimization framework was leveraged (Akiba et al., 2019). The learning rate $\eta_1 = 0.0125$ was chosen for training the GNN models and $\eta_2 = 50 \cdot \eta_1$ for training the graph filters. For each individual, the training process was run 10 times with different permutations of the training and test sets, and the average over these was computed for all of the individual training and test error plots.

We also acknowledge that the GNN and Graph filter architectures were implemented using the Graph Neural Network library for Python based on the work of (Gama et al., 2019).

## F.3. Going Deeper Than Two Layers.

Here, we provide the experimental results for the setting when the GNNs may have more than two layers. Before that, we formalize a multi-layer GNN architecture with a graph filter as the building block and that has multiple-input-multiple-output (MIMO) information processing functionality.

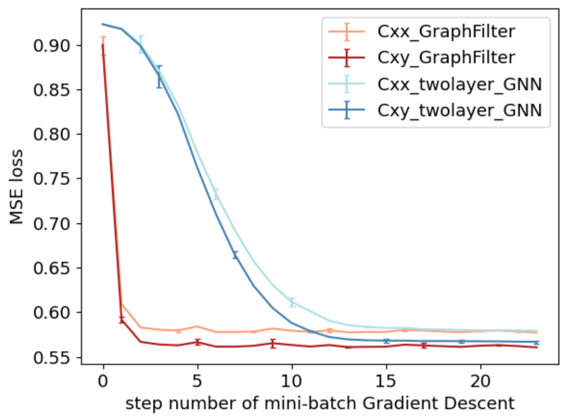

(a) Training loss for time series prediction task on the weather dataset.

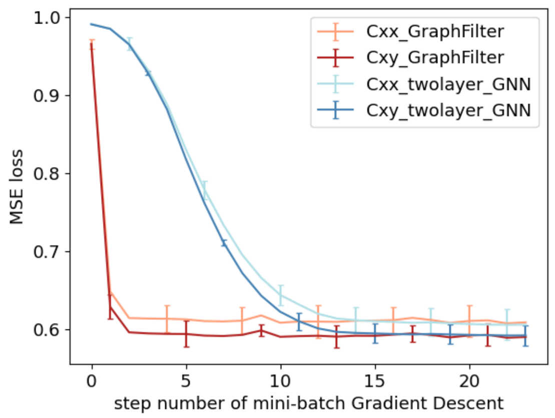

(b) Test loss for the time series prediction task on the weather dataset.

*Figure 7.* Experimental results for the weather dataset

**Multi-layer GNN.** We recall that the ability to learn non-linear mappings by GNNs are fundamentally based on addition of an element-wise non-linearity to a graph filter to form a graph perceptron, which is realized via a point-wise non-linearity $\sigma(\cdot)$ as $\sigma(H(S)\mathbf{x})$. We can further build upon the expressivity (and therefore, representational power) of a graph perceptron by concatenating multiple graph perceptrons to form a multi-layer GNN architecture. In this scenario, the relationship between the input $\mathbf{q}_{(l-1)}$ and the output $\mathbf{q}_{(\ell)}$ of the $\ell$-th layer of the GNN is given by $\mathbf{q}_{(\ell)} = \sigma(H_{(\ell)}(S)\mathbf{q}_{(\ell-1)})$. Based on the definitions of a graph perceptron and a multi-layer GNN, we next formalize the GNN architecture with MIMO functionality.

**Definition F.1** (Multiple-Input-Multiple-Output Graph Neural Network)**.** (Gama et al., 2020) We can substantially increase the representation power of GNNs by incorporating multiple parallel features per layer. These features are the result of processing multiple input features with a parallel bank of graph filters. Let us consider $F_{\ell-1}$ $n$-dimensional inputs $\mathbf{q}^1_{(\ell-1)}, \dots, \mathbf{q}^{F_{l-1}}_{(\ell-1)}$ at layer $\ell$. Each input, $\mathbf{q}^g_{(\ell-1)}$ for $g \in \{1, \dots, F_{\ell-1}\}$ is processed in parallel by $F_\ell$ different graph filters to output the $F_\ell$ $n$-dimensional outputs denoted by $\mathbf{u}^{fg}_{(\ell)}$ with the following relationships

$$\mathbf{u}^{fg}_{(\ell)} = H^{fg}_{(\ell)}(S)\mathbf{q}^g_{(\ell-1)} = \sum_{k=0}^{K} h^{fg}_{(\ell),k} S^k \mathbf{q}^g_{(\ell-1)}, \quad f \in \{1, \dots, F_\ell\}.$$

The outputs $\mathbf{u}^{fg}_{(\ell)}$ are subsequently summarized along the input index $g$ to yield the aggregated outputs

$$\mathbf{u}^{f}_{(\ell)} = \sum_{g=1}^{F_{l-1}} H^{fg}_{(\ell)}(S)\mathbf{q}^g_{(\ell-1)}, \quad f \in \{1, \dots, F_\ell\}.$$

The aggregated outputs $\mathbf{u}^f_{(\ell)}$ are finally passed through a non-linearity $\sigma(\cdot)$ to compute the $\ell$-th layer output as follows

$$\mathbf{q}^f_{(\ell)} = \sigma\left(\mathbf{u}^f_{(\ell)}\right), \quad f \in \{1, \dots, F_\ell\}.$$

A GNN in its complete form is a concatenation of $L$ such layers, in which each layer computes the above operations.

In the main paper, we theoretically analyzed a two-layer GNN without non-linearity in the final layer, with $F_0 = F_2 = 1$ (since we only have one input and one output feature vector in each sample), and $F$ number of features in the hidden layer i.e., $F_1 = F$ (see Fig. 8).

**Experiment results.** To assess the effect of increasing the depth of the GNN in the experiments, we present results for two-layer, three-layer and four-layer GNNs that had been trained for one individual in the HCP-YA dataset. The training

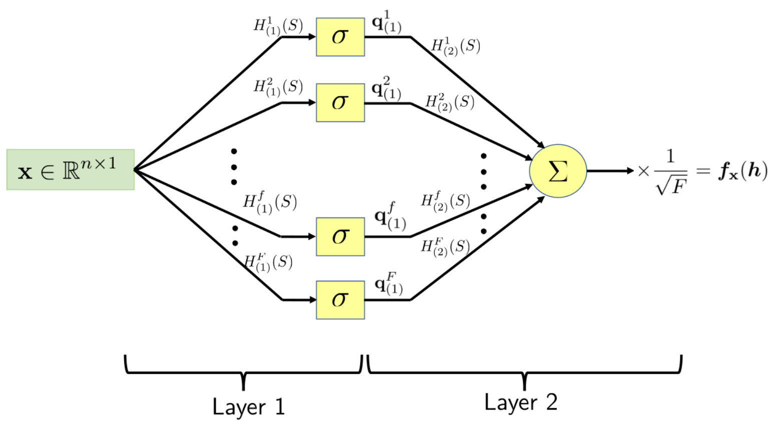

*Figure 8.* The two layer GNN architecture defined in Section 3.2

and test loss for the gradient descent for these models is illustrated in Fig. 9. It can be seen that regardless of the depth of the GNNs, the training loss and test loss for the GNN with $S = C_{XY}$ converged faster as compared to those with $S = C_{XX}$ and to a smaller final value.

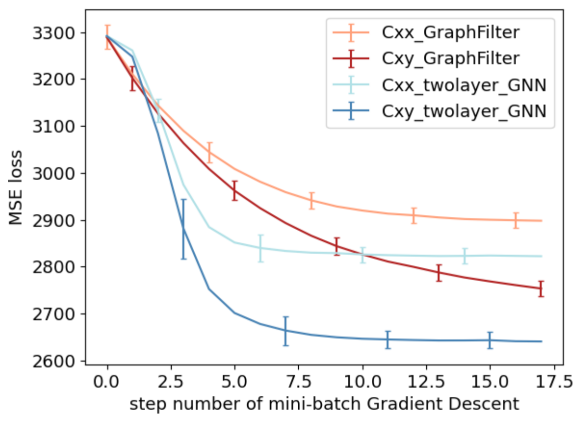

(a) Training loss during GD for two layer GNN;
$F_0 = 1, F_1 = 50, F_2 = 1$

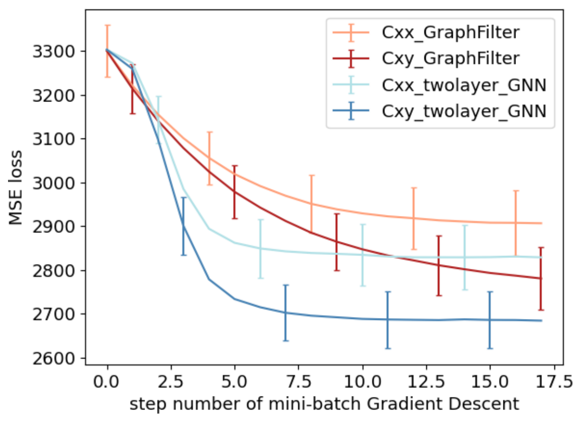

(b) Test loss during GD for two layer GNN;
$F_0 = 1, F_1 = 50, F_2 = 1$

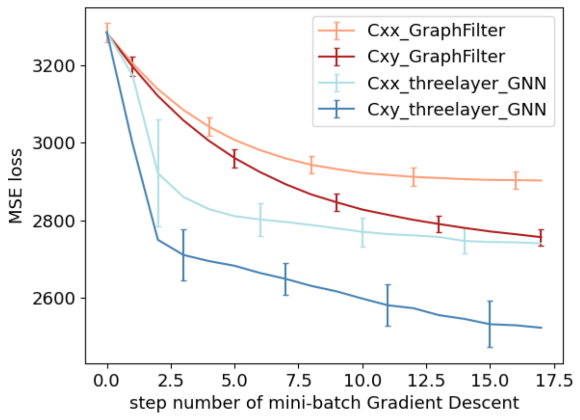

(c) Training loss during GD for three layer GNN;
$F_0 = 1, F_1 = 50, F_2 = 50, F_3 = 1$

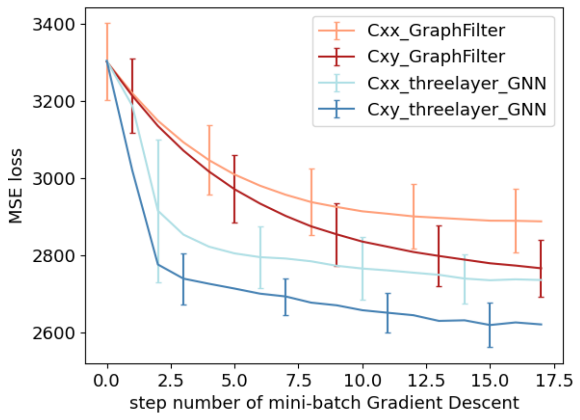

(d) Test loss during GD for three layer GNN;
$F_0 = 1, F_1 = 50, F_2 = 50, F_3 = 1$

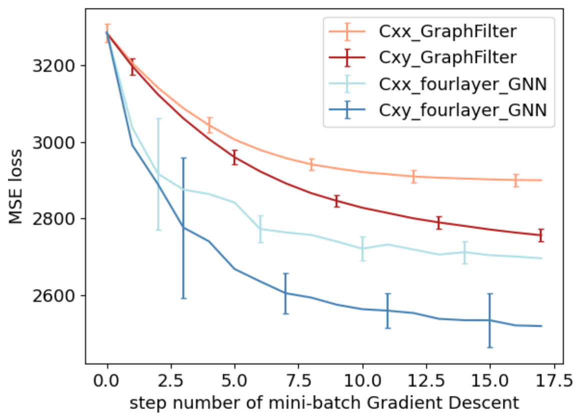

(e) Training loss during GD for four layer GNN;
$F_0 = 1, F_1 = 50, F_2 = 50, F_3 = 50, F_4 = 1$

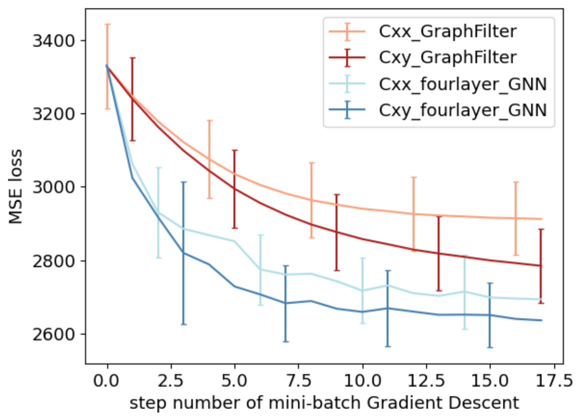

(f) Test loss during GD for four layer GNN;
$F_0 = 1, F_1 = 50, F_2 = 50, F_3 = 50, F_4 = 1$

*Figure 9.* The effect of increasing depth of the GNN

### F.4. The effect of changing the number of graph filter taps $K$

We recall our motivation for using the cross-covariance graph as the GSO from Theorem 3.5 where we concluded that the optimal GSO $S^*$ should satisfy $\sum_{k=0}^{K-1}(S^*)^k = \mu \cdot C_{XY}$. For the case $K = 2$, this leads to $S^*$ being proportional to $C_{XY}$ (see (21)). However, for $K > 2$, while the optimal GSO is still clearly a function of the cross-covariance $C_{XY}$, solving (20) to find a closed form expression for $S^*$ is not trivial. In this context, we investigated empirically whether $S = C_{XY}$ was a better choice than $S = C_{XX}$ when $K > 2$. The plots in Fig. 10 illustrate the training error for GNN and graph filter models with different values of $K$ for one individual in the HCP-YA dataset. Clearly, GNNs with $S = C_{XY}$ outperformed those with $S = C_{XX}$ as GSO. These experiments indicate that the cross-covariance matrix is still a better choice as a GSO for GNNs when $K > 2$.

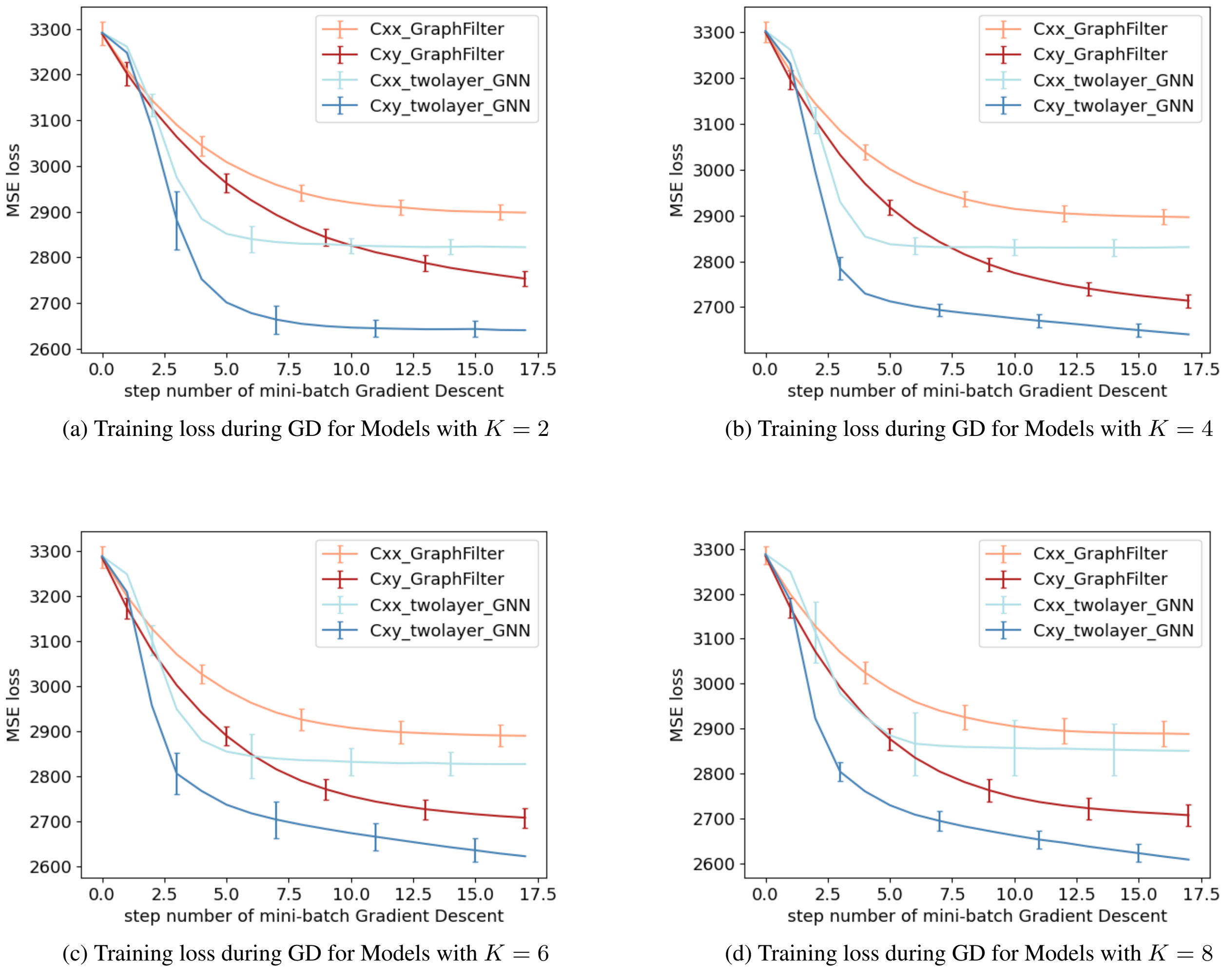

(a) Training loss during GD for Models with $K = 2$

(b) Training loss during GD for Models with $K = 4$

(c) Training loss during GD for Models with $K = 6$

(d) Training loss during GD for Models with $K = 8$

*Figure 10.* The effect of changing the number of filter taps $K$

## F.5. The effect of changing the non-linear activation function $\sigma(\cdot)$.

Our theoretical results hold for $\tanh$ function as the non-linearity $\sigma(\cdot)$. In this section, we investigated empirically whether the cross-covariance matrix was a better choice as a GSO than the covariance matrix for different choices of $\sigma(\cdot)$. The plots in Fig. 11 demonstrate the results from training for GNN and graph filter models with different activation functions, for a single individual. Aside from the setting where the activation function was the ReLU function (for which the convergence depends highly on the initialization thus the variance in the training process between different runs is too high to conclude anything meaningful), the experiments for other activation functions showed that the GNNs with $S = C_{XY}$ converged faster and to a smaller final value as compared to GNNs with $S = C_{XX}$. This observation suggests that the theoretical insights drawn from the scenario of $\sigma = \tanh$ extends empirically to settings with the choice of other activation functions.

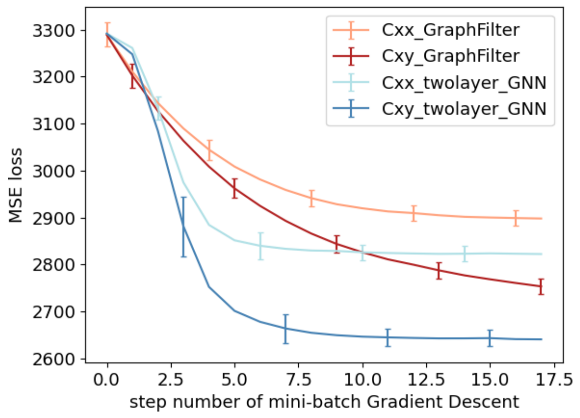

(a) Training loss during GD for Models with the Leaky ReLU activation function

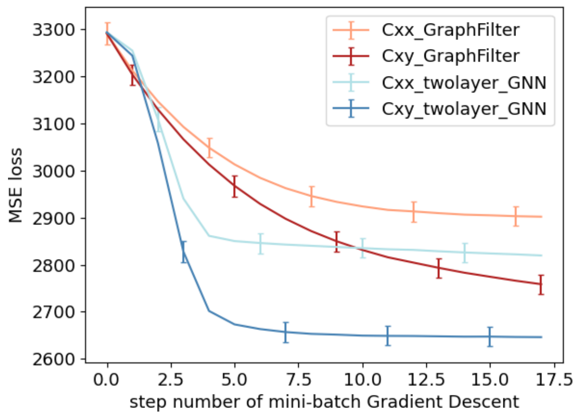

(b) Training loss during GD for Models with the $\tanh$ activation function

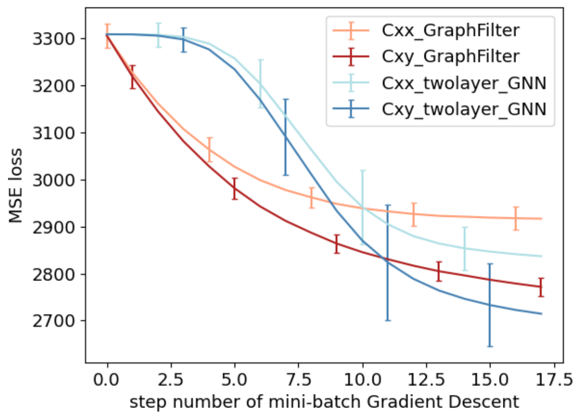

(c) Training loss during GD for Models with the Sigmoid activation function

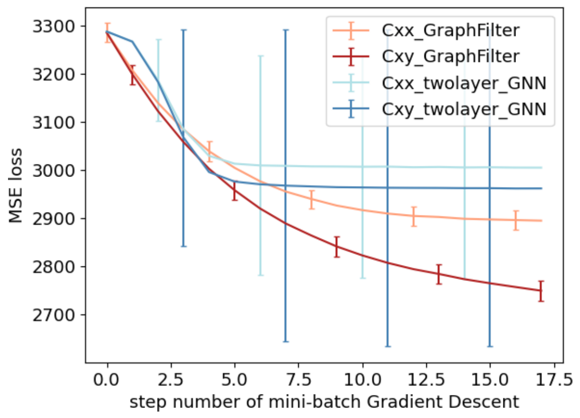

(d) Training loss during GD for Models with the ReLU activation function

*Figure 11.* The effect of changing the non-linear activation function $\sigma(\cdot)$ on GNN performance. (Graph filter curves are only plotted for comparison)

## F.6. Time-series prediction using more than just the previous time step

In the experiments in the main paper, we considered a prediction task where we use the value of the signal at just the previous time step to predict the current signal. However, in practice, the time series forecasting algorithms typically use information from a longer history, i.e., more than just the previous time step. Here, we investigate a time-series prediction model that uses the model in Section 4 as the building block to form predictions from an arbitrary set of time steps in the past.

In this design, we used $D$ separate graph filters to process the signal values at the previous $D$ time steps and aggregated the outputs of the filters to form the final prediction:

$$\boldsymbol{f}(\boldsymbol{z}^{(t-1)}, \boldsymbol{z}^{(t-2)}, \cdots, \boldsymbol{z}^{(t-D)}) = \sum_{k=0}^{K-1} h_{k,1} S_1^k \boldsymbol{z}^{(t-1)} + \cdots + \sum_{k=0}^{K-1} h_{k,D} S_D^k \boldsymbol{z}^{(t-D)} \tag{264}$$

This methodology can be extended to the two-layer GNN architecture by replacing each graph filter in the GNN with multiple graph filters as per (264). Note that we are not restricted to use the same graph shift operator in these filters. For example, for processing the signal value from $d$ time steps ago, we could utilize the cross-covariance between signal values with a distance of $d$ time steps i.e.

$$S_d = \mathbb{E}\left[\boldsymbol{z}^{(t)}(\boldsymbol{z}^{(t-d)})^T\right] \tag{265}$$

To gauge the usefulness of this setting, we consider the multiple filter model in (264) for $D = 1, 2, 3, 4, 5$. The result can be seen in Figures 12a, 12b. It can be observed that there is a significant gain in increasing from $D = 1$ to $D = 2$. However increasing $D$ further does not seem to yield better test performance, at least for this dataset. Note that the cross-covariance graph shift operator was used for all the models in Figure 12.

Next we set $D = 2$ to compare the cross-covariance and covariance graph constructions in this setting. The results can be seen in Figures 12c, 12d. It can be observed that in this setting as well, models with cross-covariance graph shift operator outperform those with covariance graphs. This holds for both the graph filter models and the two-layer GNNs. Also note that increasing $D$ to 2, results in better performance for the two-layer GNN in addition to the Graph filter models However similar to the results observed for the graph filter, increasing $D$ further for the GNNs did not result in any observable gains.

## F.7. Other Graphs constructed based on the input data

In our experiments in the main paper, we have considered the cross-covariance matrix as the graph shift operator to be representative of the class of graphs constructed from only the input data. In order to further emphasize on the advantages offered by cross-covariance graphs, we also consider the two following additional methods of constructing a graph from the input data (See (Qiao et al., 2018) for a detailed review of different methods of graph construction used in the literature). The first method is based on Euclidean distance between values of the signals on each node of the graph and using the nonlinear Gaussian kernel, the weight between node $i$ and $j$ of the graph is quantified as follows:

$$S_{ij} = e^{-\frac{||x_i - x_j||_2^2}{2\varrho^2}}, \tag{266}$$

where $\varrho = 1$ in our experiments.

The second method for graph construction set the weights of the adjacency matrix proportional to the Pearson's correlation coefficient between two nodes. In this case, the weight between node $i$ and $j$ of the graph is

$$S_{ij} = \frac{(x_i - \bar{x}_i)^T(x_j - \bar{x}_j)}{||x_i - \bar{x}_i||_2 ||x_j - \bar{x}_j||_2} \tag{267}$$

where in both (266) and (267), $x_i, x_j \in \mathbb{R}^{N_{\textsf{train}} \times 1}$ are the $i$-th and $j$-th columns of the input data matrix $X_{\textsf{train}} \in \mathbb{R}^{n \times N_{\textsf{train}}}$ respectively.

The results corresponding to these two choices of graph construction for one individual have been illustrated in Fig. 13. It is observed that while the performance of the models with different input-based graph constructions vary, they are all consistently outperformed by the models with the cross-covariance based graph. This trend is consistent across different individuals in the dataset.

As an additional baseline, we have also included the result for a Fully connected two layer neural network (FCNN) for comparison. The FCNN and the two layer GNN with cross-covariance graph exhibit comparable performance in terms of

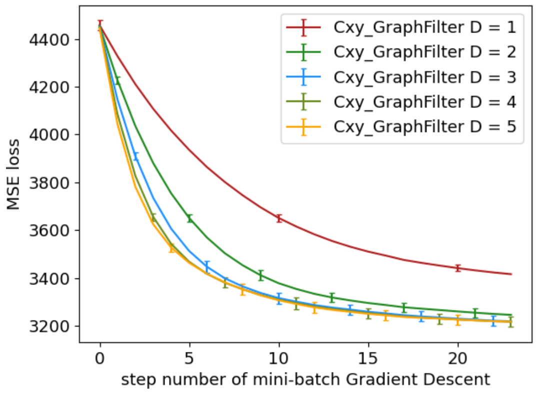

(a) Training loss during GD for Time-series prediction using $D$ previous time steps.

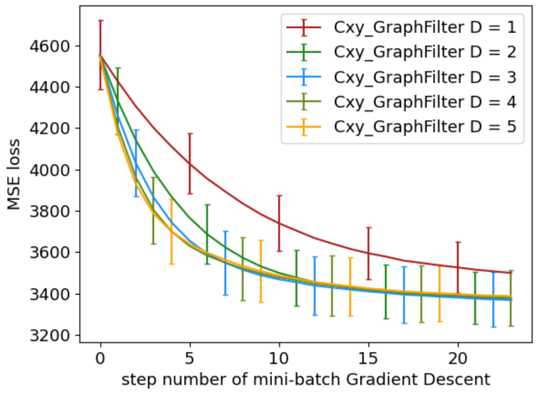

(b) Test loss during GD for Time-series prediction using $D$ previous time steps.

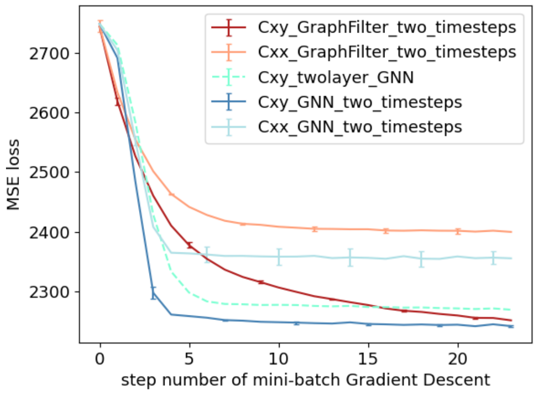

(c) Training loss during GD for Time-series prediction using $D = 2$ previous time steps.

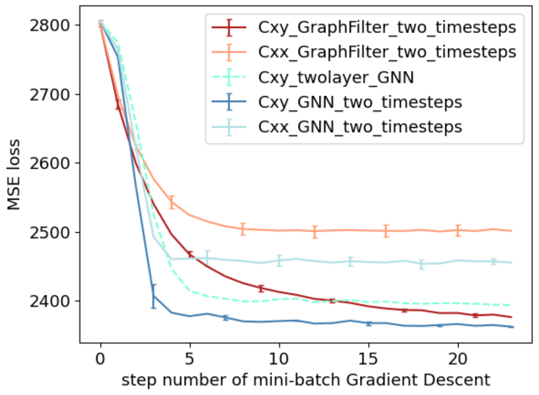

(d) Test loss during GD for Time-series prediction using $D = 2$ previous time steps.

*Figure 12.* Time-series prediction using $D$ previous time steps

final test error, while the GNN converges faster than FCNN. In general, for the complete HCP-YA dataset, the FCNN often has slightly smaller final test error, which is achieved at the expense of complexity as it has almost 100 times the number of trainable parameters than the GNN models.

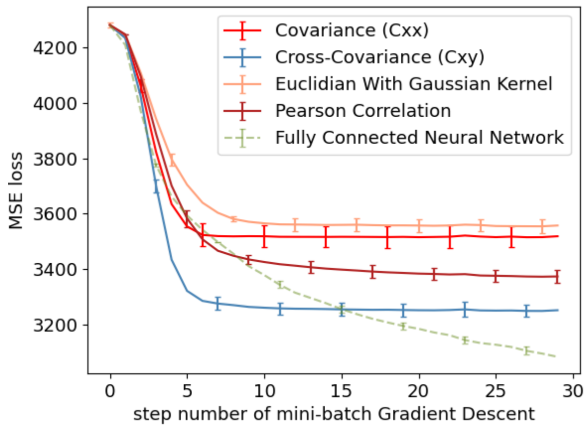

(a) Training loss during GD when using different constructions for the graph shift operator

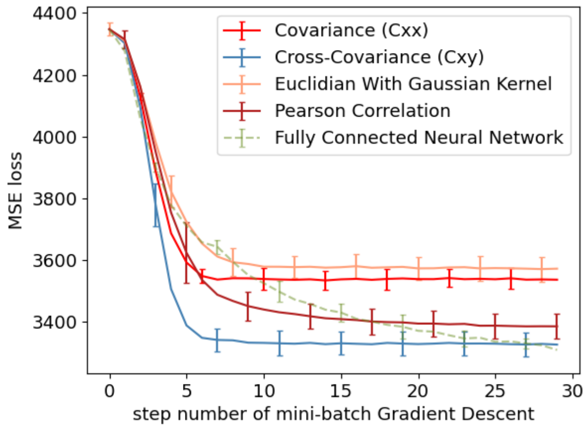

(b) Test loss during GD when using different constructions for the graph shift operator

*Figure 13.* Comparison between GNN models with cross-covariance graphs and GNN models with graphs constructed according to different construction methods. The models compared here are two-layer GNNs.

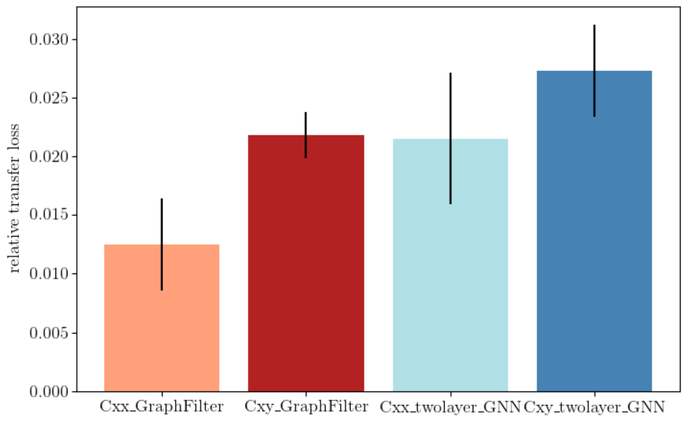

*Figure 14.* The relative transfer loss from N = 50 to N = 100 for different models. The transfer loss is defined as the difference between the test loss in the following two scenarios: (i) Model trained and tested on dataset with $n = 100$ features; (ii) Model trained on dataset with $n = 50$ and tested on dataset with $n = 100$.